UNIVERSITÉ DU LUXEMBOURG

PhD-FSTM-2024-055
Faculty of Science, Technology and Medicine

DISSERTATION

Presented on the 12/07/2024 in Luxembourg

to obtain the degree of

DOCTEUR DE L'UNIVERSITÉ DU LUXEMBOURG EN SCIENCES DE L'INGÉNIEUR

by

Johannes Sebastian Laur
Born on 26th July 1989 in Laupheim, Germany

Mitigating Radio Blackout in Hypersonic Flights and Atmospheric Entries – Computational Electromagnetics and Experimental Validation

Dissertation Defense Committee

Dr. Symeon CHATZINOTAS, Chair
Professor, University of Luxembourg, Luxembourg
Dr. Juan Carlos MERLANO DUNCAN, Vice-chair
Research Scientist, University of Luxembourg, Luxembourg
Dr. Jan THOEMEL, Member (Supervisor)
Research Scientist, University of Luxembourg, Luxembourg
Dr. Francesco PANERAI, Member
Professor, University of Illinois Urbana-Champaign, USA

Abstract

The radio blackout phenomenon disrupts essential communication, and navigation during hypersonic flights posing significant challenges especially for atmospheric entry missions because effective data collection is vital for emergency preparation and response. Modeling electromagnetic (EM) wave propagation is complex and costly. Ray-tracing algorithms offer cost-effective tools for optimizing radio communication in complex scenarios and thus for blackout modeling. During atmospheric entry, vehicles experience high velocities and significant interactions with the atmosphere causing plasma formation and radio blackout. Radio blackout mitigation techniques such as aerodynamic shaping, quenchant injection, and magnetic windows have been proposed. The magnetic windowing method is analyzed in this work as part of the Magnetohydrodynamic Enhanced Entry Systems for Space Transportation (MEESST) project.

This thesis researches and applies an advanced Magnetohydrodynamics (MHD) ray-tracer to analyze the effects of magnetized plasma on signal propagation during hypersonic flight and atmospheric re-entry, focusing on addressing the radio communication blackout caused by the ionized gas surrounding a spacecraft. The MHD ray-tracer integrates electromagnetic wave theory with high-speed fluid dynamics, offering detailed analysis of signal properties under various inhomogeneous plasma conditions.

In a first step, the analysis of electron number densities and ray trajectories in magnetized plasma indicated that sufficiently strong magnetic fields alter the flow field, consistent with existing literature. Cases with applied magnetic fields show an increased radiation aperture angle, suggesting a potential to mitigate or eliminate radio blackout.

In a second step, a new signal characterization method analyzing the electric field along the ray path provides a deeper understanding of the physical mechanisms behind radio blackout phenomena. Analysis of a non-magnetized plasma case reveals that plasma increases signal intensity by bending rays towards each other, more influential than refraction losses. Free space loss, which rises with higher frequencies, counteracts the effect of plasma on the spread factor. Validation against VKI ground experiments confirms the method's effectiveness in explaining radio blackout physics.

In a third step, the behavior of various angles between the wave vector and the magnetic field vector for ordinary and extraordinary waves aligned with literature and provided important insight. An applied magnetic field can reduce electron number density and alter the refractive index along the ray trajectory, increasing the radiation aperture angle and reducing signal attenuation, thereby improving communication. Magnetized plasmas introduce complexities like Faraday rotation and increased signal absorption but offer the potential for mitigating blackouts by widening communication angles through controlled magnetic fields. The study demonstrates the functionality

of the magnetic windowing method to create communication corridors for re-entry vehicles. BORAT matches very well with experimental results for non-plasma cases. For plasma cases, computed attenuations are above those measured.

The developed signal characterization method provides deeper insights into the physical phenomena causing radio blackout. This research advances the understanding of plasma effects on signal propagation and explores mitigation techniques, contributing to safer and more successful space missions. Further insight can be gained when additional and more accurate measurements are available.

Sometimes it pays to stay in bed on Monday, rather than spending the rest of the week debugging Monday's code.

Dan Salomon

Acknowledgements

I am not one for many words (which might explain why my thesis is not particularly long). Recently, I came across Zara Larsson's song Memory Lanes, and its lyrics resonated with what I want to express here. The chorus goes: "So I walk myself down memory lane, I still hold on to all the joy and the pain, So I sing a little louder, get carried away, And I thank myself for who I became." Reflecting on my journey to this point, I realize it is not just about thanking myself for who I have become. That would be both selfish and untrue.

First and foremost, I owe my deepest gratitude to my parents, my four brothers, and my entire family for their unwavering support and encouragement in pursuing my dreams. The path I chose was not easy, but it was worth it, and knowing I have a place to return to, no matter where my plans take me, brings me great comfort.

I also want to extend my heartfelt thanks to my fiancé, Nick, who has stood by me for the last three and a half years. You have shared in my successes and helped me through the tough times, especially during those stressful moments when I was not at my best. Thank you, Nick, for always making me feel at home, for your love, and for reminding me of my worth. You have been my rock throughout this PhD journey, and I cannot wait to start the next chapter of our lives together—both professionally and personally, as we plan our wedding and look forward to our future.

I am grateful to my colleagues at the University of Luxembourg, particularly those from the MEESST project, for their support and fresh perspectives that made my work more rewarding. I also appreciate the guidance and supervision of my CET committee members and advisory board. A special thanks to my PhD supervisor, Jan Thoemel, for your exceptional mentorship and patience. This journey would not have been as successful or fulfilling without your guidance.

Now, for the more formal acknowledgments. My research, as part of the MEESST project, was funded by the European Union's Horizon 2020 Research and Innovation Program under grant agreement 899298. I would also like to thank the HPC facilities and the team at the University of Luxembourg for their invaluable computational support [1] – see hpc.uni.lu.

Lastly, a special thanks to Jens Warkall from Genias Graphics GmbH & Co. KG for occasionally providing free Tecplot licenses.

Johannes Sebastian Laur
Luxembourg, July 2024

Contents

List of Figures

List of Tables

1 Introduction

In the following chapter, the challenges of atmospheric entry, and hypersonic flight in general are described including the process and important parameters leading to the cut-off of communication, the radio blackout. An overview of missions facing radio blackout is followed afterward. Then, possible radio blackout mitigation methods are described and the Magnetohydrodynamic Entry Systems for Space Transportation (MEESST) project is introduced using a novel high-temperature superconducting magnet to mitigate radio blackout. The chapter closes by the motivation and the importance for society of this work, and completed with the scope and the outline of this thesis are presented.

Contents

1.1 Atmospheric entries and hypersonic flights

A crucial phase of a space mission is the atmospheric entry phase, characterized by exceptionally high velocities and extensive interaction with the planet's gaseous atmosphere. During this stage, the flow conditions around the entry vehicle undergo significant alterations [5].

The categorization of hypersonic flow pertains to velocities significantly surpassing the speed of sound. The distinctive attributes of hypersonic flow can be broadly categorized into hydrodynamic features, arising from the high flight Mach number and physical or chemical aspects, given the substantial kinetic energy of the flow [6]. The Mach number M is defined as the ratio of the velocity v to the speed of sound a in the gas, i.e,

$$M = \frac{velocity}{speed\,of\,sound} = \frac{v}{a}. \tag{1.1}$$

The speed of sound a is defined for an ideal gas as follows:

$$a = \sqrt{\frac{\gamma p}{\rho}} = \sqrt{\gamma R T}, \tag{1.2}$$

with γ as the specific heat ratio, ρ as the density, p as the pressure, R as the gas constant, and T as the temperature of the gas being considered. If M is less than 1, the flow is termed as subsonic, and when M exceeds 1, it is termed as supersonic. In cases where the Mach number is around 1 and involves areas with both subsonic and supersonic flow, it's classified as transonic. For Mach numbers significantly higher than 1, the flow is designated as hypersonic [7].

The hypersonic flow regime itself can be divided into two subsections [8] (chemistry is considered for air):

1. The first section pertains to the broad objective of prolonged hypersonic cruising within the atmosphere. This objective typically involves a duration lasting from 10 to 100 minutes, Mach numbers ranging between 4 and 12, stagnation temperatures ranging from 500 K to 4000 K, and a relatively low to moderate concentration of oxygen atoms. This zone was anticipated to be where hypersonic transportation would operate.

2. The second segment details the general-purpose mission involving ascent into or descent from orbit. The mission for returning from Low Earth Orbit (LEO) typically lasts around 10 minutes, with Mach numbers ranging between 10 and 25, stagnation temperatures between 1500 K and 5500 K, and notable oxygen dissociation alongside moderate nitrogen dissociation. Conversely, the mission for returning from lunar orbit typically spans about 15 minutes, featuring Mach numbers between 10 and 36, stagnation temperatures ranging from 1500 K to 9500 K, substantial dissociation of oxygen and nitrogen, and moderate levels of ionization.

In hypersonic speeds, shock waves primarily dictate the force field through adiabatic compression, unlike subsonic speeds where isentropic expansions are responsible for these forces. Despite temperature extremes impacting gas density and composition, they have minimal influence on pressure levels, hence exerting limited effect on force structure. Consequently, the windward side shape significantly impacts the

overall force structure of a spacecraft, whereas the influence of the leeward side shape is relatively minor, although it can impact vehicle stability by creating necessary stabilizing moments [8].

A notable feature of hypersonic flow involves the interaction between the oblique shock wave originating at the body's front edge and the boundary layer on its surface. Take, for instance, the oblique shock wave created at the leading edge of a wedge within a supersonic flow, depicted on the left in Figure 1.1. With increasing Mach numbers, the shock angle decreases, causing the shock to approach very near to the surface at elevated Mach numbers. This phenomenon is shown on the right in Figure 1.1 [7].

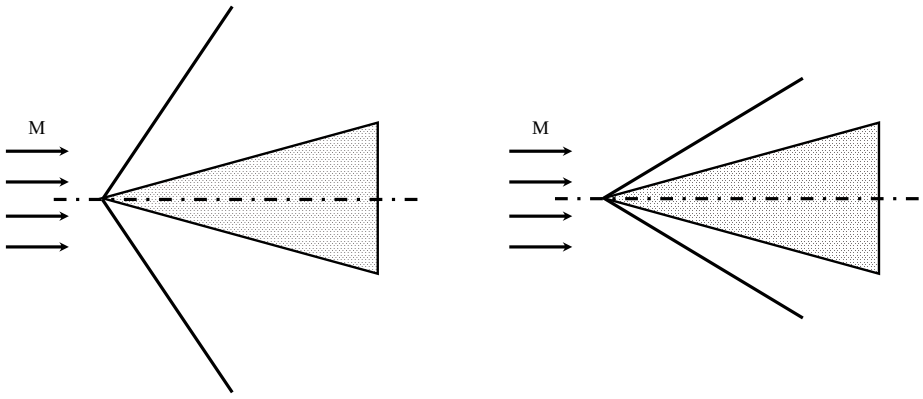

Figure 1.1: The angle of shock in both low and high supersonic Mach number flows over a wedge [7].

Within hypersonic flow, the shock wave typically is close to the surface, while the boundary layer tends to be substantial in thickness. Consequently, this often leads to interaction between the shock wave and the boundary layer flow, resulting in a curved shock and a flow pattern resembling the depiction on the left in Figure 1.2. This curved shock is typical in hypersonic flows for all body shapes (illustrated in Figure 1.2, right).

The high temperatures that are generated behind the shock waves in hypersonic flows are another characteristic of such flows. At high temperatures, a notable effect arises due to the constitution of air, predominantly composed of nitrogen and oxygen in its diatomic state under standard conditions. As temperatures rise, these diatomic gases tend to dissociate into their monoatomic states, while at even higher temperatures, the monoatomic atoms undergo ionization. This dissociation occurs within specific temperature intervals:

- For temperatures between 2000 K and 4000 K: $O_2 \rightarrow 2O$, indicating the breakdown of oxygen molecules into O atoms.
- For temperatures between 4000 K and 9000 K: $N_2 \rightarrow 2N$, signifying the breakdown of nitrogen molecules into N atoms.

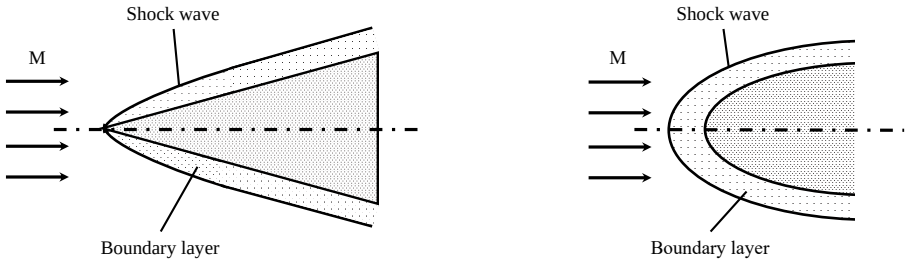

Figure 1.2: Interaction between shock wave and boundary layer in hypersonic flow over a wedge and a curved body [7].

Importantly, this dissociation does not instantaneously affect the entire air composition upon reaching a certain temperature threshold. Throughout these temperature ranges, the air consists of a mix of diatomic and monoatomic molecules, with the proportion of monoatomic molecules increasing as temperatures increases.

Likewise, ionization occurs at temperatures exceeding 9000 K:

- $O \rightarrow O^+ + e^-$
- $N \rightarrow N^+ + e^-$

Again, the air is only partially ionized depending on the temperature. The hypersonic flow and the thermochemical processes around solid objects within the Martian atmosphere, where approximately 97 % of the atmosphere is composed of CO_w, are not described here. Further information can be found here [9].

For blunt bodies, a significant nose radius forms the basis of the spacecraft's passive thermal shield, as convective heating decreases with the local curvature radius. Simultaneously, the large frontal area results in substantial drag primarily caused by the high-pressure shock layer formed due to adiabatic compression. In contrast, skin friction plays a minor role in drag compared to slender bodies. Certain reentry vehicles, especially ballistic missile warheads, adopt a design resembling spherical blunted cones. It is evident that smaller nose radii can be incorporated without significant increases in drag. The blunt nose design helps alleviate reentry heating by reducing the heat flux at the stagnation point. Consequently, thermal protection can be improved with minimal impact on drag [8].

1.2 Reasons for radio blackout

The cut-off of communication is a persistent challenge in the realm of hypersonic flight and atmospheric entries. Atmospheric entries, or hypersonic flights in general, cause the formation of shock waves at the vehicle's front, where a significant portion of the vehicle's kinetic energy is transformed into heat, elevating the temperature of the surrounding gas. This process causes the dissociation and the consequent ionization of gas molecules. This ionized gas, called plasma, forms around the

vehicle's leading edge. This plasma leads to a disruption in radio communication, called "radio blackout". The radio blackout issue impacts the ability of ground stations to detect and track the vehicle, as well as the efficiency of transmitting real-time telemetry data and navigation information. This can result in unforeseeable consequences and even disasters during aerospace missions [10, 11, 12, 13, 14].

The physicist Frank-Kamenetski labeled plasma the fourth state of matter. In outer space, matter is primarily ionized, enabling free movement of electrons and ions, often influenced more by electromagnetic forces than gravity, observed in stars and interstellar space. Notably, plasma constitutes the universe's predominant state of matter, contrasting with the neutral matter found in our living environment. Over 95 % of the universe consists of plasma. Formed by heating gas to high temperatures, plasma is self-luminous and electrically conductive, with interactions between its components releasing radiant energy. This complex behavior necessitates a deep understanding of atomic physics and gas technology due to the intricate collision processes occurring within the plasma.

As an example, consider the entry, descent, and landing (EDL) process for Mars missions, which begins as the vehicle reaches the boundary of the Martian atmosphere with a velocity of approximately Mach 25. The EDL phases are of paramount importance in Mars exploration missions, as they directly dictate the mission's overall success. Throughout the Mars atmospheric entry phase, the velocity of the entry vehicle undergoes a substantial reduction, dropping from 4–7 km/s to approximately 400 m/s. Notably, nearly 99% of the initial kinetic energy is dissipated during this atmospheric entry phase [15].

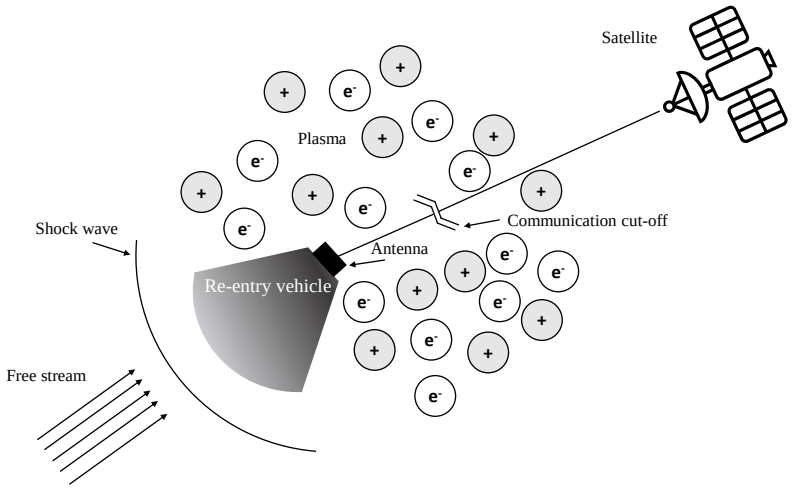

Figure 1.3: Schematic of the reason for cut-off of communication [16].

Figure 1.3, illustrates how plasma-induced communication disruption occurs during atmospheric entries. This communication interruption primarily arises from the presence of free electrons within the plasma. These electrons have the effect of altering the path of the radio signal by refracting, reflecting, or completely diminishing the electromagnetic waves being transmitted to or received from an onboard antenna.

The blackout phenomenon in case of a non-magnetized plasma with negligible collisions occurs when the plasma frequency surpasses the radio frequency, as given

in Eq. 1.3:

$$f_{radio} \leq f_{plasma} = \frac{1}{2\pi}\sqrt{\frac{e^2 N_{e_{crit}}}{\epsilon_0 m_e}}. \tag{1.3}$$

In this equation, f_{radio} signifies the radio frequency measured in Hertz, f_{plasma} represents the plasma frequency measured in Hertz, e corresponds to the electric charge of an electron in Coulombs, m_e stands for the mass of an electron in kilograms, and $N_{e_{crit}}$ denotes the critical electron number density per cubic meter.

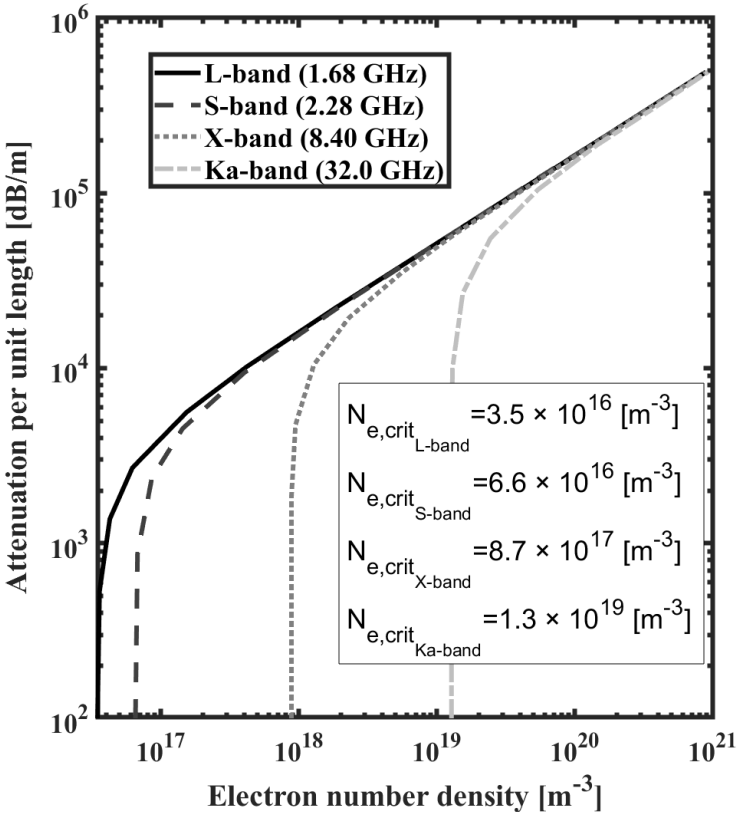

Figure 1.4: Attenuation per unit length over electron number density for various frequencies with their critical electron number densities for non-magnetic, collisionless plasma [17, 18].

Figure 1.4 illustrates the signal attenuation per unit length as a function of electron number density for different frequencies, and it also includes the associated critical electron number densities for the L-, S-, X-, and Ka-bands [17, 18]. It is important to note that blackout conditions occur when the plasma frequency equals or surpasses the radio frequency. As an example, the critical electron number density for the L-band is $3.5 \times 10^{18}\mathrm{m}^{-3}$, and for the Ka-band, it is $1.3 \times 10^{19}\mathrm{m}^{-3}$. The electron number densities are also influenced by the vehicle's trajectory and design. Typically, electron number densities encountered during atmospheric entries fall within the range of $10^{15}\mathrm{m}^{-3}$ and $10^{19}\mathrm{m}^{-3}$ [19].

1.3 History of missions facing radio blackout

During the early days of human space exploration in the 1960s, a prominent and quickly identified issue was the significant reduction in radio communication signals due to the plasma enveloping the reentry vehicle [20]. The issue of radio blackout has garnered significant interest from both the academic community and space agencies, especially during the era of the Apollo missions. During the 1960s and 1970s, extensive research on the ground and in-flight experiments were undertaken by NASA and the U.S. Air Force. These experiments aimed to measure the characteristics of the plasma sheath and explore potential approaches for mitigating the problem [11]. Spacecraft involved in Project Mercury, Gemini, and Apollo encountered substantial communication blackouts lasting several minutes during their atmospheric re-entry phase. During the atmospheric re-entry phase, Project Mercury, in particular, endured a challenging blackout period lasting approximately 4 minutes. In the case of Apollo, the high-speed interaction of the blunt capsule with Earth's atmosphere led to communication blackouts ranging from 4 to 10 minutes in duration at the S-band frequency [21].

To date, the occurrence of this radio frequency blackout has been documented in numerous reentry flight trials, encompassing missions such as RAM-C II (Reentry Attenuation Measurement), the Apollo command module (conducted by NASA), and OREX (Orbital Re-entry Experiments; formerly NASDA/NAL, currently managed by JAXA) [22]. A critical element in forecasting the initiation and cessation of radio blackout during entry into a planetary atmosphere is the precise determination of electron concentration (Ne) within the plasma layer surrounding the entry vehicle. Significant advancements had been achieved in comprehending and projecting ionized flow dynamics back then. A pivotal factor for this progress had been the availability of flight-measured data collected across various entry scenarios and correlated with analyzable flow patterns. The RAM project conducted by the Langley Research Center played a substantial role in enhancing both theoretical insights and experimental outcomes. A re-entry trajectory of the NASA RAM C-II test and the phases of radio blackout during re-entry for different frequency bands is given in Fig. 1.5. The plasma frequency changes with altitude and velocity. This leads to different blackout phases for VHF, S-, C-, and X-band. During this blackout phase, no communication is possible and no telemetry data can be received. This should be prevented for the safety of vehicles and their passengers or cargo [23].

From equation 1.3 it is obvious that the plasma frequency depends on the electron density. In-flight test data from NASA RAM C tests are shown in Fig. 1.6. Obviously, the electron density distribution is normal to the vehicle surface, and the peak electron density is largely varied at different altitudes. This agrees with the observed onset of radio blackout for different frequency bands in Fig. 1.5. Plasma occurs at an altitude of 250 kft with a maximum electron density of $10^{16}\mathrm{m}^{-3}$. A peak electron density of $10^{19}\mathrm{m}^{-3}$ is reached at an altitude of 100 kft [24].

In February 1994, the OREX space probe was launched into space using an H-II rocket that departed from the Tanegashima Space Center in Japan. Subsequently, during the re-entry phase, all communication between the space probe and ground stations could not be established [25].

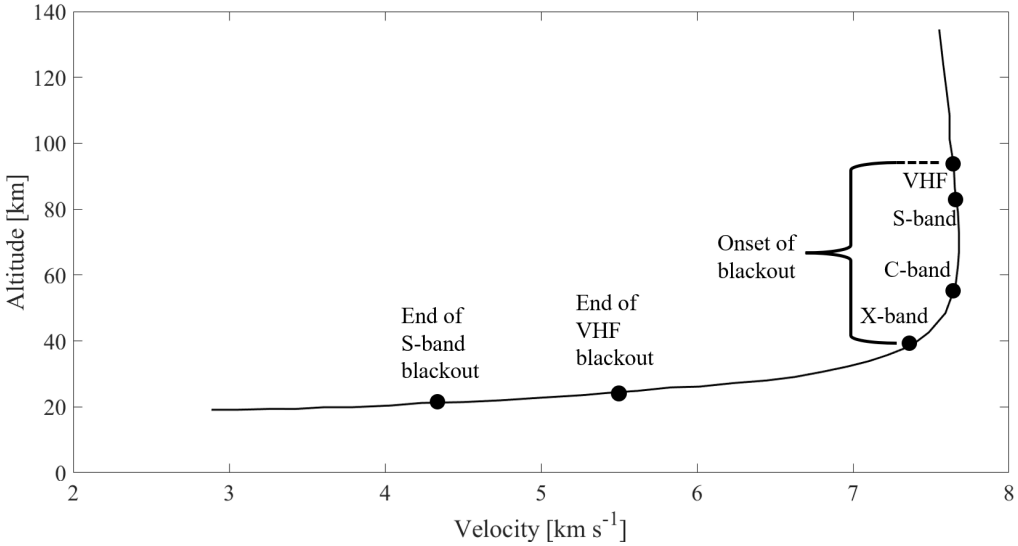

Figure 1.5: Re-entry trajectory of NASA RAM C-II vehicle including onset and end of radio blackout [23].

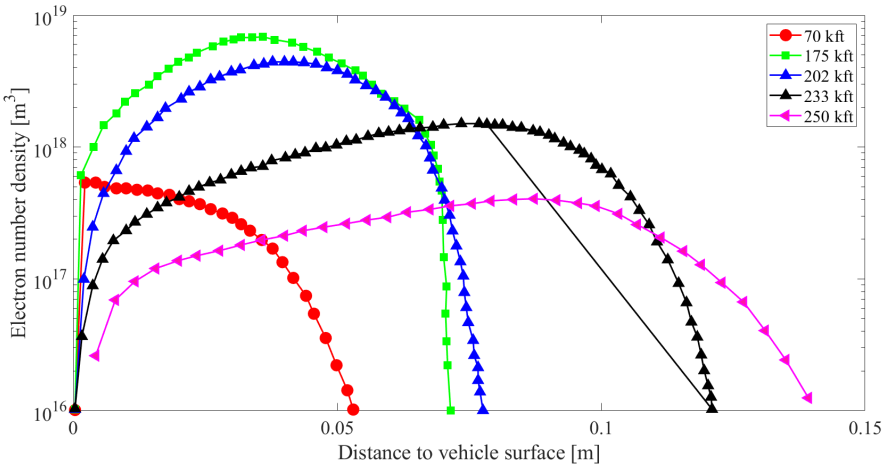

Figure 1.6: Re-entry trajectory of NASA RAM C-II vehicle including onset and end of radio blackout [24].

An examination of spacecraft entering the Martian atmosphere involved a retrospective assessment of the 30-second signal interruption experienced by the Mars Pathfinder spacecraft in 1997. This interruption occurred on an X-band direct-to-Earth (DTE) link and was primarily attributed to the presence of charged particles. The UHF relay connections between the Mars Science Laboratory (MSL) and both the Mars Reconnaissance Orbiter (MRO) and the Mars Express (MEX) experienced an approximately 70-second interval of signal deterioration. This period encompassed a mix of signal fades, referred to as brownout, and complete signal loss (blackout) [26]. The Atmospheric Reentry Demonstrator (ARD) is a 70 % down-scaled Apollo capsule launched in 1998. The radio signal toward the Tracking and Data Relay Satellite (TDRS) was not fully attenuated. The radio frequency to TDRS was 2.267 GHz. However, the Global Positioning System (GPS) signal with a radio frequency of 1.575 GHz was fully attenuated for about 300 seconds between an altitude of 90 km and 40 km. [27].

1.4 Mitigation methods for radio blackout

Techniques for mitigating radio communication blackouts were intensively investigated and summarized in [12, 23] and are listed below.

1.4.1 Aerodynamic Shaping

The aerodynamic shaping technique leverages the benefit of allowing certain electromagnetic waves with significantly longer wavelengths than the thickness of the plasma sheath to potentially pass through it. A streamlined body design results in the formation of a thinner and less ionized plasma sheath. An example of a sharp leading edge is the Sharp Edge Flight Experiment (SHEFEX). Sharp leading edges offer several advantages in terms of aerodynamic performance, such as minimal drag, reduced thrust requirements during ascent, and the ability to achieve greater crossrange during reentry, which in turn expands the reentry windows. However, it's important to note that they also face significant aerothermodynamic loads. Nevertheless, recent advancements in material development and the enhancement of layout and design calculation methods have prompted a reevaluation of the feasibility of sharp leading-edge concepts like SHEFEX for hypersonic flight [28].

1.4.2 Liquid Quenchant Injection

The Liquid Quenchant Injection method aims to reduce the electron number density by "quenching" the plasma by injecting liquids. NASA has successfully conducted flight demonstrations involving the injection of liquids into the airflow to mitigate blackout occurrences. One notable demonstration took place during the reentry of the Gemini 3 capsule. During the early stages of a water injection sequence, spanning an altitude range from 272 to 246 thousand feet, there was a substantial increase in signal strength as detected by VHF telemetry and VHF voice ground stations. Additionally, an improvement in C-band beacon signal strength was observed in the latter part of the water injection sequence, occurring between altitudes of 200 and 160 thousand feet. A comparison of calculated electron concentrations exhibited similar trends, with the assumption that the primary mechanism reducing electron concentration is recombination at or near the surface of water droplets. These values were inferred from the observed VHF attenuation data. The data collected from this flight provided compelling evidence that it is feasible to mitigate RF attenuation on a blunt body by injecting water into the flow field [23].

1.4.3 Solid Quenchant Injection

The Solid Quenchant Mitigation method is similar to the Liquid Quenchant Injection method but uses solid material to quench the plasma. Micron-sized particles are distributed and promise to absorb 96 % of the electrons [29]. Metal-oxide particles like tungsten-oxide, or alumina-oxide with dielectric properties are used according to [12].

1.4.4 Inflatable Aeroshell

Guolong He [14] mentions the Inflatable Aeroshell method for radio communication blackout mitigation. An inflatable vehicle experiences little to no impact from a blackout since it slows down at a higher altitude where the air density is significantly lower, resulting in a reduction in the plasma density created within the shock-wave [22]. A numerical analysis on an inflatable aeroshell entry vehicle concludes that the

radio blackout may be mitigated by placing the antenna in the aft of the inflating vehicle [30].

1.4.5 Resonant Transmission

Theoretical and experimental investigations have demonstrated that evanescent waves, boosted by resonance with a surface wave, can be harnessed to transmit visible-range electromagnetic radiation through metal films. This broader capacity to guide and manipulate evanescent waves within materials exhibiting negative permittivity and negative permeability often referred to as meta-materials, has emerged as a highly dynamic research area. Artificially generating a structure with layers featuring contrasting dielectric constants is achievable through composite arrangements composed of alternating metal films and semiconductors. In such structures, the electron density can be externally regulated using an electric field. Furthermore, an external magnetic field can be employed to manipulate the dielectric permittivity of the plasma. A somewhat analogous layer configuration, comprising multiple layers of dense and rarefied plasmas, can naturally occur in laboratory and space environments [31].

1.4.6 High Frequency and High Power

While raising the frequency typically decreases attenuation, it's important to note that higher frequencies are more susceptible to atmospheric and rain-induced attenuation. In practice, 10 GHz is often considered as an upper limit due to these factors. Boosting the transmission power from the vehicle faces constraints, particularly related to aperture breakdown. Typically, the breakdown powers fall within the range of hundreds of watts [23]. Implementing a relay method through a satellite to circumvent rain-induced attenuation, high-frequency communication remains one of the most viable solutions for addressing RF communication blackout [32].

1.4.7 Laser Communication

Laser communication in general has the advantage of a reduced power and mass requirement compared to radio frequencies due to the higher gain and low beam divergence and the reduced antenna sizes due to the small wavelengths [33]. In hypersonic flights, the self-focusing characteristic of plasma is beneficial to establish a communication link between the spacecraft and the control station using a laser beam. In this interaction between the laser beam and the plasma, the laser beam impacts an electron, causing it to accelerate in the direction of the laser's propagation. This acceleration results in a relativistic increase in the electron's mass, leading to an augmentation of the plasma's refractive index. As a consequence, the plasma behaves like a converging lens due to this refractive index rise. The increased electron velocity further aids in the convergence of waves [34].

1.4.8 Magnetic Window

Electrons possess the ability to respond to the electric field of an incoming electromagnetic wave when the wave's frequency is lower than the plasma frequency. In response, the electrons work to counteract the electric field, leading to the reflection of the incident wave at the plasma's surface. Nevertheless, by restricting the movement of electrons, it becomes possible to explore new modes of propagation,

allowing waves below the plasma frequency to traverse the plasma sheath. The magnetic window concept aims to leverage alterations in the dispersion relationship made feasible by an applied magnetic field, thus enabling bidirectional communication between the spacecraft and ground control as illustrated in Fig. 1.7. The RAM A-2 flight represents one of the few documented flights that tested the magnetic window mitigation technique, but unfortunately, limited information is available on the test outcome. The results demonstrate that right-handed polarized waves can propagate along magnetic field lines with intensities as low as 357 Gauss (G) through a plasma sheath with a density of 10^{12}cm^{-3}, without any attenuation, even at frequencies up to 1 GHz. Additionally, certain calculations suggest a 20 dB enhancement in signal reception with a magnetic field strength of 750 G. Initial findings from computations conducted at NASA Glenn Research Center show similar outcomes. However, it's worth noting that magnetic materials themselves may pose significant challenges for the magnetic window approach. Electromagnets come with inherent complexities, increased mass, and higher power requirements [12]. According to [23] 10000 G are required for vehicles with blunt leading edges (see also [35]) or 1500 G in case the Whistler mode (magnetic field cyclotron frequency matches the radio frequency) is used for communication (see also [36]). A magnet providing a 10000 G (1 Tesla) magnetic field estimated to weigh more than 500 kg [37].

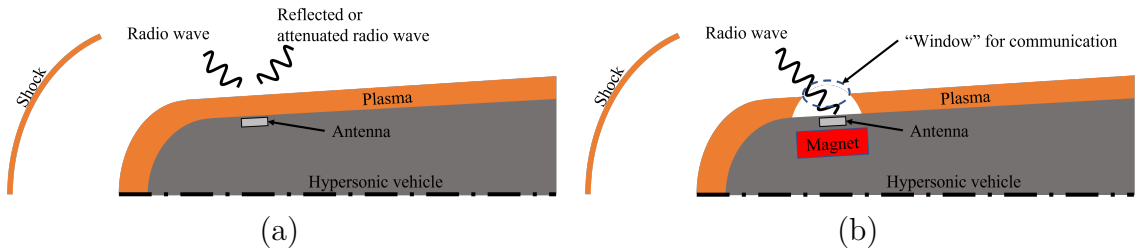

Figure 1.7: Illustration of RF interaction with a plasma sheath above the critical plasma frequency (a) without and (b) with an applied magnetic field and the created magnetic window [18].

1.5 Magnetohydrodynamic Enhanced Entry System for Space Transportation (MEESST)

The primary goal of MEESST is to create and validate a magnetic shielding prototype that reduces thermal loads and radio blackout during atmospheric entries. Additionally, it aims to enhance vehicle reusability, increase scientific data transmission during atmospheric entry, develop a lighter and safer protective system for various space missions, and advance numerical codes for simulating atmospheric entry and MHD interactions. Ultimately, MEESST seeks to shift the focus of entry vehicle shielding from material design to magnetic solutions, revolutionizing this field.

The MEESST project has received 3.5 million Euros in funding from the European Union's Horizon 2020 research and innovation programme under grant agreement No 899298. Its consortium consists of 10 project partners from Europe as can be seen in Fig. 1.8. KU Leuven (Belgium) is leading the project and contributing to the numerical analysis of the blackout problem. The von Karman Institute for

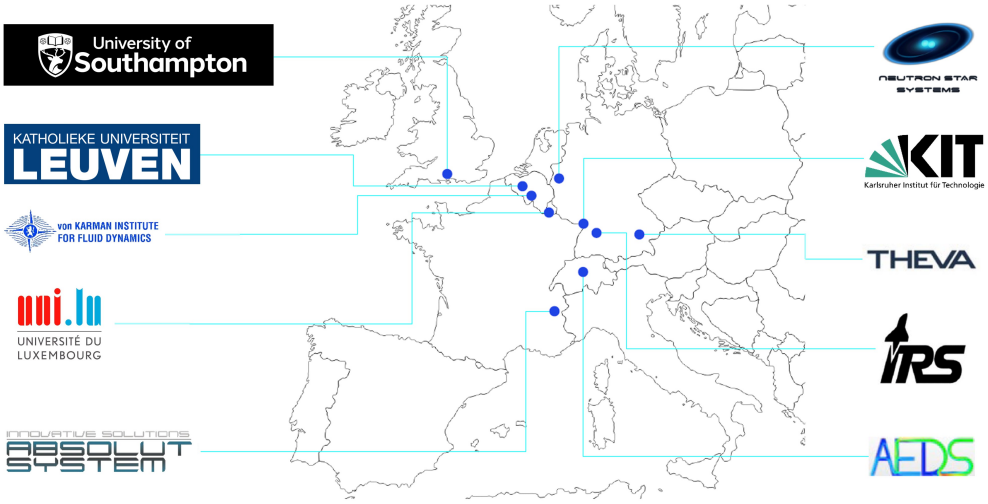

Figure 1.8: The MEESST consortium.

Fluid Dynamics (VKI) in Belgium is performing on-ground experiments in their plasma wind tunnel facility Plasmatron for the blackout analysis. The University of Southampton (UK) is also performing numerical analysis of the MHD fluid flow. The Karlsruhe Institute of Technology (KIT) and Theva Dünnschichttechnik GmbH from Germany are responsible for the HTS magnet. Absolut System (France) is developing a cryo-cooling system. The Institute of Space Systems (IRS) of the University of Stuttgart (Germany) is performing on-ground experiments in their plasma wind tunnel facility and numerical simulations for heat flux analysis. Advanced Engineering Design Solutions (AEDS) from Switzerland is performing radiation analysis and Neutron Star Systems (NSS) from Germany is responsible for marketing and dissemination. The University of Luxembourg is further developing the BlackOut Ray Tracer (BORAT) to numerically analyze the radio signal propagation in (magnetized) plasma including the signal characterization and validation of the numerical model with the on-ground experiments performed at VKI.

MEESST is pioneering an active Magnetohydrodynamic (MHD) system, aiming to modify plasma behavior during atmospheric entries. Utilizing novel cryo-cooled high-temperature superconducting magnets to generate an electromagnetic field that deflects plasma during the atmospheric entry, reducing heat loads and preserving radio communication. The use of superconductors enables powerful magnetic fields with lightweight magnets, surpassing traditional technology. Developing numerical codes to simulate magnetic-plasma fluid interaction and radio signal propagation with signal characterization will maximize design flexibility [38].

A schematic of the magnetic window effect is shown in Fig. 1.9. The volume around the magnet contains fewer free electrons. The reduction of the electron number density leads to a different dispersion relation, or refractive index, of the plasma in this region enabling the radio waves to propagate through the plasma.

The Lorentz force, caused by the applied magnetic field, acting on a plasma's charged particles influences the plasma's dynamics [38]. Superimposing a static magnetic field on a plasma alters the electromagnetic plasma properties leading to a reduced electron transverse motion, which reduces the interaction between the electrons and the electromagnetic wave [18, 39].

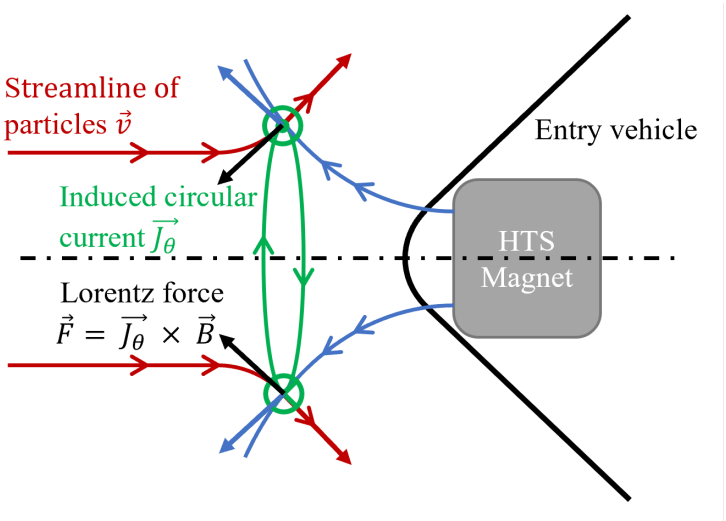

Figure 1.9: Illustration of the MEESST magnetic shield configuration [38].

1.6 Motivation

The physical phenomena involved in hypersonic flight and atmospheric entry are complex and cannot be solved analytically and require therefore a more advanced technique. Experiments recreating the exact flow conditions are cost- and time-extensive. Typical on-ground testing facilities have limitations and can only partially recreate the physics. Numerical models provide a fast, accurate, and cost-effective method to analyze such complex systems. Analyzing radio blackout is an interdisciplinary task, combining the high-speed, high-enthalpy fluid dynamics of plasma flows and the electromagnetic wave theory. In case a magnetic field is applied the magnetohydrodynamic effects increase the complexity. However, the numerical models require to be validated to show their consistency with the reality. Experiments in plasma wind tunnel (PWT) facilities can reproduce the plasma interaction of an atmospheric entry allowing to analyze radio blackout and heat flux. Different Computational Electro-Magnetics (CEM) models vary in their accuracy and cost-effectiveness. Full wave analysis models like the finite difference time domain (FDTD) method or the finite element method (FEM) are exact and powerful in low-frequency ranges but require larger computational cost and time. Asymptotic methods or high-frequency approximation methods like ray tracing require less computational costs and are better for large problems and multi-trajectory analysis. Atmospheric entry simulations usually require a large computational domain in all dimensions and the analysis of multiple trajectory points during EDL. A ray-tracing analysis also provides better insights into the problem and a better understanding of the physics, compared to a full wave analysis. Ray-tracing is a widely utilized method in various fields such as optics, wireless communication systems, and even in the study of fusion plasma. An overview of existing ray tracing models for fusion plasma can be found in this source [40]. This technique involves tracing the path of electromagnetic waves as they propagate through different mediums or interact with various surfaces, allowing us to characterize the signal behavior. Ray tracing offers valuable insights into signal propagation within a specific environment, enabling more efficient design and optimization of communication systems [41, 42]. Recently, new ray tracing methods have been introduced to investigate atmospheric entry scenarios,

particularly concerning blunt cones and inhomogeneous plasma slabs [43, 44].

Prior research concerning radio communication blackout on entry vehicles focused on the Mars Science Laboratory (MSL) and employed the Line-Of-Sight (LOS) method [45]. However, it is important to note that the LOS method lacks the capability to delve into the underlying physics of wave propagation. In contrast, two-dimensional ray tracing analyses have been conducted for both, the ExoMars Schiaparelli re-entry capsule [46, 47], and the Atmospheric Re-entry Demonstrator (ARD) [48]. Additionally, there is existing literature on three-dimensional ray tracing for the Intermediate eXperimental Vehicle (IXV) [49]. However, it is worth mentioning that neither of these studies addressed the unique context of magnetized plasma, nor offer a comprehensive analysis of signal propagation combined with signal characterization in scenarios involving arbitrary inhomogeneous plasma, diverse incident waves, and a wide range of fluid compositions. Additionally, some of these studies primarily concentrate on examining the transmitting side of the antenna mounted on the vehicle.

1.7 Importance of this work for society

The radio blackout phenomenon presents a significant challenge as it disrupts EM waves leading to the loss of one or several of the communication, navigation, control, and guidance systems during hypersonic flights. This unresolved issue has drawn increasing attention, especially as humanity plans to expand its exploration of the inner solar system (Moon and Mars), which lies in human nature. Transporting cargo and astronauts safely back to Earth and developing hypersonic passenger vehicles for rapid long-distance travel is in the interest of research worldwide. These endeavors require predictability and fail-safe measures to ensure the safety of astronauts, space travelers, and potential future hypersonic flight passengers.

The safety of lives is a basic requirement in this research. In the event of emergencies, data collection is crucial for safety and rescue missions, as well as for making improvements and preventing future incidents. Additionally, the emergence of hypersonic missiles poses a new threat, demanding swift, traceable, and maneuverable defense mechanisms to safeguard critical infrastructure and human lives.

The developed ray tracing algorithm offers a valuable tool for analyzing radio communication performance in advance, serving as a cost-effective and life-saving solution in these complex scenarios.

1.8 Scope of the thesis

The objective of this thesis is to examine the propagation of a radio signal through an arbitrary magnetized plasma medium by employing a ray tracing methodology and analyzing the altering signal characteristics including validation of the numerical tool with on-ground experiments. By introducing a magnetic field, alterations to the plasma properties are made to mitigate or potentially eliminate radio blackout. The analysis focuses on the ray propagation path and the signal characteristics along the path of the ray, providing a quantifiable assessment of how the plasma and the magnetic field influence the radio signal. The validation shall show the consistency of the model with the reality.

The following questions are tried to be answered:

1. How is the signal propagation path affected by a plasma?
2. How is the signal propagation path affected by a magnetized plasma?
3. How are the signal characteristics affected by a plasma?
4. How are the signal characteristics affected by a magnetized plasma?
5. Is the magnetic windowing method suitable to mitigate radio blackout?
6. Can the numerical tool be validated against experiments?

1.9 Thesis overview

The structure of this dissertation can be found in the road map in Fig. 1.10.

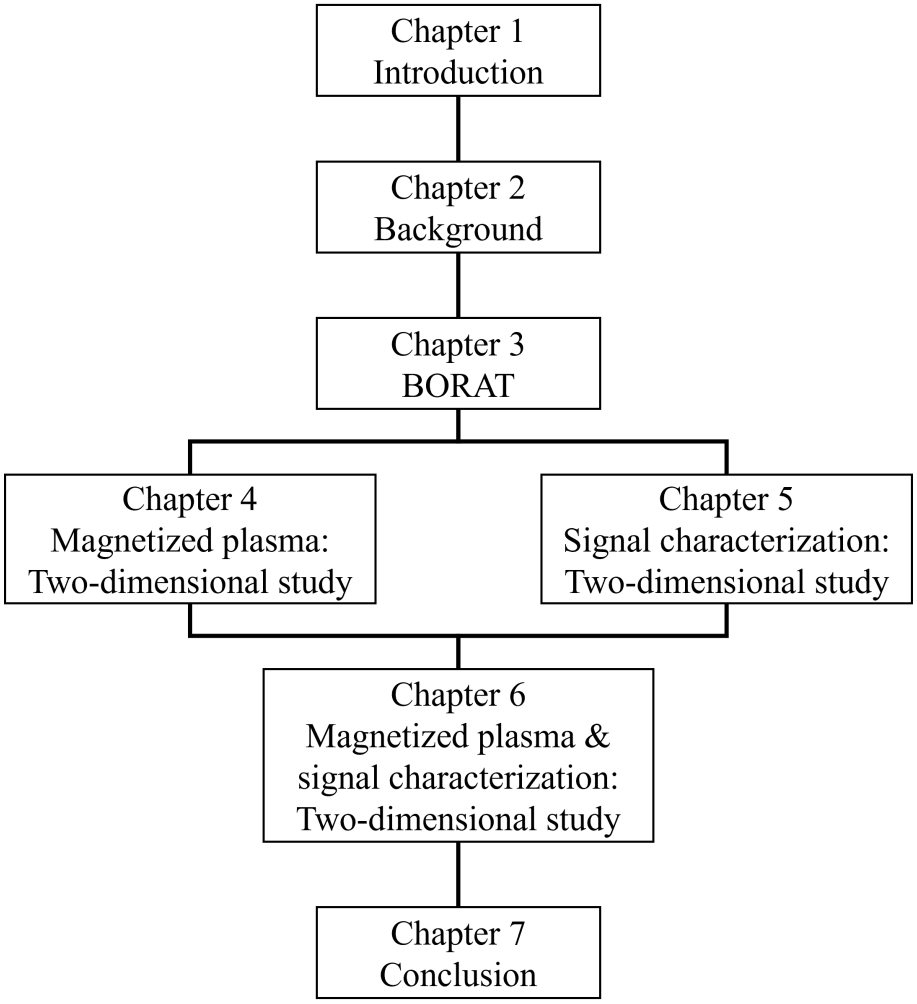

Figure 1.10: Road map of the thesis.

Chapter 1 Introduction In this introductory chapter, the thesis outlines its objectives and the importance of addressing the radio communication blackout issue associated with hypersonic flight and spacecraft reentry. The need for reliable communication, especially in future space exploration and hypersonic travel, is emphasized.

Chapter 2: Background Chapter 2 provides the necessary technical background and equations relevant to the research. This foundational information sets the stage for the subsequent chapters' analysis.

Chapter 3: BORAT (BlackOut RAy Tracer) Chapter 3 introduces BORAT, the tool developed to analyze the radio signal propagation. The chapter details BORAT's development stages and provides information about the solver used in the research.

Chapter 4: Magnetized Plasma: Two-Dimensional Study In this chapter, the impact of an applied magnetic field is analyzed using Knapp's test case. This represents the fourth version of BORAT. The research delves into how a magnetic field can mitigate radio blackout in plasma sheaths.

Chapter 5: Signal Characterization: Two-Dimensional Study Chapter 5 focuses on signal characterization, particularly in two-dimensional studies. It analyzes the energy along the ray path and the power transmitting between two antennas, primarily for non-magnetized plasma. Experimental validation of the results is carried out by comparing the numerical and experimental Scattering parameters.

Chapter 6: Magnetized Plasma & Signal Characterization: Two-Dimensional Study Chapter 6 represents the culmination of the research efforts. It combines the magnetized plasma solver with the signal characterization for 2D ray tracing. This chapter describes, verifies, and validates the model by comparing it with experimental data.

Chapter 7: Conclusion The final chapter of the thesis serves as a conclusion, summarizing the key findings, implications, and significance of the research. It provides insights into the potential applications and future directions based on the outcomes of the study.

This sequential structure guides the reader through the development, analysis, and findings of the research, ultimately addressing the critical issue of radio communication blackout in hypersonic flight and spacecraft reentry.

2 Background

This chapter contains the mathematics and physics background required to follow the thesis. The ray-tracing concept is introduced and put into context with other computational electromagnetics methods. The chapter is continued by a presentation of the ray tracer and the plasma modeling for non-magnetized and magnetized plasma. Lastly, the signal characterization is introduced and the developed model is explained.

Contents

2.1 Modeling of the signal propagation in plasma

It is of interest to know the path of energy flowing from a transmitter to a receiver. This is particularly important when analyzing EM wave propagation in complex domains. The feasibility of establishing a transmission between the sender and receiver and alterations in the ray propagation and signal (de-) focusing is subject to the advantages of a ray tracing analysis. The knowledge of the ray propagation path is required to predict the signal strength, phase, and polarization. Thinking of a ray path as a wave packet trajectory limited in frequency and space [50].

2.1.1 Electromagnetic radiation considered as rays

In this study, we employ a technique known as ray tracing, which is a computational electromagnetic method that provides calculations of path loss, received signal strength, angle of arrival/departure, and time delays of electromagnetic waves in complex propagation scenarios. This technique is used to analyze the phenomenon of radio communication blackout.

Ray tracing has its origin in the optics of light, specifically in the realm of ray optics. Here, the characterization of light relies on the depiction of rays emanating from light sources. From a mathematical perspective, rays are defined by both a position and a direction vector. These rays traverse through various media, with the medium's optical properties denoted by the refractive index. Within this framework, the behavior of light propagation is elucidated by monitoring alterations in the ray's direction and positional vectors within space.

In homogeneous media, ray propagation occurs along straight paths. At interfaces between different media, the laws of reflection and refraction come into play, guiding the trajectory of light rays. In graded-index media, the ray equation is employed to describe their path. These fundamental principles of ray optics can all be derived from Fermat's principle, which succinctly states that light rays follow the path of the least time.

Optical modeling founded on Fermat's principle forms the basis of ray optics. This branch of optics is often interchangeably referred to as geometrical optics, as the ray model fundamentally hinges on geometric concepts. This foundational understanding provides us with the necessary tools to analyze and optimize EM wave systems, making ray tracing an immensely popular technique, particularly in the context of lens systems.

So far, all the observed effects and quantities have been effectively explained within the framework of geometrical optics. However, our next objective is to incorporate the energetic effects occurring at the interface between two different media.

Fermat's principle solely concerns the trajectory of rays. Consequently, we cannot elucidate this surface effect within the confines of ray optics. In various optics textbooks, you can find derivations of the so-called Fresnel equations. These equations provide a mathematical expression for the transmission of energy, and the reflection of energy.

The derivation of these equations takes into account the propagation of an ideal electromagnetic plane wave through an ideal plane interface between two media with differing refractive indices. This solution relies on the fact that the components of the electric and magnetic fields in the plane interface are continuous functions. Fresnel's equations naturally follow from this. The concept of an ideal plane wave and the

continuity of the transverse field components stem from Maxwell's equations.

In contrast to geometrical optics, which is entirely based on Fermat's principle, we consider physical optics to be rooted in Maxwell's equations. Physical optics is a high-frequency approximation commonly used in optics, electrical engineering, and applied physics. It is an intermediate method between geometric optics, which ignores wave effects, and full wave electromagnetism, which is a precise theory. Physical optics allows for fast predictions with a limited level of accuracy proportional to the electrical size of the objects. Therefore, an explanation of losses at an interface between two media is derived from physical optics.

Integrating this into a ray tracing routine already leads to an algorithm that combines both ray and physical optics. Within this work, a combined algorithm of ray and physical optics is developed to analyze the EM wave path and properties. This combined approach is a comprehensive model of electromagnetic behavior. Ray tracing provides a detailed picture of how electromagnetic waves propagate and interact with their environment, while physical optics accounts for wave effects that are not captured by ray tracing. Meanwhile, computational electromagnetics provides the overall framework and tools for carrying out these simulations and analyses. This leads to more accurate and detailed predictions and analyses of electromagnetic phenomena[51].

2.1.2 Methods and Solvers for Ray Tracing

2.1.2.1 Snell's Law solver

Snell's Law serves as the fundamental equation in geometrical optics, representing the most simplified model for the propagation of electromagnetic waves within a medium. The ray tracing integration method based on Snell's law is an iterative stepwise approach that operates under the assumption of discrete and linear wave propagation over short distances. In this technique, rays originate from the antenna location, and their directions are determined by applying the principles of geometrical optics. Any deviation in the path of a ray from a straight line is calculated by utilizing Snell's law:

$$\mu_1 \sin \alpha_1 = \mu_2 \sin \alpha_2 \tag{2.1}$$

This algorithm operates as a marching-in-space method, where the signal is represented as a ray that progresses through a defined finite distance, referred to as the marching step [46]. A schematic of the procedure is illustrated in Fig. 2.1. The chosen step size within the domain corresponds to a region characterized by a constant refractive index, known as an iso-surface. At the boundaries of these iso-surfaces, Snell's Law is applied.

The marching technique initiates by advancing one step size from point P_1 to point $P_{1.5}$. The refractive index is determined at $P_{1.5}$ and then the algorithm retraces its steps backward to P_{temp} by advancing backward at half the step size. The radius of the iso-surface and its associated normal vector are determined at this point. Snell's Law is then applied between P_1 and $P_{1.5}$ to calculate the angle α_2. The algorithm subsequently advances to point P_2 by progressing half the value of the step size from P_{temp} at an angle α_2. This process continues until either the boundary of the domain is reached or the signal attenuation exceeds a predefined threshold.

It's important to note that the step size for the raytracer must be small enough to accurately resolve the refractive index gradients within the flowfield. This is ensured

through a step-size independence study.

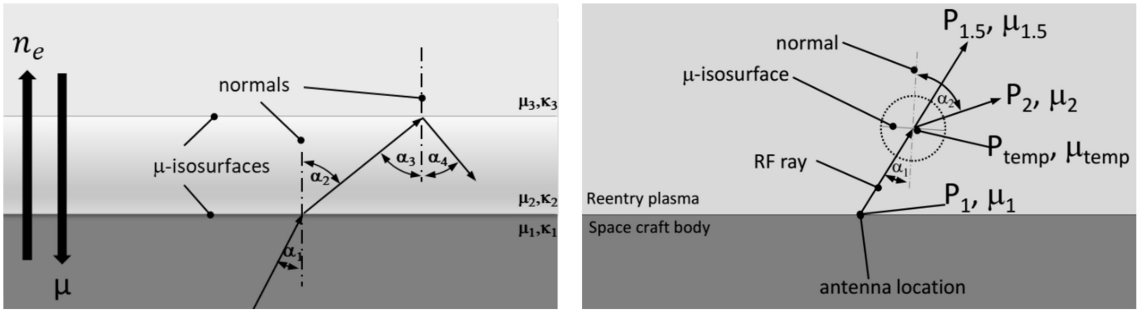

(a) (b)

Figure 2.1: Snell's law ray tracing solver: (a) Snell's law and (b) Marching in space technique.

In a typical reentry scenario, the rays originating from an antenna on the vehicle's surface transition from a region with lower electron densities (or a higher refractive index) to hotter regions characterized by higher electron concentrations (or a lower refractive index). This transition is analogous to light passing from water into air or from a denser optical medium to a less dense one. As the rays penetrate deeper into regions with higher electron concentrations, the refractive index μ decreases. If the electron density becomes significant enough to reduce μ to zero, a wave will be reflected, as described by equation 2.1 and depicted in Fig. 2.1. Consequently, Snell's law has no solution when the critical angle is exceeded, leading to the application of the law of reflection.

2.1.2.2 Eikonal solver - 3D

The Eikonal equation is the direct link between geometrical optics and EM waves theory and it is the theoretical starting point of any physical and advanced ray-tracing method. The Eikonal equation can be derived as an approximate solution of Maxwell's equations in the high-frequency limit [52, 53]. The Eikonal approximation is valid as long as medium properties vary slowly over a length-scale of the order of the signal wavelength [52, 53]. In an hypersonic entry plasma, this assumption can be considered valid in the whole wake region, while the front shock region, characterized by steep gradients, is generally not involved in EM propagation. At large frequencies, electric and magnetic fields may be expressed as:

$$\begin{aligned} E(r) &\simeq E_0 e^{-\imath k_0 S(r)} \\ H(r) &\simeq H_0 e^{-\imath k_0 S(r)}, \end{aligned} \tag{2.2}$$

where $S(r)$ is the normalised Eikonal phase function, defining the wave-front surface. Inserting the high frequency fields into Maxwell's equations leads to the Eikonal equation:

$$|\nabla S| = \mu, \tag{2.3}$$

that defines the relation between the direction of propagation of an EM wave and the refractive index μ of the medium.

A more convenient, but mathematically equivalent, form of the Eikonal equation may be obtained by rewriting the equation in characteristic form. The characteristic

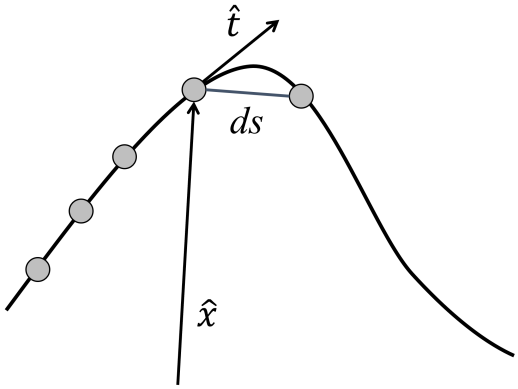

Figure 2.2: Ray trajectory for Eikonal algorithm.

solution of the Eikonal equation defines the rays trajectories. This may be achieved by introducing the normalized local wave vector $\xi = \nabla S$, that defines the propagation direction of the EM wave, and the position vector $x_i = (x_1, x_2)$. Using the arc-length s along the ray, one arrives at the following system of ordinary differential equations:

$$\begin{aligned} \frac{\partial x_i}{\partial s} &= \frac{\xi_i}{\mu}, \\ \frac{\partial \xi_i}{\partial s} &= \frac{\partial \mu}{\partial x_i}. \end{aligned} \tag{2.4}$$

The system (2.4), along with prescribed initial conditions in terms of position and angle of the emitted ray, allows to predict ray trajectories and states that the curvature of rays at each point is proportional to the gradient of the refractive index as illustrated in Fig. (2.2). The validity of characteristic solution of the Eikonal equation, namely the ray trajectories, falls in layers of plasma in which the value of the refractive index μ vanishes. These conditions are generally referred as cut-off conditions, and they are treated as localised reflection conditions. However, these conditions are rarely encountered, since in re-entry plasma problems high-density electron layers with steep variations are generally located in the front part of the vehicle, not designed for communication propagation.

From a theoretical point of view, from the Eikonal equation is possible to retrieve the Snell's law equation. In a uniform refractive index field medium, the gradient of the refractive index is equal to zero. Integrating the Eikonal equation leads to a linear variation in space of the ray trajectory:

$$\nabla n = 0 \rightarrow n = const \rightarrow \frac{\partial^2 x_i}{\partial s^2} = 0 \rightarrow \bar{x} = \bar{a}s + \bar{b} \tag{2.5}$$

Thus, the Snell's law can be considered as the local solution of the Eikonal equation at the interface between two medium at different refractive index, in which a straight ray deviates depending on the refractive index discontinuity at the interface. The Eikonal formulation presents three main advantages. First of all, second order continuity in refractive index of the Eikonal formulation allows us to increase the ray tracing solution accuracy with respect to the first order ray tracing Snell's law algorithm. Second, the Ordinary Differential Equations (ODE) system resulted from the Eikonal equation (2.4) is solved using a Runge-Kutta method (RK4) with

adaptive integration step refinement. This leads to a performance increase up to 100x times with respect to the previous marching in space method. Last, one of the main advantages of the Eikonal system of equation is the decoupled form of the space variables, allowing algorithmic simplicity that led to a straightforward development of a 3D version of the solver. Figure (2.3) summarizes the functionality of the Eikonal solver.

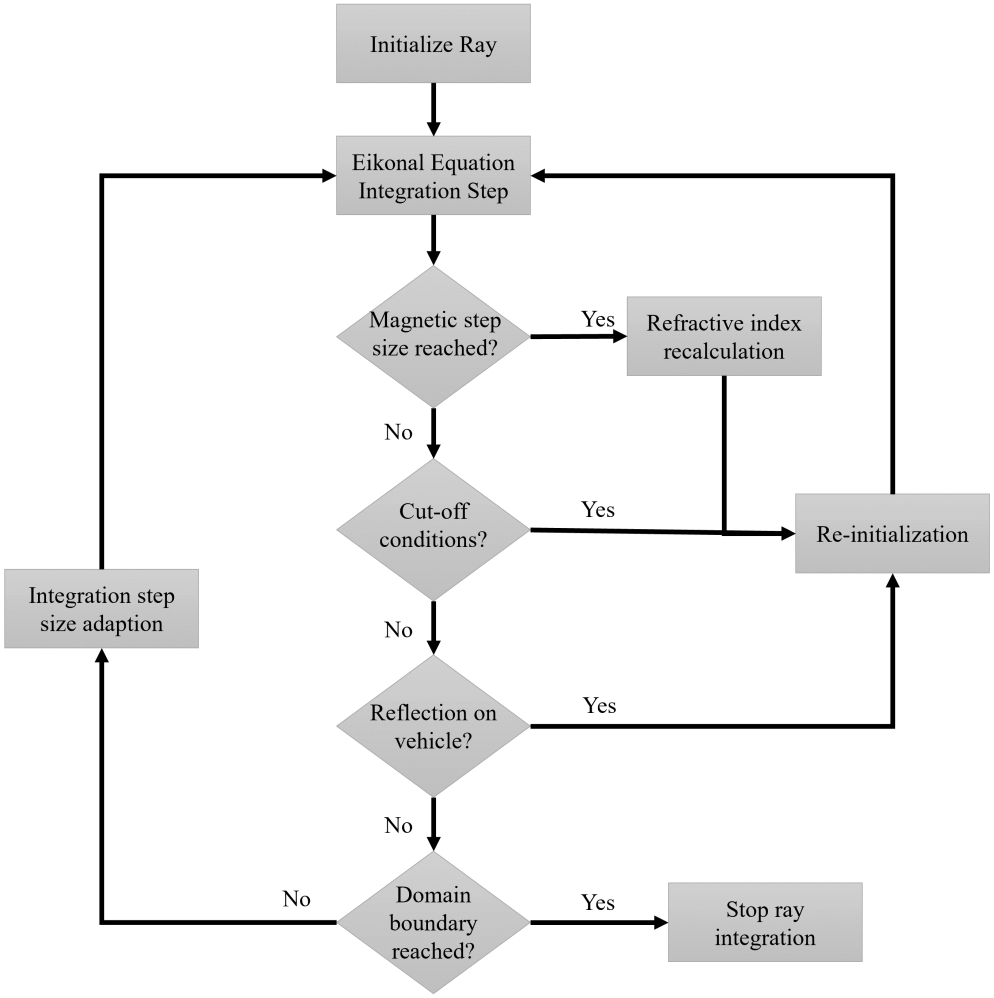

Figure 2.3: Eikonal ray tracing algorithm.

Refractive index gradients, which are needed for Eikonal equation integration, are reconstructed from the plasma field with a first order approximation:

$$\mu\left(x,y,z\right)=\frac{\partial\mu}{\partial x}x+\frac{\partial\mu}{\partial y}y+\frac{\partial\mu}{\partial z}z+\mu_0 \tag{2.6}$$

The refractive index $\mu(x,y,z)$ is assumed to be a piece-wise planar function over the computational domain. For each computational domain mesh element, the reconstructed gradient is computed by solving the following system of equation:

$$\begin{bmatrix} x_1 & y_1 & z_1 & 1 \\ x_2 & y_2 & z_2 & 1 \\ x_3 & y_3 & z_3 & 1 \end{bmatrix} \begin{bmatrix} \frac{\partial \mu}{\partial x} \\ \frac{\partial \mu}{\partial y} \\ \frac{\partial \mu}{\partial z} \\ \mu\left(x, y, z\right) \end{bmatrix} = \begin{bmatrix} \mu(x_1, y_1, z_1) \\ \mu(x_2, y_2, z_2) \\ \mu(x_3, y_3, z_3) \end{bmatrix} \tag{2.7}$$

where:

$$\nabla \mu|_T = \begin{bmatrix} \frac{\partial \mu}{\partial x} & \frac{\partial \mu}{\partial y} & \frac{\partial \mu}{\partial z} \end{bmatrix}. \tag{2.8}$$

The partial derivative at each node is the weighted sum of each of the partial derivatives of the triangles associated with that node. The weightings $\omega_i = A_i/A_{tot}$ are the areas of each triangle divided by the total area of all triangles associated with that node.

$$\nabla \mu|_n = \sum_{i=1}^{k} \omega_i \nabla \mu|_{T_i} \tag{2.9}$$

A more detailed description of the Eikonal solver can be found here: [52].

2.1.2.3 Eikonal solver - 2D

Equations 2.6 to 2.8 reduce to the following form for two dimensional applications, where the z-component of the refractive index gradients is canceled out

$$\mu\left(x, y, z\right) = \frac{\partial \mu}{\partial x} x + \frac{\partial \mu}{\partial y} y + \mu_0 \tag{2.10}$$

$$\begin{bmatrix} x_1 & y_1 & 1 \\ x_2 & y_2 & 1 \\ x_3 & y_3 & 1 \end{bmatrix} \begin{bmatrix} \frac{\partial \mu}{\partial x} \\ \frac{\partial \mu}{\partial y} \\ \mu\left(x, y\right) \end{bmatrix} = \begin{bmatrix} \mu(x_1, y_1) \\ \mu(x_2, y_2) \\ \mu(x_3, y_3) \end{bmatrix} \tag{2.11}$$

where:

$$\nabla \mu|_T = \begin{bmatrix} \frac{\partial \mu}{\partial x} & \frac{\partial \mu}{\partial y} \end{bmatrix}. \tag{2.12}$$

2.1.2.4 Eikonal solver for magnetized plasma

The above-described principle of the Eikonal solver applies also to magnetized plasma. Besides the more complex refractive index calculation, an additional event needs to be implemented. The dependency of the refractive index on the angle between the wave vector and the magnetic field vector leads to the requirement, that the refractive index field needs to be recalculated after each time step. This slows down the initial mentioned performance but can be compensated with a parallel ray path computation. Additionally, in the case of bi-refractions, a right-hand polarized and left-hand polarized will continue at a refraction position. The functionality of the Eikonal solver for magnetized plasma is sketched in Fig. (2.4).

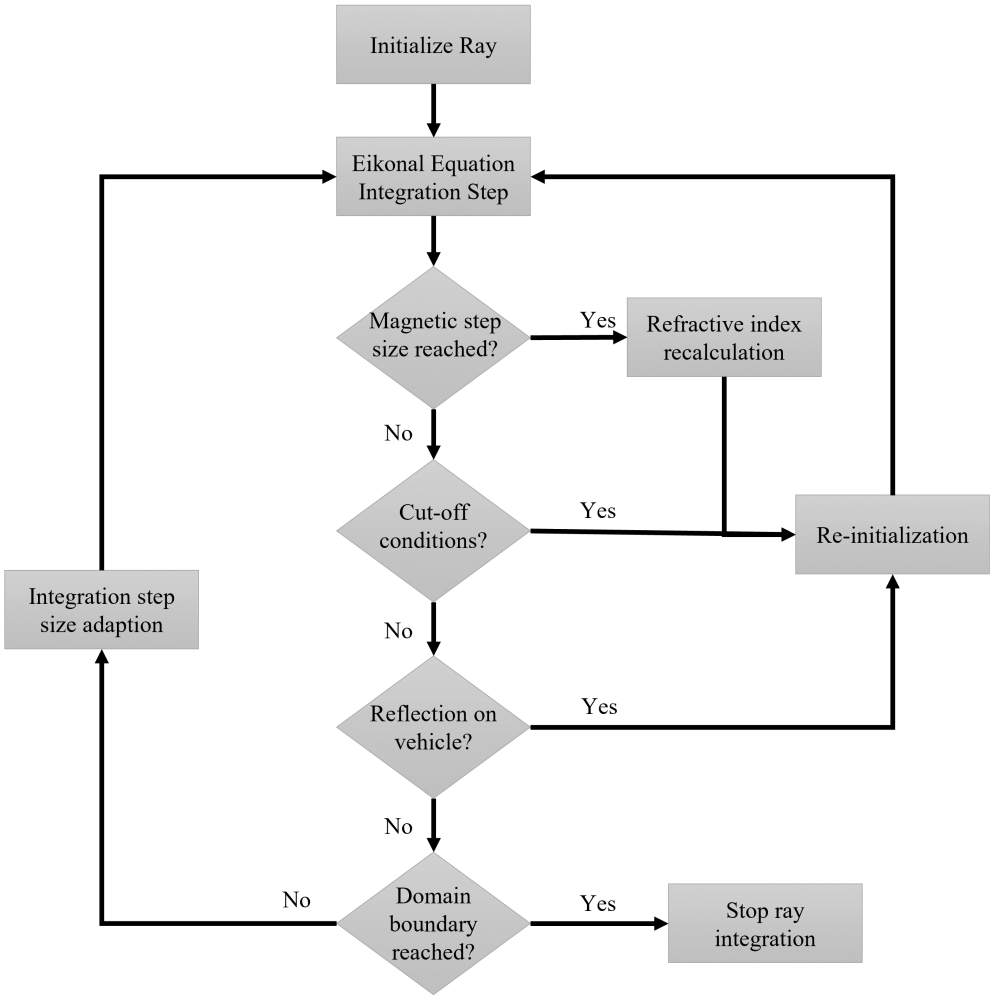

Figure 2.4: Eikonal ray tracing algorithm for magnetized plasma.

2.1.3 Plasma modeling

2.1.3.1 Relevant plasma properties for signal propagation

The cold plasma approximation is valid for atmospheric entry or hypersonic flow plasma since we are concerned only by radio signals traveling close to the speed of light in plasma with a thermal electron velocity much smaller than the speed of light [54]. The full Appleton-Hartree equation (2.13) describes the refractive index for magnetized cold plasma including collisions. This form of the Appleton-Hartree equation is suitable to show the relation between the wave vector and the magnetic field by including the angle Θ between the wave vector and the magnetic field [55]:

$$n^2 = (\mu - \chi i)^2 = 1 - \frac{X}{1 - Zi - \frac{Y^2 sin^2(\Theta)}{2\left(1 - X - Zi\right)} \pm \sqrt{\frac{Y^4 sin^4(\Theta)}{4\left(1 - X - Zi\right)^2} + Y^2 cos^2(\Theta)}}. \tag{2.13}$$

with:

$$\begin{aligned} X &= e^2 N_e / \left(\epsilon_0 m \omega^2\right) \\ Y &= eB / \left(m\omega\right) \\ Z &= \nu / \omega \\ \omega &= 2\pi f \end{aligned} \tag{2.14}$$

where e denotes the electron charge, N_e the electron number density, ϵ_0 the vacuum permittivity, m_e the electron mass, ν the electron-heavy particle collision frequency, f for the communication system transmission frequency and B is the magnetic field. The $\pm$ sign represents the resulting refractive index of "+" for the ordinary wave and "-" for the extraordinary wave [56]. It is worth mentioning that the wave vector is independent of the refractive index in the cold plasma approximation [54]. The refractive index might change while the electromagnetic wave is propagating through the magnetized plasma because of the link between the wave vector and the magnetic field through the angle Θ. Additionally, the refractive index values are not limited between 0 and 1 if compared to the collision-free non-magnetized solution of the Appleton-Hartree equation and can become complex [50].

2.1.3.1.1 Birefringence in anisotropic (magnetized) plasma Birefringence is an optical property exhibited by materials where the refractive index varies depending on the polarization and direction of propagation. In the presence of a magnetic field, plasma behaves as a birefringent medium, necessitating a detailed exploration of its characteristics. These properties encompass the division of a plane polarized wave into ordinary and extraordinary waves, alongside deviations in the direction of energy flow relative to the phase propagation [50]. Conversely, a finite magnetic field introduces anisotropy, inducing birefringence during wave propagation [54]. This phenomenon results in double refraction, where an incident ray splits into two rays with different polarizations, each traveling along slightly divergent paths.

2.1.3.2 Magnetized plasma, without collisions

Neglecting collisions between heavy particles and electrons ($Z{\sim}0$, meaning $\nu \ll f$) leads to the reduced Appleton-Hartree eq. after Hutchinson [54]

$$n^2 = (\mu - \chi i)^2 = 1 - \frac{X}{1 - \frac{Y^2 sin^2(\Theta)}{2\,(1-X)} \pm \sqrt{\frac{Y^4 sin^4(\Theta)}{4\,(1-X)^2} + Y^2 cos^2(\Theta)}}., \tag{2.15}$$

with

$$\begin{aligned} X &= e^2 N_e / \left(\epsilon_0 m_e \omega^2\right), \\ Y &= eB / (m\omega) \\ \omega &= 2\pi f. \end{aligned} \tag{2.16}$$

and the angle Θ between the wave vector and the magnetic field. It is worth mentioning that the wave vector $\mathbf{k}$ is independent of the refractive index in the cold plasma approximation. According to literature [46, 47] neglecting collisions in plasma is a good approximation to describe blackout phenomena during re-entry. However, an increased sensitivity against collisions for magnetized plasma is mentioned as well [56]. Applying strong magnetic fields will require a comparison to estimate if collisions need to be considered.

The dependency of the refractive index on the angle between the ray vector and the B-field vector leads to a coupling of the refractive index and the ray position and ray angle. Therefore, the refractive index needs to be recalculated after each step (see 2.1.2.4).

2.1.3.3 Non-magnetized plasma, with collisions

One reduced form of the Appleton-Hartree equation is the unmagnetized cold plasma form, in which the effect of magnetic fields is neglected in the computation of the refractive index. This is the general case of atmospheric re-entry plasma, in which no magnetic fields are applied to the spacecraft and planetary magnetic fields can be neglected. In this case, $B = 0$, leading to:

$$n^2 = (\mu - \chi i)^2 = 1 - \frac{X}{1 - Zi} \tag{2.17}$$

Solving this equation for μ and χ leads to:

$$\mu^2 = \frac{1}{2}\left(1 - \frac{X}{1+Z^2}\right) + \frac{1}{2}\sqrt{1 - 2\frac{X}{1+Z^2} + \frac{X^2}{1+Z^2}} \tag{2.18}$$

and

$$\chi^2 = -\frac{1}{2}\left(1 - \frac{X}{1+Z^2}\right) + \frac{1}{2}\sqrt{1 - 2\frac{X}{1+Z^2} + \frac{X^2}{1+Z^2}} \tag{2.19}$$

The resulting equation becomes a function of X, which is a direct function of the electron number density, and Z, which is a direct function of the collision frequency ν.

2.1.3.4 Non-magnetized plasma, without collisions

In case collisions are negligible and no magnetic field is applied the equation to calculate the refractive index simplifies as follows

$$n = \mu = \sqrt{1 - X} = \sqrt{1 - \left(\frac{f_p}{f}\right)^2}, \tag{2.20}$$

with

$$f_p = \sqrt{kN_e}, \text{ and} \tag{2.21}$$

$$k = e^2 / \left(4\pi^2 \epsilon_0 m_e\right). \tag{2.22}$$

The refractive index becomes a function of the plasma frequency f_p and the radio frequency f in Hz. The refractive index for non-magnetized plasma neglecting collisions is a real number between 0 and 1. The value for the refractive index decreases for a given antenna frequency f if the electron density N_e is increasing, i.e., while the EM wave is propagating into regions with higher electron density concentration the refractive index μ becomes smaller.

2.2 Signal characterization

The following section shall give an introduction into antenna theory and their properties as well as radio signal behavior in plasma relevant to this research.

2.2.1 Antenna and signal theory

According to Webster's Dictionary, an antenna is described as "typically a metallic apparatus, such as a rod or wire, used for emitting or detecting radio waves." The IEEE Standard Definitions of Terms for Antennas (IEEE Std 145–1983) similarly defines an antenna, or aerial, as "a device for emitting or detecting radio waves." Essentially, the antenna serves as the interface between open space and a guiding mechanism. [2]. The transmission line, which can be in the shape of a coaxial cable or a hollow pipe (waveguide), serves the purpose of conveying electromagnetic energy either from the transmitter to the antenna or from the antenna to the receiver. When energy is transferred from the source to the antenna, it forms a transmitting antenna; conversely, when it travels from the antenna to the receiver, it constitutes a receiving antenna. Beyond its role in receiving or transmitting energy, an antenna within an advanced wireless system typically needs to optimize or focus radiation energy in specific directions while minimizing it in others. Thus, the antenna serves as both a directional and probing device. Consequently, it must adopt various forms to suit specific requirements, potentially appearing as a conducting wire, an aperture, a patch, an array of elements, a reflector, a lens, and more. Within wireless communication systems, the antenna stands as one of the most pivotal components. An effective antenna design has the potential to alleviate system demands and enhance overall system performance [2].

2.2.1.1 Antenna types

In the following, the most important different antenna types will be briefly introduced.

Wire antennas Wire antennas are one of the most popular antenna designs. Figure 2.5 illustrates different shapes of wire antennas, including the straight wire (dipole), loop, and helix. Loop antennas are not limited to circular shapes; they can also be rectangular, square, elliptical, or adopt any other configuration. Among these, the circular loop is the most prevalent due to its straightforward construction [2].

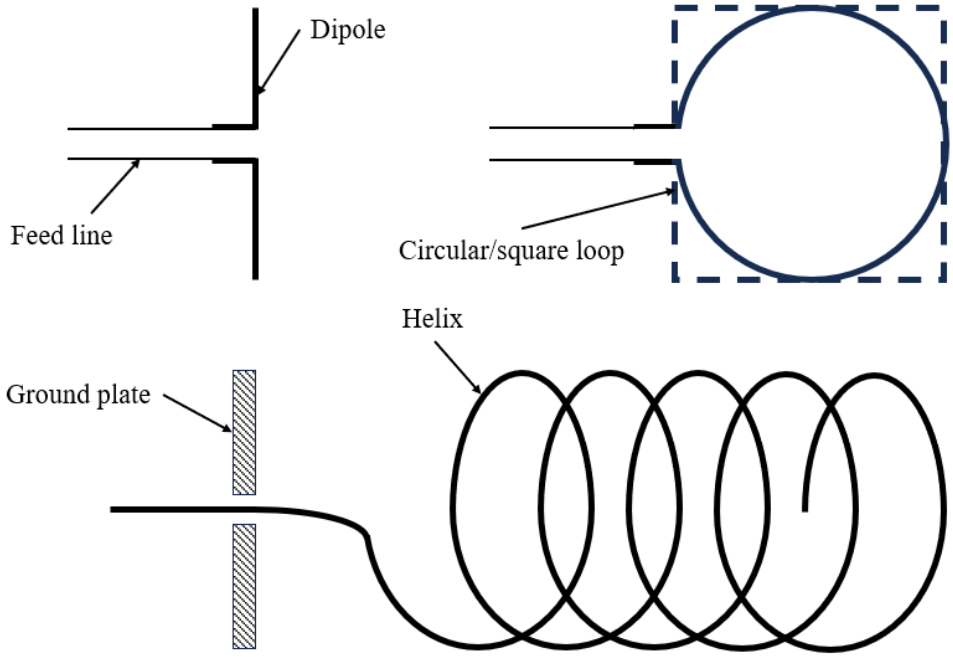

Figure 2.5: Examples of wire antennas.

Aperture antennas Aperture antennas are becoming more common due to the increasing demand for more sophisticated antenna forms and the use of higher frequencies. aperture antennas are used for aircraft and spacecraft. Their advantage is that they can be mounted on the vehicle surface and covered with a dielectric material to protect the antenna from the environment. Typical designs are the horn antennas (conical/rectangular) and the rectangular waveguide as shown in Fig. 2.6 [2].

Microstrip antennas Microstrip antennas are composed of a metallic patch placed on a grounded substrate, with various configurations depicted in Fig. 2.7. However, rectangular and circular patches, are favored due to their ease of analysis and fabrication, alongside their appealing radiation characteristics, particularly low cross-polarization radiation. These antennas boast a low profile, adaptability to both planar and non-planar surfaces, simplicity and affordability in fabrication through contemporary printed-circuit technology, mechanical robustness when affixed to rigid surfaces, compatibility with Monolithic Microwave Integrated Circuit (MMIC) designs, and remarkable versatility regarding resonant frequency, polarization, pattern,

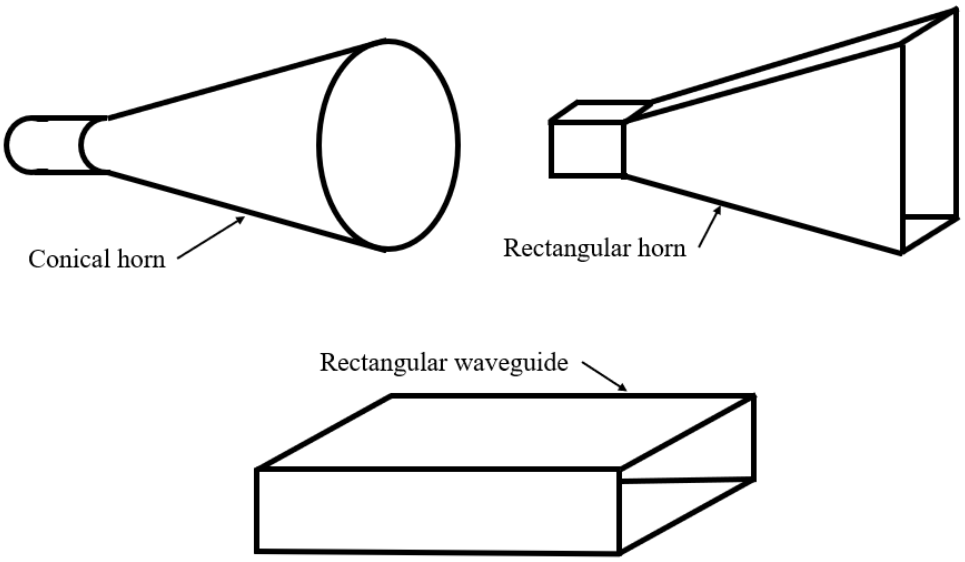

Figure 2.6: Examples of aperture antennas.

and impedance. Such antennas find application in diverse settings, including high-performance aircraft, spacecraft, satellites, missiles, automobiles, and even portable devices [2].

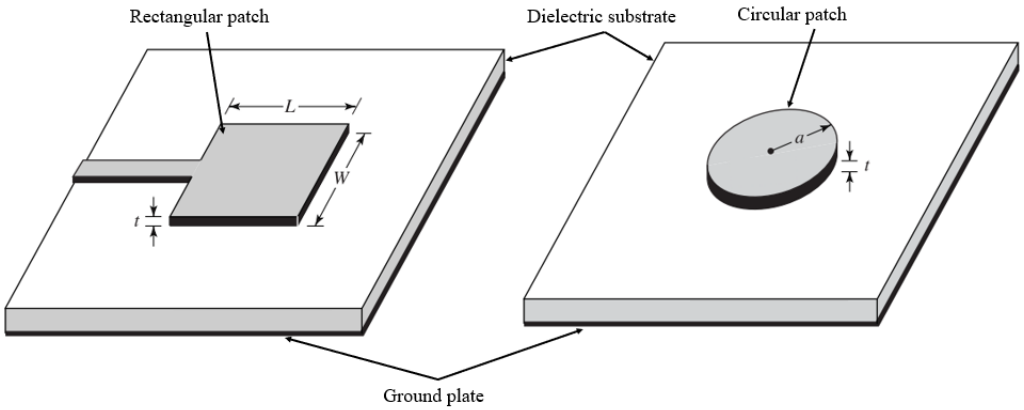

Figure 2.7: Examples of microstrip (patch) antennas.

Antenna arrays Numerous applications demand radiation characteristics that might not be attainable with a single element. However, by arranging a group of radiating elements in both electrical and geometrical configurations (referred to as an array), it becomes feasible to achieve the desired radiation properties. The array's configuration may be engineered so that radiation from the elements combines to produce maximum radiation in specific directions while minimizing it in others, or as otherwise desired. Common examples of arrays include the Yagi-Uda array and microstrip antenna arrays. Array configurations can include rectangular, linear, circular, and other variations [2].

Reflector and lens antennas Advancements in antenna theory owe much to the successes in outer space exploration. Communicating across vast distances necessitated the use of sophisticated antenna designs capable of transmitting and

receiving signals spanning millions of miles. A commonly employed antenna type for such tasks is the parabolic reflector, often constructed with diameters exceeding 305 meters to achieve the high gain essential for long-distance signal transmission and reception. Another reflector type, though less prevalent than the parabolic variant, is the corner reflector [2].

Furthermore, lens antennas are notable for their ability to convert divergent energy into plane waves due to the material of the lenses. While they serve similar purposes as parabolic reflectors, especially at higher frequencies, their size and weight become impractical at lower frequencies. Lens antennas are categorized based on their construction material or geometric shape [2].

2.2.1.2 Antenna parameters

In order to assess an antenna's performance, it is essential to define various parameters. While some of these parameters are interconnected, not all of them need to be specified to fully describe the antenna's performance [2].

Radiation pattern An antenna radiation pattern, or simply antenna pattern, is defined as a mathematical function or graphical representation depicting the radiation characteristics of the antenna concerning spatial coordinates. Typically determined in the far-field region, this pattern is expressed as a function of directional coordinates and encompasses various radiation properties such as power flux density, radiation intensity, field strength, directivity, phase, or polarization [2].

Of particular interest is the spatial distribution of radiated energy in two or three dimensions concerning the observer's position along a path or surface with constant radius. The trace of the received electric (or magnetic) field at a constant radius is referred to as the amplitude field pattern, while a graph illustrating the spatial variation of power density along a constant radius is termed an amplitude power pattern. Often, both field and power patterns are normalized relative to their maximum values, resulting in normalized field and power patterns [2].

Moreover, the power pattern is commonly depicted on a logarithmic scale or, more frequently, in decibels (dB). This scale is preferred as it effectively highlights details of the pattern, particularly those with very low values, often referred to as minor lobes. According to [2] the different antenna patterns are:

- **Field Pattern**: This typically represents a plot of the magnitude of the electric or magnetic field as a function of the angular space. It provides information about the strength of the field in different directions.
- **Power Pattern (in linear scale)**: This typically represents a plot of the square of the magnitude of the electric or magnetic field as a function of the angular space. It provides information about the power density in different directions. Since power is proportional to the square of the field magnitude, the power pattern is derived from the field pattern.
- **Power Pattern (in dB)**: This represents the magnitude of the electric or magnetic field, in decibels, as a function of the angular space. The use of decibels allows for a more manageable range of numbers to work with, especially when dealing with very large or very small values.

Each type of pattern provides different insights into the behavior of the electromagnetic field, and the choice of pattern depends on the specific requirements of the analysis [57]. Examples of these antenna patterns are shown in Fig. 2.8 for the patch antenna used for verification in chapter 5. The main lobe points towards 90° and

the back lobe towards 270°. This specific antenna has no side lobe/miner lobes.

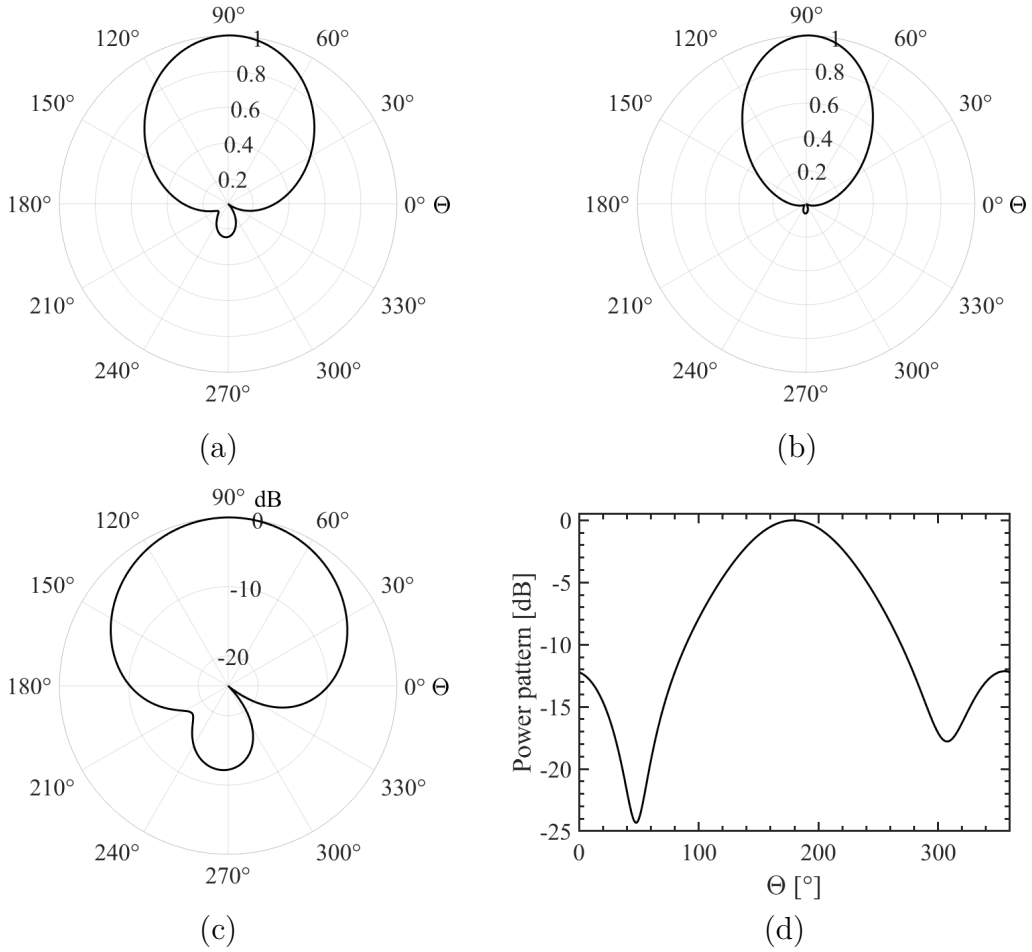

Figure 2.8: Two-dimensional normalized (a) field pattern (linear), (b) power pattern (linear), and (c) power pattern (dB) in polar coordinates, and (d) power pattern (dB) in rectangular coordinates of the 2.4 GHz patch antenna at $\Phi = 0°$.

Beamwidth and aperture angle The beamwidth of an antenna is a crucial performance metric and is often balanced against the side lobe level. In other words, as the beamwidth narrows, the side lobe tends to increase, and vice versa [2].

The beamwidth also serves to illustrate the antenna's ability to differentiate between two nearby radiation sources or radar targets [2].

The Half-Power Beamwidth (HPBW) is defined by the IEEE as the angle, within a plane that contains the maximum beam direction, between the two directions where the radiation intensity is half the maximum value of the beam (-3 dB) [2].

Another significant beamwidth is the First-Null Beamwidth (FNBW), which is the angular distance between the first nulls of the pattern [2].

The aperture angle refers to the angle at which the radio signal is radiating in two dimensions. Considering an aperture angle of 180° in the air might lead to different aperture angles after propagating through a plasma domain due to refraction and reflection processes. Since the initial radiation pattern might be significantly disturbed and no clear beamwidth will be established the term aperture angle is more useful.

Radiation fields The area around an antenna is typically divided into three distinct regions: the reactive near-field, the radiating near-field (also known as the Fresnel region), and the far-field (or Fraunhofer region). Each region is named based on the structure of the field within it. While there are no sudden changes in the field configurations at the boundaries, each region has unique characteristics [2].

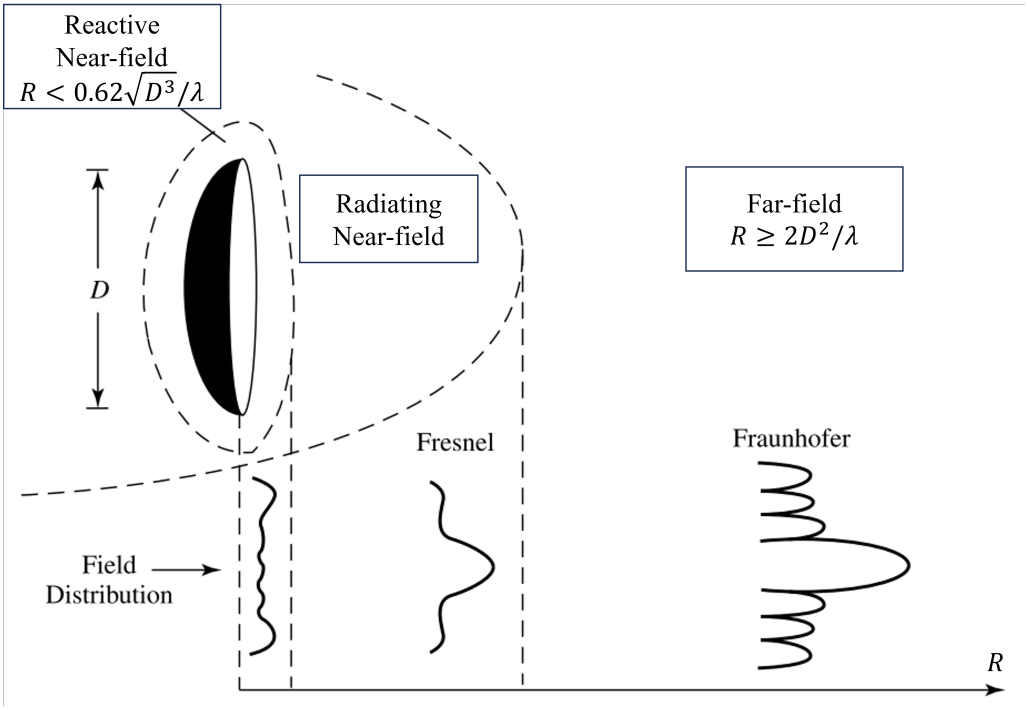

Figure 2.9: Usual transformations in the shape of an antenna's amplitude pattern from the reactive near field progressing towards the far field [2]. (Source: C. A. Balanis, Antenna theory: analysis and design. Hoboken, New Jersey: Wiley, fourth edition. ed., 2016 - 2016.

The reactive near-field region is the area immediately surrounding the antenna where the reactive field is dominant. For most antennas, the outer boundary of this region is usually considered to be at a distance $R < 0.62\sqrt{D^3}/\lambda$ from the antenna surface, where λ represents the wavelength and D is the largest dimension of the antenna [2].

The radiating near-field, or Fresnel region, is the area between the reactive near-field and the far-field regions. In this region, radiation fields predominate and the angular field distribution depends on the distance from the antenna. If the antenna's maximum dimension is not large compared to the wavelength, this region may not exist [2].

The far-field, or Fraunhofer region, is where the field components are essentially transverse and the angular distribution is independent of the radial distance from the antenna. The inner boundary is typically taken to be the radial distance $R = 2D^2/\lambda$ and the outer boundary is at infinity [2].

As the observation distance varies from the reactive near-field to the far-field, the amplitude pattern of an antenna changes in shape due to variations in the fields, both in magnitude and phase. In the reactive near-field region, the pattern is more spread out and nearly uniform, with slight variations. As the observation moves to the radiating near-field (Fresnel) region, the pattern begins to smooth and form lobes.

In the far-field (Fraunhofer) region, the pattern is well-formed, usually consisting of a few minor lobes and one or more major lobes (see Fig. 2.9) [2].

Power density & radiation intensity Electromagnetic waves transmit information from one point to another, either through a wireless medium or a guiding structure. It is therefore reasonable to associate power and energy with electromagnetic fields. The power associated with an electromagnetic wave is represented by the instantaneous Poynting vector [2]. Since energy must flow over a surface a power radiated in a single direction is zero. Therefore the power density, which is the power per unit area, and is measured in SI base units of W/m^2 is required.

According to [58] the real (not complex) power density is calculated as follows:

$$S(\mathbf{r}, \Theta, \Phi) = \frac{|E(\mathbf{r}, \Theta, \Phi)|^2}{2\sqrt{\frac{\mu_0 \mu_r}{\epsilon_0 \epsilon_r}}}, \tag{2.23}$$

where E is the electric field of the radio signal, μ_0 and ϵ_0 are the permeability and permittivity of vacuum, respectively, and μ_r and ϵ_r the permeability and permittivity of the medium. The factor 1/2 appears because the electric field value represents the amplitude and for the power density the root means square (RMS) value need to be considered.

The Radiation intensity U is defined as the power that an antenna radiates per unit solid angle in a specific direction and is simply the multiplication of the radiation density S by the square of the distance r according to Eq. 2.24:

$$U(\Theta, \Phi) = r^2 S(\mathbf{r}, \Theta, \Phi) = \frac{r^2}{2\sqrt{\frac{\mu_0 \mu_r}{\epsilon_0 \epsilon_r}}} |E(\mathbf{r}, \Theta, \Phi)|^2. \tag{2.24}$$

Therefore, a direct correlation between the radiation intensity U and the power density S exists. The power density in the far field is inversely proportional to the square of the distance from the source ($1/r^2$), given that the magnitude of the far field is dependent on r as $1/r$. Consequently, the radiation intensity U is solely dependent on the direction (Θ, Φ) and not on the distance r. The radiation intensity also has a relationship with the far-zone electric field of an antenna [2].

Directivity & antenna gain Directivity is characterized by the spatial power density in a specific direction, rather than the power in that direction. More specifically, the directivity in the direction (Θ,Φ) is defined as [57]:

$$D(\Theta, \Phi) = \frac{S(\mathbf{r})}{S_{ave}(\mathbf{r})}. \tag{2.25}$$

In this formula, $S(\mathbf{r})$ represents the power density at ($\mathbf{r}$,Θ,Φ), meaning at a distance $\mathbf{r}$ in the direction (Θ,Φ). $S_{ave}(\mathbf{r})$ stands for the average power density at that same distance, which is to say, $S(\mathbf{r})$ averaged across all potential directions at distance $\mathbf{r}$. Given that directivity is a ratio of power densities, it does not have units.

To summarize: Directivity is the proportion of power density in a given direction to the average power density across all directions at an equivalent distance from the antenna [57]. To put it precisely, the directivity remains constant at every distance $\mathbf{r}$. This is a crucial aspect: Directivity serves as a handy metric for characterizing an antenna because it remains unaffected by the distance from the antenna.

The gain G(Θ,Φ) of an antenna is essentially its directivity, adjusted to account for any loss within the antenna itself [57]. The gain of an antenna, in a specific direction, is defined as the ratio of the intensity in that direction to the radiation intensity that would result if the power received by the antenna were radiated uniformly in all directions. The radiation intensity corresponding to this isotropic radiation is equal to the power input P_{in} to the antenna divided by 4π [2].

$$G(\Theta, \Phi) = 4\pi \frac{U(\Theta, \Phi)}{P_{in}} = D(\Theta, \Phi) e_{c,d}. \tag{2.26}$$

The efficiency factor $e_{c,d}$ are the losses in the antenna related to conduction and dielectric losses [2].

Polarization Polarization is a characteristic of an electromagnetic wave that describes the time-varying direction and relative magnitude of the electric-field vector. It's the curve traced by the end point of the vector representing the instantaneous electric field, observed along the direction of propagation.

Polarization can be linear, circular, or elliptical. Linear polarization occurs when the electric field vector is always directed along a line. Elliptical polarization, the most common, occurs when the electric field traces an ellipse. Linear and circular polarizations are special cases of elliptical polarization, obtained when the ellipse becomes a straight line or a circle, respectively. The direction of the electric field's rotation can be clockwise (right-hand polarization) or counterclockwise (left-hand polarization).

The polarization characteristics of an antenna can be represented by its polarization pattern, which is the spatial distribution of the polarizations of a field vector radiated by the antenna over its radiation sphere. At each point on the radiation sphere, the polarization is usually resolved into a pair of orthogonal polarizations, the co-polarization and cross-polarization. Co-polarization represents the polarization the antenna is intended to radiate or receive, while cross-polarization represents the polarization orthogonal to a specified polarization, usually the co-polarization.

A time-harmonic wave is linearly polarized at a given point in space if the electric field vector at that point is always oriented along the same straight line at every instant of time. This is accomplished if the field vector possesses either only one component, or two orthogonal linear components that are in time phase or 180° out-of-phase.

A time-harmonic wave is circularly polarized at a given point in space if the electric field vector at that point traces a circle as a function of time. This requires the field vector to have two orthogonal linear components of the same magnitude, with a time-phase difference of odd multiples of 90°.

A time-harmonic wave is elliptically polarized if the end of the field vector (either electric or magnetic) traces an elliptical path in space as it changes over time. The direction of rotation can be clockwise (right-hand elliptically polarized) or counterclockwise (left-hand elliptically polarized).

Elliptically polarized waves are defined by their axial ratio, the ratio of the major to the minor axis. A wave is elliptically polarized if it is neither linearly nor circularly polarized. While linear and circular polarizations are special cases of elliptical polarization, elliptical polarization usually refers to cases other than linear or circular.

For a wave to be elliptically polarized, its field vector must have two orthogonal linear components. These components can be of the same or different magnitudes. If they have different magnitudes, the phase difference between them must not be 0° or multiples of 180° (otherwise, it would be linearly polarized). If they have the same magnitude, the phase difference must not be odd multiples of 90° (otherwise, it would be circularly polarized).

An example of a polarization trace is shown in Fig. 2.10.

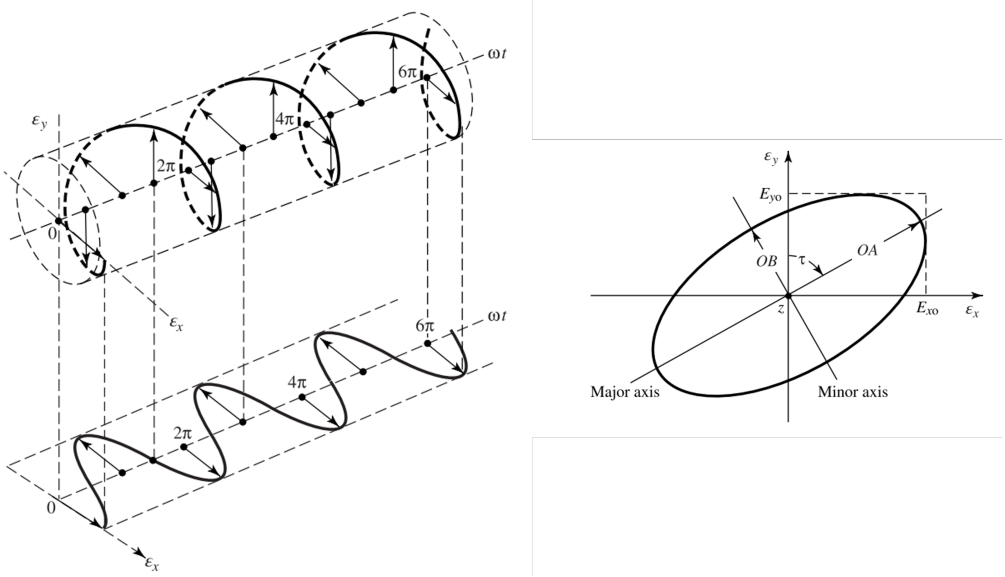

Figure 2.10: Polarization trace as a function over time traveling in z-direction. Circular polarization on the left and an polarization ellipse on the right [2]. (Source: C. A. Balanis, Antenna theory: analysis and design. Hoboken, New Jersey: Wiley, fourth edition. ed., 2016 - 2016)

2.2.2 Electromagnetic (EM) waves

The wave equation derived from the Maxwell equations for a charge and current free vacuum ($\rho = 0$, $\mathbf{j} = \mathbf{0}$) looks according to [59] as follows:

$$\nabla \times \mathbf{E} = -\frac{\partial \mathbf{B}}{\partial t}, \tag{2.27}$$

$$\nabla \times \mathbf{B} = \epsilon_0 \cdot \mu_0 \cdot \frac{\partial \mathbf{E}}{\partial t}. \tag{2.28}$$

Here, $\mathbf{E}$ is the electric field vector, $\mathbf{B}$ is the magnetic field vector, ϵ_0 is the dielectric constant of vacuum, μ_0 is the permeability of vacuum, and t is the time. After using the differential operator **rot** on both sides of Eq. 2.27 and substituting **rot B** from Eq. 2.28 in Eq. 2.27 the wave equation in the following form [59]:

$$\Delta \mathbf{E} = \epsilon_0 \mu_0 \frac{\partial^2 \mathbf{E}}{\partial t^2}. \tag{2.29}$$

This vector wave equation (Eq. 2.29) describes a wave with an altering electric field $\mathbf{E}(\mathbf{r}, t)$ propagating in vacuum at the speed of light $c = 1/\sqrt{\epsilon_0 \mu_0}$.

Assuming a periodic plane wave leads to the following expression for the wave equation in complex notation [59]:

$$\mathbf{E} = \mathbf{E_0} e^{i(\mathbf{k}\cdot\mathbf{r}-\omega t)}, \tag{2.30}$$

with the wave vector $|\mathbf{k}| = 2\pi/\lambda$, the position vector $\mathbf{r}$, the frequency ω, and time t.

2.2.2.1 Electromagnetic (EM) waves in plasma

The wave equation for EM waves in refractive media (or material in general) is shown in Eq. 2.31:

$$\mathbf{E} = \mathbf{E_0} e^{-\omega\kappa\frac{\Delta s}{c}} e^{-i(n_r-1)\frac{\Delta s}{c}} e^{i(\mathbf{k}\cdot\mathbf{r}-\omega t)}. \tag{2.31}$$

Two additional factors are present affecting the electric field along the propagation path. The factor $e^{-\omega\kappa\Delta s/c}$ with the imaginary part κ of the complex refractive n describes the attenuation due to absorption of the electric field along the propagation path Δs. Another common notation of the absorption uses the absorption coefficient α in m^{-1} according to Beer's law of absorption $\alpha = 4\pi\kappa/\lambda$. Using the absorption coefficient in the wave equation leads to the factor $e^{-\alpha\Delta s/2}$, which is identical to the factor described above. According to Eq. 5.1, there is no absorption in a collision-free plasma, since the refractive index is always real [59].

The second additional factor is $e^{-i(n_r-1)\Delta s/c}$, which describes the phase shift due to the refractive media. The phase shift $\Delta\phi = \omega(n_r - 1)\Delta s/c$ depends on the real part n_r of the complex refractive index n along the ray trajectory Δs. A refractive media is therefore causing a change in the EM wave's wavelength ($\lambda = \lambda_{vacuum}/n_r$) and its phase velocity ($v_{ph} = c/n_r$) [59].

2.2.2.2 Electromagnetic (EM) waves in magnetized plasma

The wave equation in magnetized plasma is essentially the same as in section 2.2.2.1. However, there are some differences. Firstly, the refractive index in a magnetized plasma can become complex even if no heavy particle collisions are considered in the plasma leading to absorption. Furthermore, an applied magnetic field affects the refractive index due to the dependency of the ray propagation direction on the magnetic field vector. Therefore, the real part of the complex refractive index can cause a different phase shift along the ray trajectory [59]. Additionally, the presence of a magnetic field causes the so-called Faraday rotation. The Faraday rotation along the wave path is calculated as follows [4]:

$$\psi_p = 2.36 \cdot 10^4 \frac{B \cdot N_T}{f^2}, \tag{2.32}$$

with B as the magnetic field, f as the electromagnetic wave frequency, and the total electron count (TEC) N_T. The equation for TEC is given below:

$$N_T = \int_S n_e(s) ds, \tag{2.33}$$

with the electron number density n_e along the propagation path s.

2.2.3 Signal characterization in BORAT

This section describes a novel model for characterizing signals, aiming to estimate received power at an antenna and analyze the impact of plasma and magnetized plasma. The model utilizes inputs such as ray tracing solutions, along with directivity patterns or complex electric field patterns of both transmitting and receiving antennas. Additionally, the model requires information on transmitting antenna power and antenna mismatch. Antenna gain can either be derived from radiation patterns or supplied as supplementary input data.

2.2.3.1 Friis transmission equation

The Friis Transmission Equation links the power received P_r by one antenna to the power transmitted P_t by another antenna over a distance R [2]:

$$P_r = e_{cdt} e_{cdr} (1 - |\Gamma_t|^2)(1 - |\Gamma_r|^2) \left(\frac{\lambda}{4\pi R} \right)^2 D_t(\Theta_t, \Phi_t) D_r(\Theta_r, \Phi_r) |\hat{\rho}_t \cdot \hat{\rho}_r|^2 P_t, \quad (2.34)$$

with

$$|\hat{\rho}_t \cdot \hat{\rho}_r|^2 = \cos(\psi_p)^2 \quad (2.35)$$

where D_t and D_r are the directivities of the transmitting and receiving antenna, respectively, e_{cdt} and e_{cdr} are the combined dielectric and conductive antenna efficiencies, $(1 - |\Gamma_t|^2)$ and $(1 - |\Gamma_r|^2)$ are the efficiencies due to reflection mismatch (losses due to the connection of the antenna to a transmission line), $|\hat{\rho}_t \cdot \hat{\rho}_r|^2$ is the power loss factor due to polarization mismatch of the incoming wave and the receiving antenna with the angle ψ_p between the polarization vectors (see Fig. 2.11). In general, the antenna polarization vector $\hat{\rho}$ describes the way the direction and magnitude of the field vectors at a given point and how they change in time. Usually, the E-field vector of the EM wave is used [2]. If the receiving and transmitting antenna are both linear polarized and in the same plane, only the rotation of the polarization vectors and their final orientation to each other are relevant. P_t and P_r are the transmitted and received power without antenna losses, the distance between the antennas or the wave path is R, and the wavelength of the electromagnetic wave is λ. Friis transmission equation is valid in the antenna far field. The angle ψ_p in

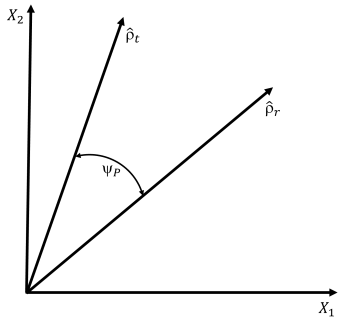

Figure 2.11: Schematic of the angle ψ_p between the polarization vectors of the incoming wave $\hat{\rho}_t$ and the receiving antenna $\hat{\rho}_r$ [2].

radians between the polarization vectors is obtained from the Faraday rotation along the wave path in case a magnetic field is present (applied magnetic field, Earth's magnetic field in experiments).

Additional losses $P_{loss,additional}$ [dB] in experiments, e.g cable losses, adapter losses, or windows, need to be considered, which leads to the following equation for the total received power $P_{r,total}$ [dB]:

$$P_{r,total} = P_r - P_{loss,additional}. \tag{2.36}$$

2.2.3.2 Electric field along the ray trajectory

The Friis transmission equation takes the losses related to distance, network mismatches, and polarization changes in the case of spherical radiation into account. Analyzing the electric field amplitude along the ray gives additional insights into the effect of a plasma on the EM wave and ensures the correct path loss calculation. Integrating theories of electromagnetic wave propagation and network introduces the concept of multilayered media network theory. Consequently, the mode of electromagnetic wave transmission in multilayered media can be transformed into a cascaded model, offering simplicity in concepts and consistency in results [60]. Therefore, we use the formulation of the received power after [58] in the following way:

$$P_r = S_t \cdot A_{Antenna,eff}, \tag{2.37}$$

with

$$S_t = \frac{|E_t|^2}{2\sqrt{\frac{\mu_0\mu_r}{\epsilon_0\epsilon_r}}}, \tag{2.38}$$

and

$$A_{Antenna,eff} = \frac{\lambda^2}{4\pi} G_r \tag{2.39}$$

where G_r is the antenna gain of the receiving antenna, E_t is the electric field of the radio signal reaching the receiving antenna, μ_0 and ϵ_0 are the permeability and permittivity of vacuum, respectively, and μ_r and ϵ_r the permeability and permittivity of the medium. S_t is the Poynting vector, λ is the wave length of the EM wave, and $A_{Antenna,eff}$ the effective antenna area.

The effective antenna area can be related to the electric field by replacing the gain with the square of the absolute value of the electric field in a certain direction at a distance r divided by the mean square electric field value in all directions at the same distance r multiplied by the efficiency of the receiving antenna leading to the following equation [57]:

$$A_{Antenna,eff} = \frac{\lambda^2}{4\pi} \frac{|E_i(r,\Theta,\Phi)|^2}{\frac{\sum_i^N |E_i(r,\Theta,\Phi)|^2}{N}} e_{cdr}. \tag{2.40}$$

The Poynting vector in a specific direction is also related to the electric field as following [61]:

$$S_t(R,\Theta,\Phi) = P_t \left(\frac{1}{4\pi R}\right)^2 G_t = P_t \left(\frac{1}{4\pi R}\right)^2 \frac{|E_i(r,\Theta,\Phi)|^2}{\frac{\sum_i^N |E_i(r,\Theta,\Phi)|^2}{N}} e_{cdt}. \tag{2.41}$$

Combining the equations 2.38, and 2.41 leads to the following expression for the calculation of the electric field at start position r_{start} ($r_{start} > 0$):

$$|E_t(r_{start},\Theta,\Phi)| = \sqrt{2\sqrt{\frac{\mu_0\mu_r}{\epsilon_0\epsilon_r}} P_t \left(\frac{1}{4\pi r_{start}}\right)^2 \frac{|E_i(r,\Theta,\Phi)|^2}{\frac{\sum_i^N |E_i(r,\Theta,\Phi)|^2}{N}} e_{cdt}}. \tag{2.42}$$

Figure 2.12 shows a schematic of the electric field calculation along a ray trajectory. Tx and Rx are the transmitting and receiving antennas, respectively. The different gray scales represent areas with different refractive indices. The black horizontal line at position E_7 represents a reflective surface.

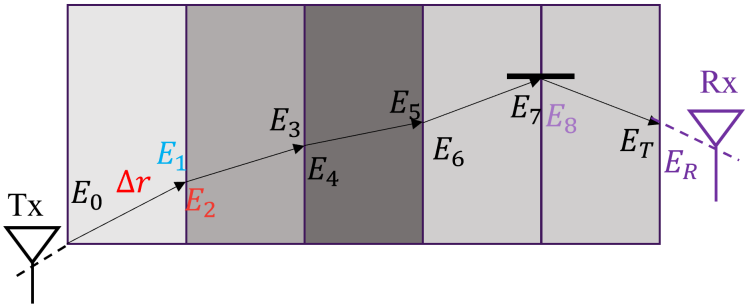

Figure 2.12: Schematic of the electric field calculation along a ray trajectory.

The amplitude of the electric field along the ray trajectory with a constant refractive index is calculated by applying the wave equation [59]:

$$E_1 = E_0 e^{i\omega t - nk_0} e^{-\omega(n_r-1)\frac{\Delta r}{c_0}} e^{-\omega\chi\frac{\Delta r}{c_0}} SF, \tag{2.43}$$

where $e^{-\omega\chi\frac{\Delta r}{c_0}}$ is the amplitude reduction due to heavy particle collisions and magnetic field effects with the imaginary part χ of the complex refractive index n, $e^{-\omega(n_r-1)\frac{\Delta r}{c_0}}$ is the phase shift due to the real part n_r of the refractive index, k_0 is the norm of the wave vector, ω is the angular radio frequency, t is the time, and c_0 the speed of light. Since energy must flow over a surface, the evolution of the electric field is related to a spreading factor describing the ray tube (ray area) A_i at a specific point i along the trajectory to a point before $(i-1)$:

$$SF = \sqrt{\frac{A_{i-1}}{A_i}} = \sqrt{\frac{r_{i-1}^2 \sin\frac{\Delta\Theta_{i-1}}{2}^2}{r_i^2 \sin\frac{\Delta\Theta_i}{2}^2}}, \tag{2.44}$$

where Θ_i is the angle between the two adjacent rays at point i, and Θ_{i-1} is the angle between the two adjacent rays at point $i-1$ [48].

At a point of refraction or reflection, the Fresnel coefficients need to be applied, which are different for the electric field vector parallel to the plane of incident and tangent to the plane of incident, and are described in the following:

$$\begin{aligned}
\frac{E_{tangent,reflection}}{E_{tangent,incident}} &= \frac{n_1\cos\alpha - \frac{\mu_1}{\mu 2}\sqrt{n_2^2 - n_1^2\sin\alpha^2}}{n_1\cos\alpha + \frac{\mu_1}{\mu 2}\sqrt{n_2^2 - n_1^2\sin\alpha^2}}, \\
\frac{E_{parallel,reflection}}{E_{parallel,incident}} &= \frac{\frac{\mu_1}{\mu 2}n_2^2\cos\alpha - n_1\sqrt{n_2^2 - n_1^2\sin\alpha^2}}{\frac{\mu_1}{\mu 2}n_2^2\cos\alpha + n_1\sqrt{n_2^2 - n_1^2\sin\alpha^2}}, \\
\frac{E_{parallel,refraction}}{E_{parallel,refraction}} &= \frac{2n_1 n_2\cos\alpha}{\frac{\mu_1}{\mu 2}n_2^2\cos\alpha + n_1\sqrt{n_2^2 - n_1^2\sin\alpha^2}}, \\
\frac{E_{tangent,refraction}}{E_{tangent,refraction}} &= \frac{2n_1\cos\alpha}{\frac{\mu_1}{\mu 2}n_2^2\cos\alpha + n_1\sqrt{n_2^2 - n_1^2\sin\alpha^2}},
\end{aligned} \tag{2.45}$$

with the magnetic permeabilities μ_1 and μ_2 before and after the reflection or refraction event, the refractive indices n_1 and n_2 before and after the reflection or refraction event and the angle α between the normal of the surface at the reflection/refraction point and the incident ray. The Fresnel coefficients account for the correct energy transport.

An additional phase shift might occur for the tangent and parallel electric field vector components depending on the ratio of the refractive index before and after the reflection. In case the refractive index is greater after the reflection both electric field components experience a phase shift of π if the reflection angle is greater than the Brewster angle. If the reflection angle is smaller, only the tangent electric field vector component experiences a phase shift of π. In case the refractive index is smaller after the reflection the phase shift of the tangent electric field vector component is zero if the reflection angle is smaller than the total reflection angle, otherwise, the following equation applies [59]:

$$\Delta\phi = 2 \cdot \tan\left(\frac{n_1^2}{n_2^2 \cos\alpha}\right)^{-1} \sqrt{\sin\alpha^2 - \left(\frac{n_2}{n_1}\right)^2}. \tag{2.46}$$

The parallel electric field vector component experiences a phase shift of π if the reflection angle is smaller than the Brewster angle, a phase shift of zero if the reflection angle is greater than the Brewster angle but smaller than the total reflection angle, or a phase shift according to the following equation of the reflection angle is greater than the total reflection angle:

$$\Delta\phi = 2 \cdot \tan\left(\frac{1}{\cos\alpha}\right)^{-1} \sqrt{\sin\alpha^2 - \left(\frac{n_2}{n_1}\right)^2}. \tag{2.47}$$

The refraction and reflection processes with their Fresnel coefficients are responsible for an altered polarization vector along the ray trajectory. The polarization vector experiences an additional rotation if a magnetic field is present. This additional rotation is obtained from the Faraday rotation along the incremental wave path [4]:

$$\psi_{p,i} = 2.36 \cdot 10^4 \frac{B \cdot N_{T,i}}{f^2}, \tag{2.48}$$

with B as the magnetic field, f as the electromagnetic wave frequency, and the total electron count (TEC) $N_{T,i}$. The equation for TEC is given below:

$$N_{T,i} = \int_s n_e(s) ds, \tag{2.49}$$

with the electron number density n_e along the incremental arc length s.

The Poynting vector of each ray reaching the receiving antenna is calculated using Equation 2.38 with the amplitude of the electric field $E_{t,end}$ at this position.

Possible interference between rays reaching the receiving antenna aperture is considered by converting the ray propagation path length differences into a phase shift and calculating the interference loss factor (IFL) by applying the following equation:

$$ILF = cos\left(\frac{\Delta L}{\lambda} \cdot 2\pi\right), \tag{2.50}$$

with ΔL as the ray propagation length difference between the receiving rays, and the wavelength λ.

Combining Equations 2.37, 2.38, 2.40, and 2.50 and adding the losses in the antenna network according to the Friis equation (Eq. 2.34) we get:

$$P_r = (1 - |\Gamma_t|^2) \cdot (1 - |\Gamma_r|^2) \cdot |\hat{\rho}_t \cdot \hat{\rho}_r|^2 \cdot S_{t,end} \cdot \frac{\lambda^2}{4\pi} \cdot D_r \cdot e_{cdr} \cdot ILF, \tag{2.51}$$

$$D_r = \frac{|E_i(r,\Theta,\Phi)|^2}{\frac{\sum_i^N |E_i(r,\Theta,\Phi)|^2}{N}},$$

$$S_{t,end} = \frac{|E_{t,end}|^2}{2\sqrt{\frac{\mu_0\mu_r}{\epsilon_0\epsilon_r}}},$$

$$ILF = cos\left(\frac{\Delta L}{\lambda} \cdot 2\pi\right).$$

Equation 2.2.3.2 is a different form of the Friis transmission equation and is applied to each ray reaching the receiving antenna and the total power P_{Rx} received is then calculated as the sum of the partial powers P_r normalized by the number of rays N:

$$P_{Rx} = \frac{1}{N} \sum_k^N P_{r,k}. \tag{2.52}$$

Possible additional losses $P_{loss,additional}$ [dB] in experiments, e.g cable losses, adapter losses, or windows, need to be considered as well, which leads to the similar equation for the total received power $P_{Rx,total}$ [dB] as in the section above:

$$P_{Rx,total} = P_{Rx} - P_{loss,additional}. \tag{2.53}$$

2.2.3.3 Scattering parameters

The antenna measurements are often performed using a Vector Network Analyzer (VNA), which measures the amplitude and phase of the wave quantities [62]. The magnitude of the complex S-parameters describes the amplitude ratio of the received to the transmitted sinusoidal signal generated by the VNA and the phase of the complex S-parameter corresponds to the phase difference between the incoming and outgoing waves at each port of the VNA. In the definition of power waves, the waves traveling away from a port of a n-port VNA are $\mathbf{a} = (a_1, a_2, ..., a_n)$ and the waves traveling towards a port are $\mathbf{b} = (b_1, b_2, ..., b_n)$ and are described as follows [63]:

$$\begin{aligned} a_i &= \sqrt{2P_{a_i}}, \text{and} \\ b_i &= \sqrt{2P_{b_i}}. \end{aligned} \tag{2.54}$$

Since we are only interested in the amount of power that is delivered to one or several receiving antennas from one transmitting antenna we ignore the self-reflection at the ports and are only concerned about the S-parameters S_{b_2,a_1} to S_{b_n,a_1}. Hence, these S-parameters describe the ratio of the received to the transmitted power.

$$\begin{aligned} S_{b_2,a_1} &= \sqrt{\frac{P_{b_2}}{P_{a_1}}}, \\ &..., \\ S_{b_n,a_1} &= \sqrt{\frac{P_{b_n}}{P_{a_1}}} \end{aligned} \tag{2.55}$$

Hereby, P_{a_1} stands for the transmitted power P_t, and P_{b_i} with $i = 2 - n$ stands for the received power P_r at each receiving antenna.

2.2.3.4 Convergence criterion

The typical condition for the convergence of ray tracing techniques necessitates resolutions at or below the scale of wavelengths of equivalent surface patches. This condition is often quantified by the number of rays per wavelength, typically around 10 rays per wavelength, or by the dimensions of ray tubes at the equivalent surface, commonly ranging from lambda/3 to lambda/6 in terms of edge lengths [64, 65]. To determine the theoretical quantity of rays needed for satisfactory convergence, we divide the total area of the Equivalent Sphere, denoted as A_{ES}, by the area of a ray tube, represented as A_T. This calculation yields the total number of ray tubes, denoted as N_T, as per Equation 2.56:

$$N_T = \frac{A_{ES}}{A_T}. \tag{2.56}$$

Consicering an actual antenna rather than a whole sphere requires the substitution of the Equivalent Sphere by the equivalent antenna aperture, which is the effective antenna area. Reducing the dimensions to 2D leads to a conversion from an area to a distance, which is the square root of the effective antenna area. The ray tube area is substituted by the square root of the ray tube, which is the distance aperture distance of the ray.

2.2.3.5 Signal characterization model in BORAT

The signal characterization in BORAT is implemented by the Ray Density Refinement method. The Ray Density Refinement method enables the analysis of the signal propagation and characterization in a wide radiation aperture and refining the signal characterization considering the convergence criteria at the relevant antenna positions. The signal characterization was implemented as an add-on to the ray tracing analysis. After the raytracing solution is produced using Snell's law solver or the Eikonal solver either of the two methods can be applied. The methodology of Ray Density Refinement is described as follows:
Ray Density Refinement method:

1. The rays closely reaching the antennas are identified and their original starting angle is obtained.

2. A second ray tracing analysis is started using the identified min. and max. initial radiation angles of each receiving antenna.

3. The rays hitting the receiving antenna aperture are identified and their receiving power is calculated according to Equations (2.37-2.52) when analyzing the electric field along the trajectory, or Equations (2.34-**??**) when applying the Friis equation.

4. The power of each ray is added, and the losses of the equipment are subtracted using Eq. (2.53/2.36).

5. The S-parameters are calculated according to Eq. (6.5).

3 BORAT - BlackOut RAy Tracer

This chapter contains the Development stages of BORAT starting from the original version developed by Jan Thoemel to the current version including the possibility to analyze magnetized and non-magnetized plasma including signal characterization. The current BORAT version with signal characterization operates in 2D. The rationale and the workflow of BORAT are explained as well.

Contents

3.1 BORAT development stages

BORAT 1.0, developed by Jan Thoemel, uses the Snell's law solver to calculate the trajectory of a ray's propagation within the refractive index field in the numerical flow domain, based on geometrical optics.

Vincent F. Giangaspero (KU Leuven) developed BORAT 2.0, which introduces the Eikonal Solver. This solver, based on wave optics principles, provides faster computation than the Snell's law solver while maintaining similar accuracy. The need for computational efficiency led to the development of BORAT 3.0, which expands the ray tracing algorithm to three dimensions, with the third dimension introduced by Vincent F. Giangaspero.

BORAT 4.0 is designed to analyze the effects of a magnetic field and uses the Snell's law solver to determine the ray's propagation path in magnetized plasma.

BORAT 5.1 introduces signal characterization for non-magnetized plasma to study the impact of a plasma environment on signal characteristics.

Finally, BORAT 5.2 integrates both signal characterization and the magnetic Eikonal Solver to investigate the effects of magnetized plasma on radio signals.

An overview of the BORAT versions is depicted in Figure (3.1).

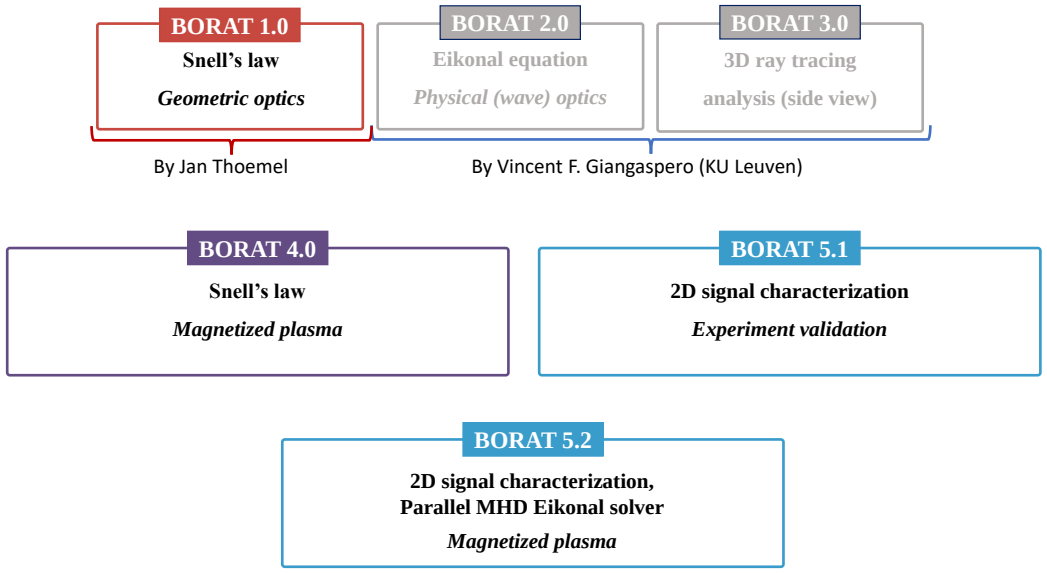

Figure 3.1: BORAT development stages.

3.2 BORAT rationale

The rationale of BORAT 5.2 is shown in Fig. (5.1). Performing a numerical analysis of the radio communication blackout with BORAT necessitates a Computational Fluid Dynamics (CFD) simulation as an input. The separation of the ray tracing analysis from the fluid computation is justified due to the difference in time scales between multi-species hypersonic flows (milliseconds) and radio waves (nanoseconds) [66]. This allows for the integration of any CFD software by incorporating the necessary I/O capabilities into BORAT. Essential fluid properties within the flow domain, such as gas composition, temperature models, and magnetic field data,

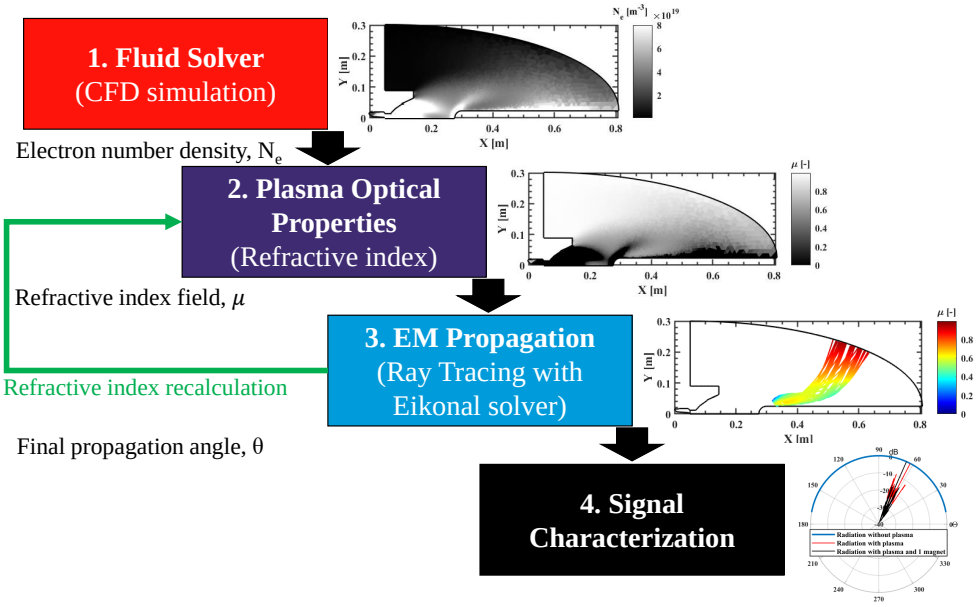

Figure 3.2: Rationale for BORAT with Signal Characterization for Magnetized Plasma.

are gathered. Subsequently, the electron number densities in the flow domain are computed from these fluid properties.

The next step involves calculating the plasma optical properties using the Appleton-Hartree equation (refer to section 5.1.2). Depending on the antenna aperture, antenna position, the refractive index field, and the applied magnetic field, either the Snell's law solver or the Eikonal solver is employed to forecast the ray propagation. If a magnetic field is present, the refractive index field must be recalculated after each ray step size because the refractive index in magnetized plasma depends on the angle between the ray vector and the B-field vector.

The ray tracing solution, along with the antenna characteristics information, is needed to characterize the radio signal. Parameters such as the radiation pattern, energy, and intensity along the ray trajectory are computed. A comprehensive workflow is depicted in Fig. (6.1).

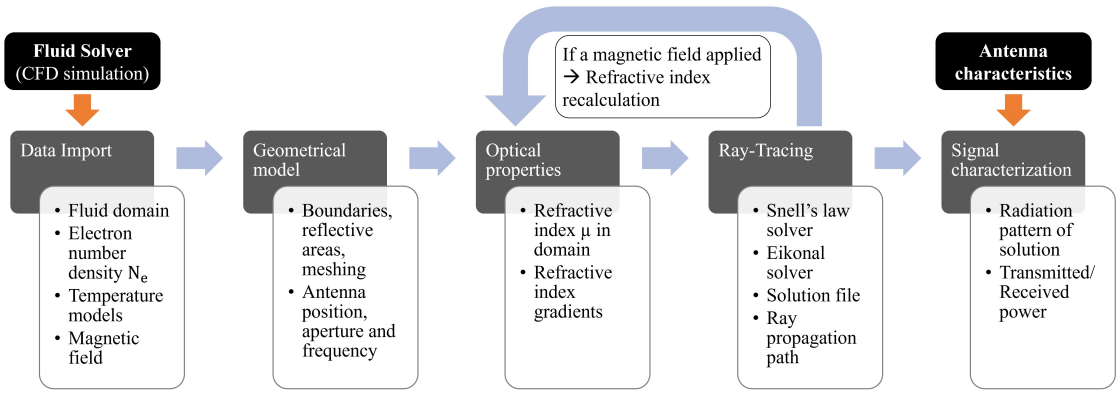

Figure 3.3: Workflow of BORAT with Signal Characterization for Magnetized Plasma.

4 Magnetized plasma: Two dimensional study

BORAT 4.0, based on a Snell's law solver, is introduced to analyze the signal behavior during re-entry using geometrical optics for non-magnetized and magnetized plasma. The ray tracing analysis is performed on Knapp's case fluid simulations provided by the University of Stuttgart. The effect of an applied magnetic field on ray tracing is discussed and visualized using radiation patterns. The results suggest that a sufficiently strong magnetic field is promising to mitigate radio communication blackout.

This chapter is based on the work published in the following research paper:

- J. S. Laur, V. F. Giangaspero, V. Sharma, A. Lani, N. Donaldson, M. K. Kim, J. Giacomelli, G. Herdrich, A. Hein, and J. Thoemel, "Radio communication blackout mitigation: Analyzing magnetic field effects via ray-tracing analysis," AIAA Journal, pp. 1–12, Apr. 2024.

Contents

4.1 Overview

The work presented in this article includes the capability of two-dimensional ray tracing for magnetized plasma. This enables the prediction of the propagation of electromagnetic waves in re-entry plasma using a magnetic field to mitigate radio communication blackout. Within this work the signal path in the absence and presence of a magnetic field for the Knapp's test case [67] using a novel ray tracing algorithm is analyzed. Knapp's test case is an experiment involving an argon plasma flow impacting on a MHD-probe equipped with a variable number of magnets in order to investigate the effects of the magnetic fields [68, 3]. It was numerically rebuilt by the computational fluid dynamics (CFD) codes employed by the MEESST consortium [67]. In Knapp's test cases, a probe was equipped with different magnet systems designed to alter the shape of the plasma sheath surrounding it. The experiments investigated the interaction between an MHD probe and an argon plasma flow and assessed the effects of a magnetic field with different intensities on the shock structure and heat flux. The experiments were carried out at IRS in the plasma wind tunnel PWK1 and the plasma source was the magnetoplasmadynamic (MPD) plasma generator RD5. The head of the probe is semi-spherical and has a 50-mm diameter. One to six neodymium permanent magnets with a nickel coating are positioned 5 mm behind the probe head surface at the centerline. The maximum measured magnetic flux in front of the probe was 0.265 T when using six magnets.

4.1.1 BORAT 4.0

BORAT 4.0 predicts the ray propagation of electromagnetic waves emerged from an antenna within a magnetized plasma. Analyzing the wave propagation using BORAT 4.0 requires the following steps illustrated in Fig. 4.1.

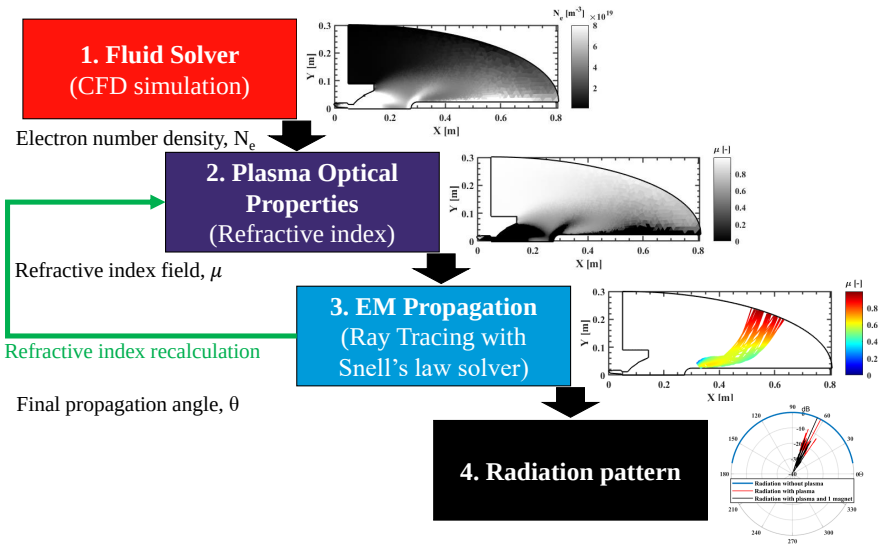

Figure 4.1: Illustration of the rationale for BORAT 4.0.

First, a CFD simulation of a re-entry trajectory point - in this work the simulation results of Knapp's case [67] - is required as input for the code. The CFD solution provides the coordinates and fluid properties in the cells or on the nodes. All the relevant information in the flow domain to calculate the electron number densities

are gathered (e.g densities, number of species, temperatures, etc.). The electron number densities can be, in case they are not provided directly, obtained from the partial densities or the molar fractions of the species. In case a magnetic field is applied, the information of the magnetic field properties in the domain are required as well. The vehicle or probe geometry and the domain boundaries are identified and rebuilt from the CFD simulation to account for reflections of the radio signal on the vehicle and to stop the ray calculation at the domain boundary, respectively. Afterward, the optical properties, i.e., the refractive indexes, are calculated in the flow domain, which is required to determine the refraction or reflection of the ray by applying Snell's law. BORAT is in general also capable of calculating the refractive index considering heavy particle collisions. In this case, BORAT is coupled with Mutation++ developed by VKI. Mutation++ is an open-source library to provide thermodynamic, transport, chemistry, and energy transfer properties associated with subsonic to hypersonic flows, which is used to calculate the correct collision frequency [69]. Finally, the ray paths are calculated and plotted in the domain, and the radiation patterns are plotted.

4.1.2 Optical properties in BORAT 4.0 - the refractive index

The governing equation to calculate the refractive index of a non-magnetized, collision-less plasma can be found in Section 2.1.3.4, Eq. 5.1 and is repeated hereafter:

$$n = \mu = \sqrt{1 - X} = \sqrt{1 - \left(\frac{f_p}{f}\right)^2}, \tag{4.1}$$

with

$$f_p = \sqrt{kN_e}, \text{ and} \tag{4.2}$$

$$k = e^2 / \left(4\pi^2 \epsilon_0 m_e\right). \tag{4.3}$$

Since a magnetized plasma is considered as well, the equation to calculate the refractive index of a magnetized, collision-less plasma is, for convenience, repeated here (see Eq. **??** in Section 2.1.3.2):

$$n^2 = (\mu - \chi i)^2 = 1 - \frac{X}{1 - \frac{Y^2 sin^2(\Theta)}{2(1-X)} \pm \sqrt{\frac{Y^4 sin^4(\Theta)}{4(1-X)^2} + Y^2 cos^2(\Theta)}}., \tag{4.4}$$

with

$$\begin{aligned} X &= e^2 N_e / \left(\epsilon_0 m_e \omega^2\right), \\ Y &= eB / (m\omega) \\ \omega &= 2\pi f. \end{aligned} \tag{4.5}$$

4.1.3 BORAT 4.0 scheme and solver for magnetized plasma: Snell's law solver

In BORAT 4.0 the Snell's law solver was extended to account for MHD effects. A detailed description of the Snell's law solver can be found in Section 2.1.2.1.

The scheme of BORAT for magnetized plasma is shown in Fig. 4.2. As mentioned earlier, a fluid simulation is required as input to get the relevant parameters in the

fluid domain. Then, the initial start conditions are set (number of rays, aperture angle, position of rays). Next, the refractive index at the start condition for the first ray is calculated and marched the first ray step according the step size. The position and angle at this step are saved. If no boundary is reached the refractive index at the second ray position is recalculated and again Snell's law is applied to identify the next ray step. This procedure continues until the ray reaches the boundary and the next ray is calculated. After all ray paths have been calculated the rays will be drawn and BORAT exits. In case of a non-magnetized plasma, the recalculation of the refractive index after each step is not required, since the refractive index is independent from the ray propagation.

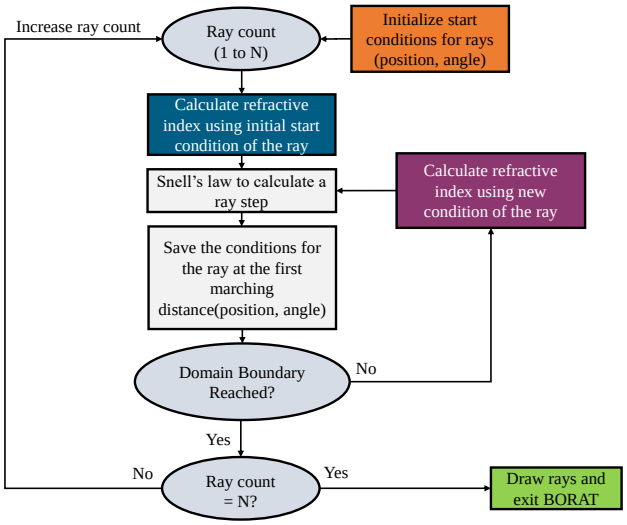

Figure 4.2: BORAT scheme for magnetized plasma.

4.1.4 Radiation pattern in BORAT 4.0

Radiation patterns are common to show the aperture angle and signal strength of antennas. The radiation patterns provide a better visualization of the ray tracing solutions and show the aperture angle of the rays leaving the flow domain. In this BORAT version, the angular power density $U_i(s)$ emitted by the antenna is calculated using the following eq. [48]:

$$U_i(s) = \frac{P_{antenna}}{2\pi} g \frac{\Delta\theta(0)}{\Delta\theta_i(s)}, \tag{4.6}$$

where $P_{antenna}$ is the emitted power by the antenna, g is the antenna gain, $\Delta\theta(0)$ the angle between two adjacent rays (n and n+1) at initial conditions and $\Delta\theta_i(s)$ the angle at position s between the ray n and n+1. Only rays, which are leaving the domain are considered in the radiation pattern. Rays, which get fully attenuated by the plasma are not counted.

4.2 Results and Discussion

A ray tracing analysis using BORAT for Knapp's case, provided by the MEESST project partner at IRS, University of Stuttgart, was performed to investigate the influence of the magnetic field on the ray propagation. The in-house code SAMSA (Self- and Applied Field MPD-thrusters Algorithm) of IRS is used to compute the flow field with a mesh composed of 26987 triangular cells. A second–order Weighted Essentially Non–Oscillatory (WENO) scheme is used and an explicit time integration is done to achieve a steady-state solution. Ohm's laws for plasmas and the Maxwell Equations in the vector potential formulation are used to calculate the magnetic field distribution. The Argon flow is simulated using a three-species model (free electrons, neutral Argon particles, and first-level ionized Argon ions). Thermal non-equilibrium is assumed. In the forward reaction only the electron impact ionization is considered and the neutralization through triple collision recombination in the backward reaction. More information can be found in the literature [67, 70]. The following conditions were used to perform the test campaign:

- radio signal frequency of 71 GHz (V Band);
- 50 rays with an initial aperture angle of 160°;
- initial start position of the rays at $X = 0.334$ m and $Y = 0.0252$ m;
- Snell's law solver with a step size of 0.002 m;
- neglecting collisions in plasma;
- only right-hand polarized waves for magnetized plasma.

Figure 4.3 shows the flow domain of Knapp's case. The outer boundary on the left side of the probe in blue is the geometry of the vacuum chamber with the plasma generator exit between $X = 0$ m and $X = 0.85$ m, and $Y < 0.4$ m. The antenna position at the probe with its radiation angle is marked as well.

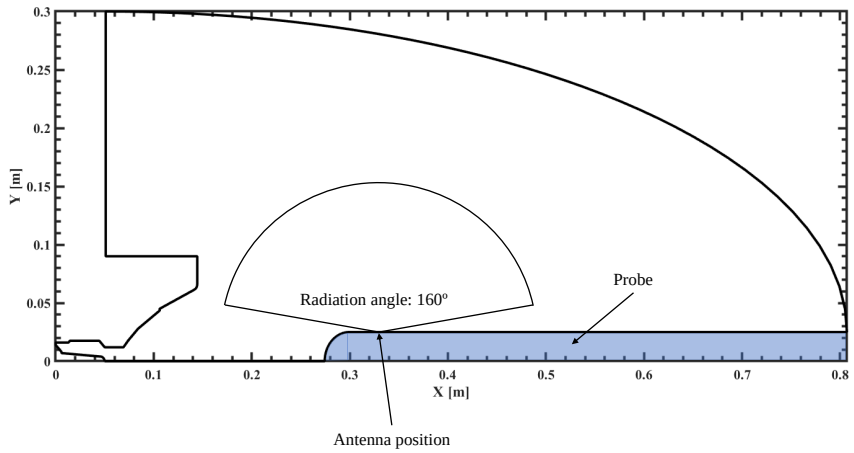

Figure 4.3: The flow domain of Knapp's case extracted from the CFD solution provided by IRS, University of Stuttgart.

A schematic of the design of the probe is shown in Fig. 4.4. This water cooled copper probe with a probe head radius of 25 mm can contain up to 6 stacked magnets in its core.

For this test campaign four different scenarios were analyzed:

- No magnet within the probe;
- 1 magnet within the probe ;
- 6 magnets within the probe;
- 6 magnets within the probe with artificially increased magnetic field strength by factor 10;

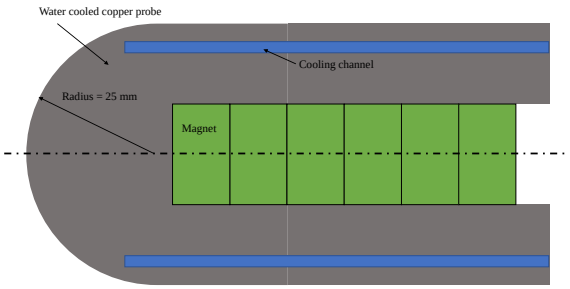

Figure 4.4: Schematic of the probe of Knapp's case, which can contain up to 6 magnets.[3]

Based on the conditions of Knapp's test cases, an antenna position was found where the electron density is low enough to allow wave propagation and where the magnetic strength is high enough to influence the ray propagation. The antenna position to start the rays was chosen to be in the proximity of the magnetic field and as close as possible to the probe surface. Decreasing the radio frequency leads to a greater radial distance of the start conditions because of a decrease of the refractive index (all rays would be instantly blocked). Further increasing the radio frequency would lead to an increased refractive index and therefore non-refracted rays. The magnetic field strength and the antenna position for the two cases with 1 magnet, and 6 magnets are shown in Fig. 4.5 (a), and (b), respectively. The magnetic fields are peaking at the tip of the probe. The experimental measured B-field values at the tip of the probe are, according to Knapp, 0.2 T for the case with 1 magnet (a) and 0.265 T for the case with 6 magnets (b), respectively. These weak magnetic fields have a small range. The magnet field strength at the starting position of the rays is below 0.05 T for the 6 magnet case and around 0.01 T for the 1 magnet case, respectively. Such weak magnetic fields have a limited influence on the ray tracing solution. The step size independent study for a single ray of the non-magnetized plasma case is shown in Fig. 4.6. A step size of 0.002 m was chosen with respect to accuracy and computational resources.

4.2.1 Fluid simulation of Knapp's case

According to the described rationale in section 3.2, first, the electron number densities in the flow domain are required. The electron number densities in the flow domain for (a) a non-MHD case, an MHD case with (b) 1 magnet, and (c) 6 magnets are shown in Fig. 4.7. For a better visualization the max. electron number density in the contour plot is limited to the critical electron number density ($6.26 \cdot 10^{19}$ m^{-3}). The overall maximum electron number density in the flow domain is $1.7 \cdot 10^{22}$ m^{-3}. The electron number densities at the tip of the probe (stagnation point) are high and

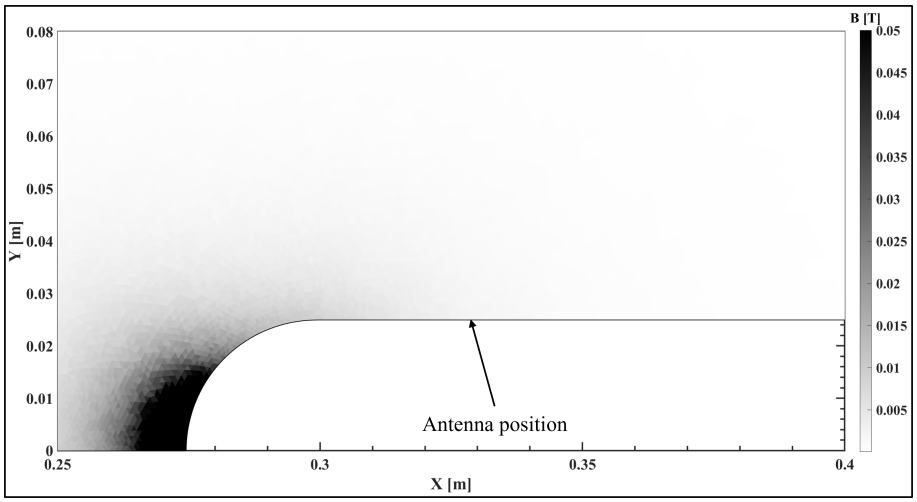

(a)

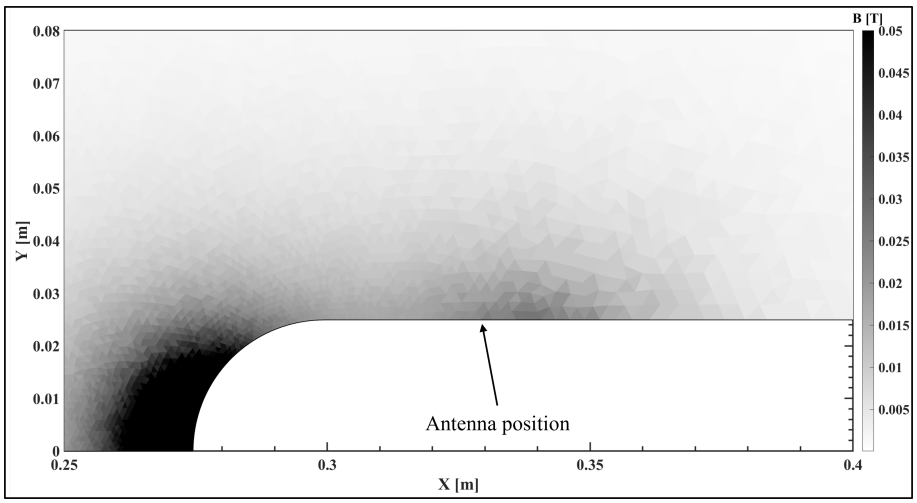

(b)

Figure 4.5: Contour plot of magnetic field strength for the cases with 1 magnet, and 6 magnets as zoom into the important areas.

decrease along the shoulder. Further downstream on the boundary of the probe the electron number density is increasing again and reaches its max. at around $X = 0.6$ m. The increased shock standoff distance is also very visible for the case with 6 magnets within the probe.

4.2.2 Initial refractive index in the flow domain

The initial refractive index in the flow is shown as a contour plot in Fig. 4.8, which directly corresponds to the electron number density. This will change for magnetized plasma as described earlier. The refractive index at the tip of the probe is zero (black), which leads to total reflection. Around the shoulders, the refractive index stays zero and increases further downstream and for greater radii. As shown in Fig. 4.7, the refractive index is decreasing again around the probe surface further downstream and peaks at around $X = 0.6$ m. Between Fig. 4.8 (a) and (b) is no significant difference is visible. Again, in Fig. 4.8 (c) the increased standoff distance is clearly visible.

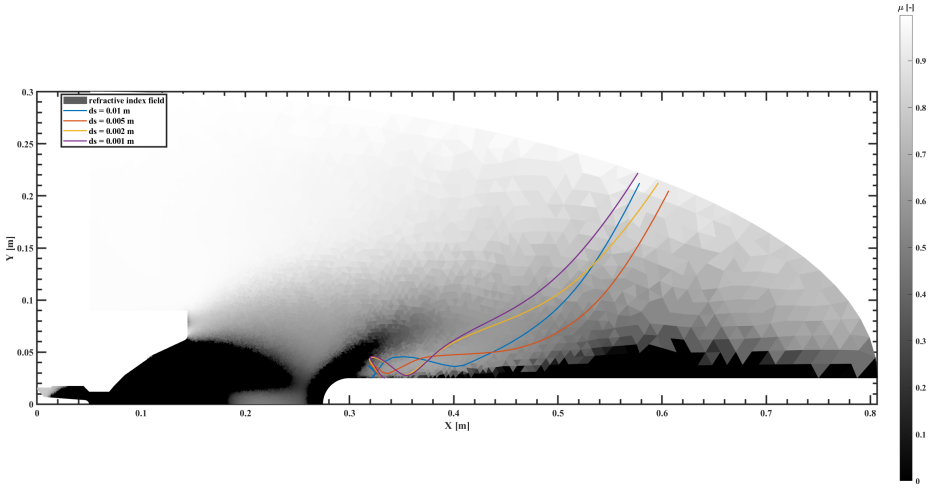

Figure 4.6: Step size independent study of a single ray for the non-magnetized plasma case with the refractive index in the flow domain as a contour plot.

4.2.3 Ray tracing analysis of Knapp's case

The results of the ray tracing analysis for (a) the non-MHD, (b) 1 magnet and (c) 6 magnets case are shown in Fig. 4.9. A ray density analysis was performed to identify a sufficient number of rays, leading to 2 rays per degree, which makes a total of 320 rays in these ray tracing solutions. As mentioned earlier, the refractive index is locally changing while the wave is propagating through the magnetized plasma because the refractive index depends on the angle between the wave vector and the B-field vector as well as the B-field strength. This is the reason why for magnetized plasma cases a different display style was chosen for the refractive index. Here, the refractive index is displayed as ray color. Purple stands for a low refractive index and dark red for a high refractive index.

The chosen simulation conditions lead to brownout conditions where rays are able to escape the plasma. This is of interest to further analyze the influence of the magnetic field. All of the rays in Fig. 4.9 (a) are heavily refracted towards the starting point and also reflected at the shoulder region. When the electron number density increases further downstream, the rays are refracted and form a very small aperture angle when they leave the flow domain. Applying a magnetic field using 1 magnet leads to a very similar case, as shown in Fig. 4.9 (b). The rays seem to be less refracted along their path, especially the heavy bending region around the shoulder looks smaller. However, the weak influence of the magnetic field of the 1 magnet case together with the close relation to the non-magnetized case show that the model is correct. The aperture angle at the flow domain boundary is about the same size as the non-MHD case with one ray further apart from the others. If 6 magnets are implemented in the probe the ray tracing solution changes significantly. The rays are much weaker bent and the aperture angle increased, as shown in Fig. 4.9 (c).

In order to obtain an outlook to the impact of higher magnetic field strength, an artificially increased magnetic field strength is assumed in the following ray tracing analysis. According to literature magnetic field strength of 1 T or higher promises to

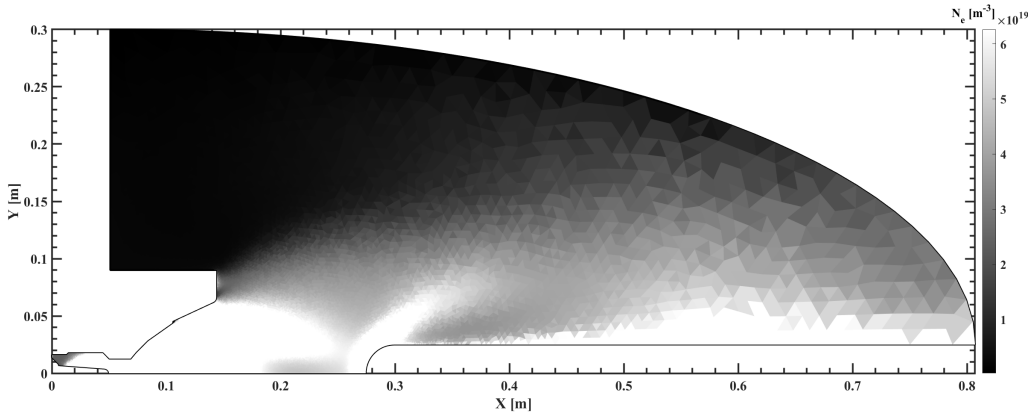

(a)

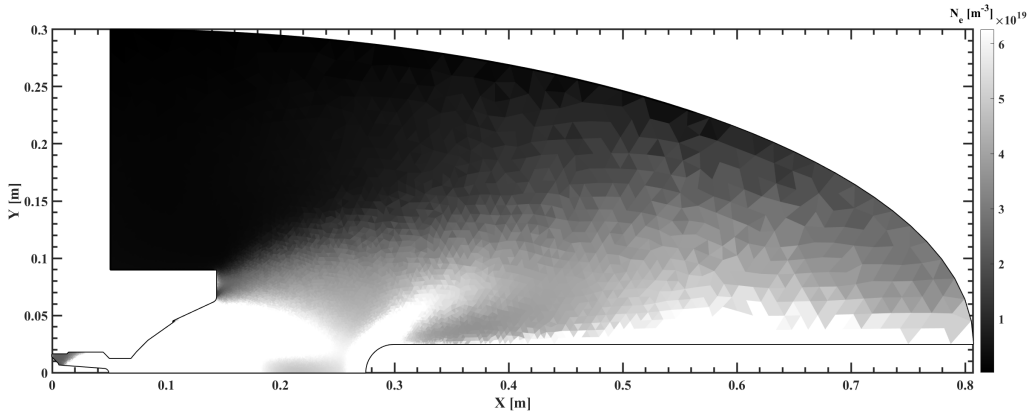

(b)

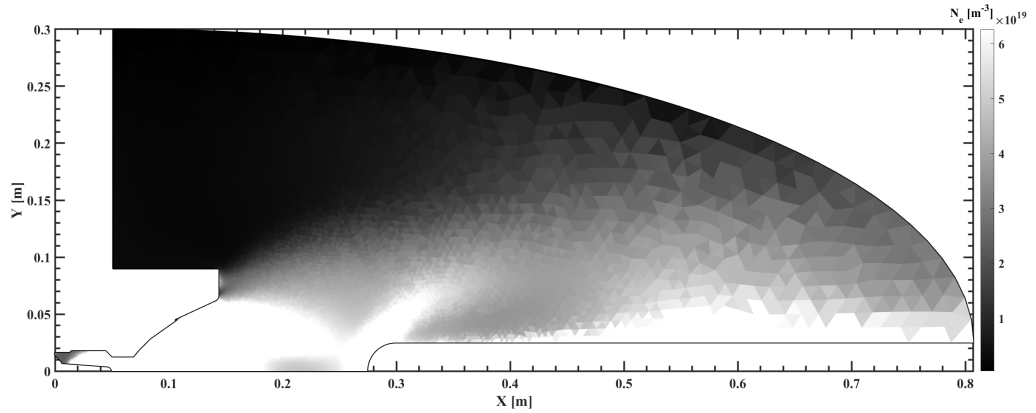

(c)

Figure 4.7: Electron number densities in the flow domain for (a) a non-MHD case, an MHD case with (b) 1 magnet, and (c) 6 magnets. The contour plot is limited to the critical electron number density at a frequency of 71 GHz.

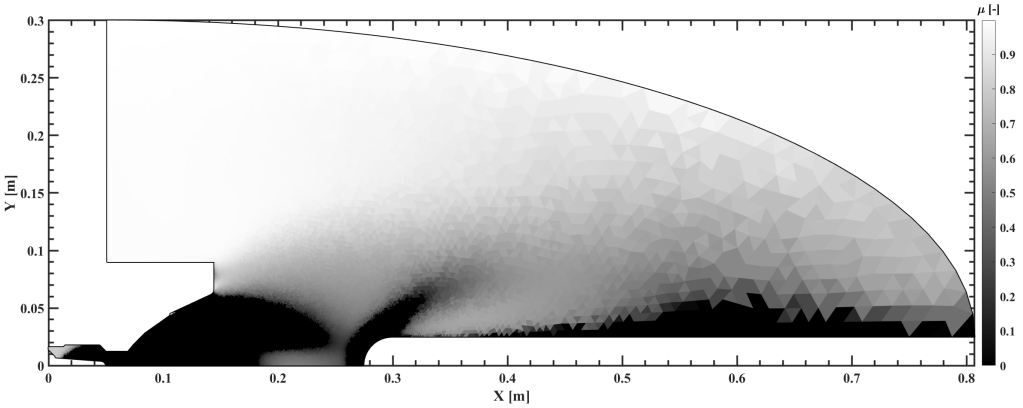

(a)

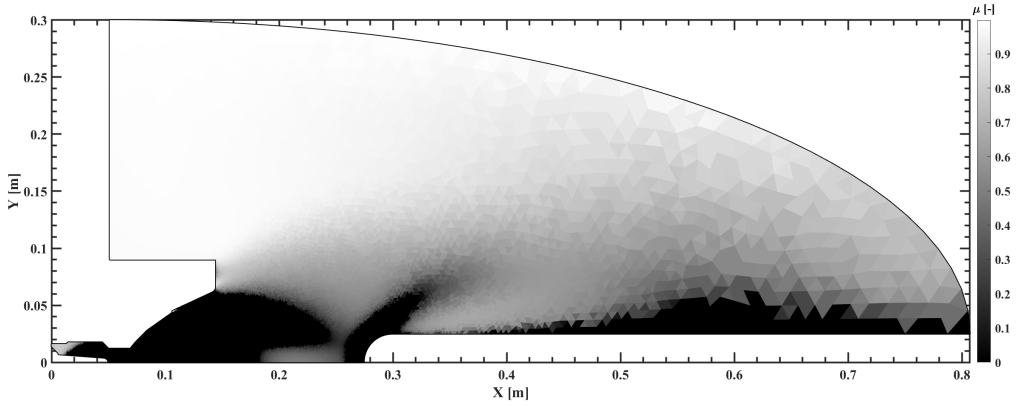

(b)

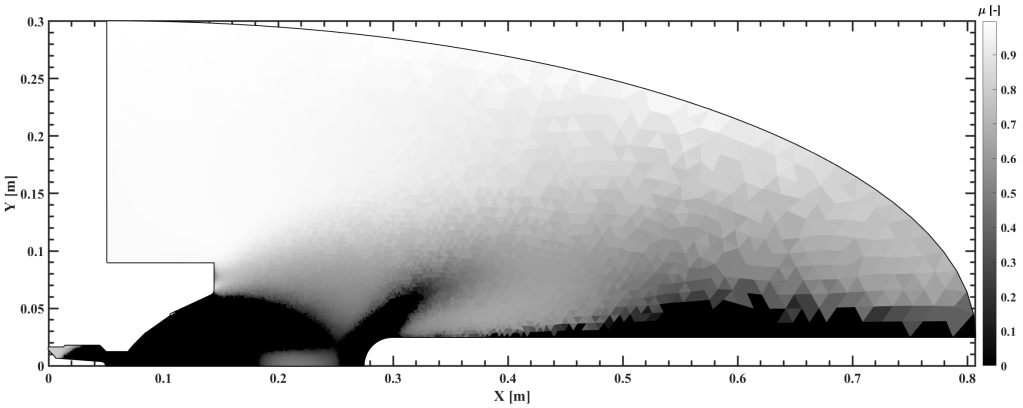

(c)

Figure 4.8: Refractive indexes in flow domain for (a) a non-MHD case, an MHD case with (b) 1 magnet and (c) 6 magnets before launching rays.

avoid radio communication blackout [18]. The design of the superconducting magnet of the MEESST project aims to provide a magnetic field strength of up to 2 T. The magnetic field was artificially increased by a factor of 10 to have a greater impact on the raytracing solution. The results of this artificially increasing is shown in Fig. 4.10 for the 6 magnets case. The authors want to repeat, that the magnetic field is artificially increased by a factor of 10 assuming the electron density and electron distribution are not changing, which is not true. Hence, no valid comparison between neglected collisions and collisions can be made at this stage. The authors want to give a possible outlook on how the raytracing solution could change when applying a stronger magnetic field.

Comparing Knapp's 6 magnets case with an artificially increased magnetic field strength with its own standard case, a tremendously increased aperture angle and a very even ray distribution over the aperture angle can be detected (see Fig. 4.10). The aperture angle seems to be double as wide as for the non-MHD case (Fig. 4.9 (a)). The refractive indexes, which are the rays facing during its propagation through the plasma, look lower because of the magnetic field. This underlines the behavior that was analyzed for the standard MHD cases without increased magnetic field. The behavior of the artificially increased magnetic field cases shows the expected trend. This leads to the conclusion that significant magnetic field strength is required, which affects at first the fluid flow and second the ray propagation. It also shows the possibilities of the magnetic windowing method. The improvements in high-temperature superconducting materials, which enabled the MEESST project, can create such a sufficiently strong magnetic field in an economic way.

4.2.4 Radiation pattern of Knapp's case simulations

An ideal antenna was assumed with an uniform radiation over the aperture angle and an antenna gain of 1 [71]. The calculated angular power density as described in eq. 4.6 is converted into dB. Without any interference and within a const. refractive index the resulting radiation pattern is shown in Fig. 4.11 as uniform blue line over the initial aperture angle of 160°.

In Table 4.1 the min. and max. aperture angles are listed for the initial, non-MHD and all magnetic cases. It clearly shows a decrease of the min. radiation angle if a plasma is present and the magnetic field strength increases. The max. radiation angle is decreasing for the 1 magnet case compared to the non-MHD case but increasing when 6 magnets are used. Applying a magnetic field changes in these cases both, the min. and the max. radiation angle.

Table 4.1: Comparison of min. and max. radiation angle of all cases and at initial conditions (absence of plasma).

Case	Max. radiation angle [°]	Min. radiation angle [°]
Initial	170	10
Non-MHD	76.4	54.4
1 magnet	74.9	52.8
6 magnets	76.4	51.5
6 magnets, 10B	91.0	50.9

In Table 4.2 the aperture angles for the non-MHD, magnetized plasma cases are

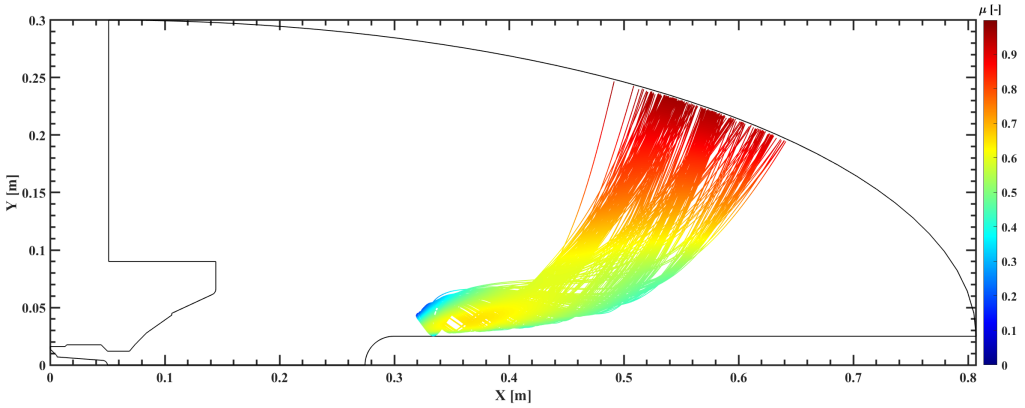

(a)

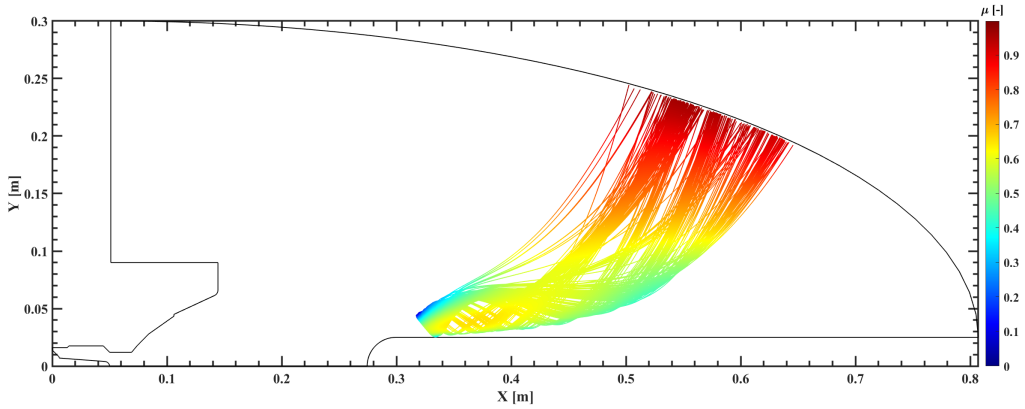

(b)

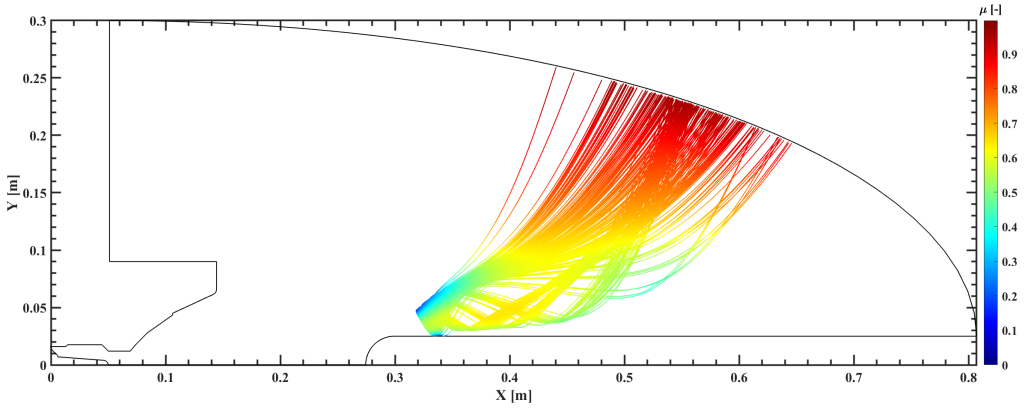

(c)

Figure 4.9: Ray tracing solution for (a) non-MHD case, MHD case with (b) 1 magnet, and (c) 6 magnets with the refractive index /*mu* as color-bar.

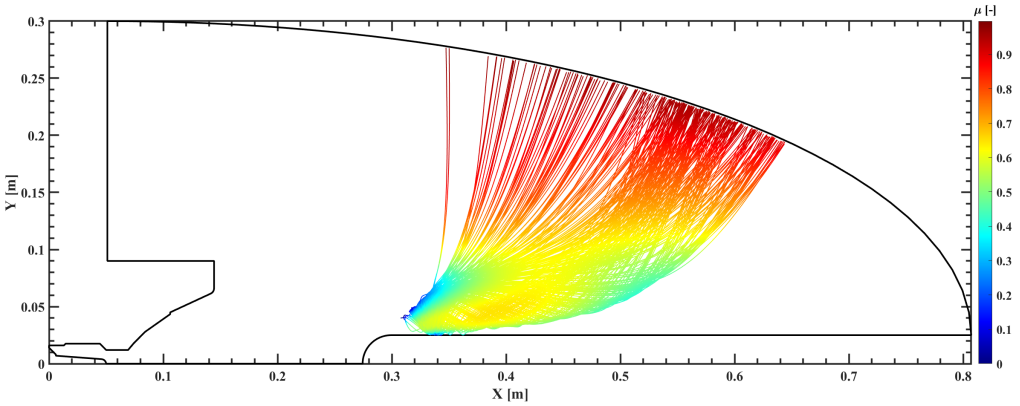

Figure 4.10: Ray tracing solution for 6 magnets and artificially increased B-field by a factor of 10 with the refractive index /*mu* as color-bar.

compared. The non-MHD case has an aperture angle of 22°. The aperture angle of the 1 magnet case is increased by 0.45% compared to the non-MHD case and has an aperture angle of 22.1°. Comparing the 6 magnets case to the non-MHD case, the aperture angle is increased by 13.1% and spans 24.9°. According to the radiation patterns the signal strength gets lower for larger aperture angles, which means the same amount of power is radiated on a bigger area. It is also visible that areas with higher ray density lead to a stronger signal. Interference and other signal properties are not covered in this work and can have a significant influence on the signal strength and quality.

Table 4.2: Comparison of the radiation aperture angle and the aperture angle increase compared to non-MHD case.

Case	Aperture angle [°]	Aperture angle increase [%]
Non-MHD	22.0	-
1 magnet	22.1	0.45
6 magnets	24.9	13.1
6 magnets, 10B	34.5	82.3

Analyzing the radiation patterns for the non-MHD and 1 magnet case in Fig. 4.11 (a) shows a very similar aperture angle. In Table 4.1 can be seen that the max. radiation angle decreased by 1.5° and the min. radiation angle decreased by 1.6° for the 1 magnet case compared to the non-MHD case. This leads to an aperture angle increase of 0.45 %. The angular power density is peaking to 0 dB at one position similar to the non-MHD case and is overall in the same range for both cases. The radiation pattern for the artificially increased magnetic field case with 6 magnets in Fig. 4.11 (c) shows that both, the max. aperture angle and the min. angle changed compared to the standard magnetic cases. The max. angle increased by 14.6° and the min. angle decreased by 0.6° compared to the standard 6 magnet case, which is an increase of 38.6% comparing these two cases. The aperture angle of the artificially increased 6 magnets case increased by 82.3% according to Table 4.2 compared to the non-MHD case. The 6 magnets cases are peaking up to 0 dB at two positions but have overall a reduced angular power density compared to the non-MHD and 1

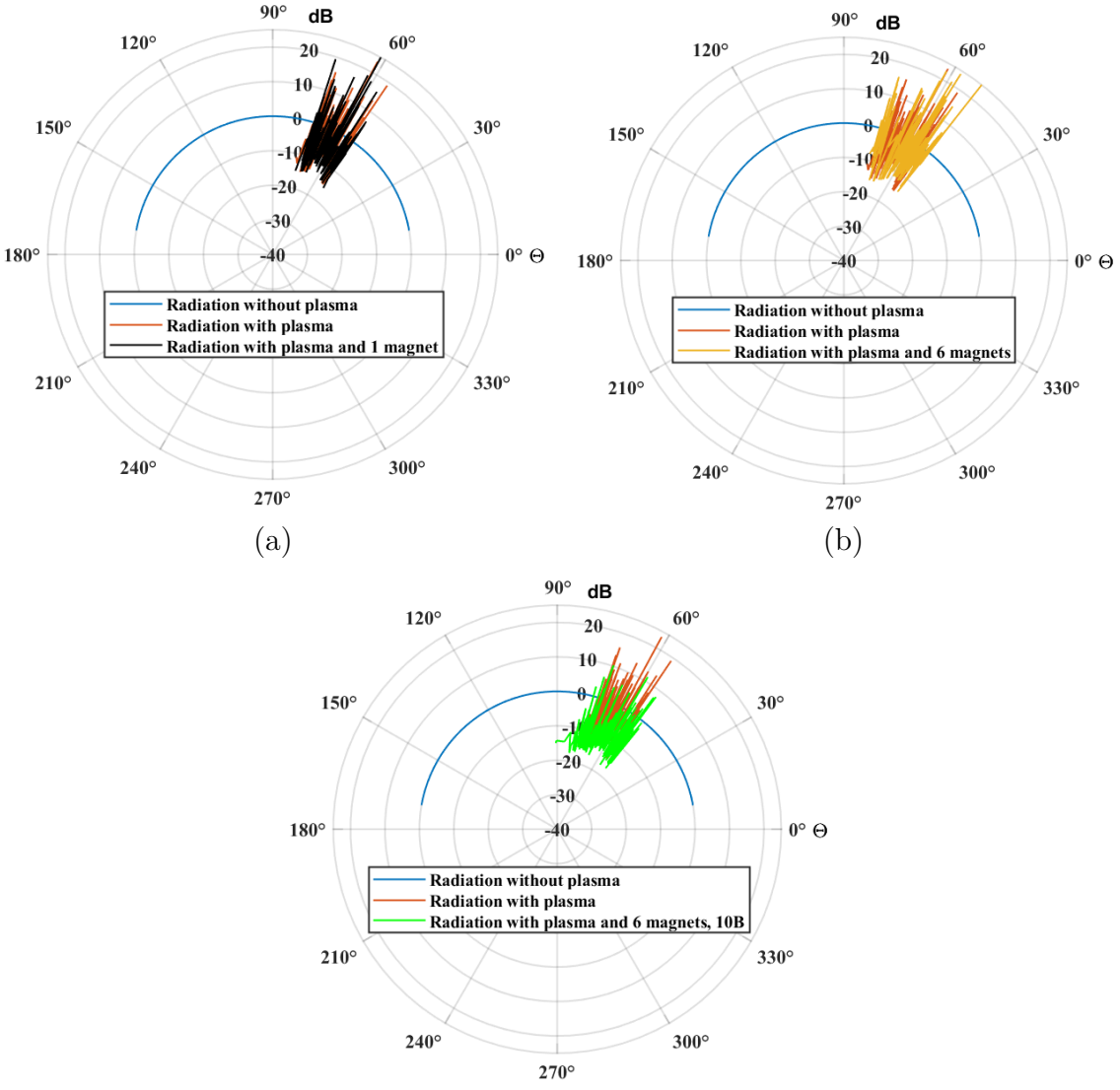

Figure 4.11: Radiation patterns for (a) initial start conditions, non-MHD and 1 magnet case, (b) initial start conditions, non-MHD and 6 magnets case, and (c) initial start conditions, non-MHD and 6 magnets case with artificially increased magnetic field.

magnet cases. Since the aperture angle increased the signal strength decreased. The signal strength over the increased radiation angle has decreased as expected and fits very well to the ray densities in Fig. 4.9 and 4.10.

4.3 Conclusion

The weak magnetic fields applied in Knapp's cases show already a significant influence on the ray tracing solution. The flow field changed due to the presence of the magnetic field and the coupled influence of the magnetic field and the EM wave has an even higher effect on the ray tracing solution, as seen in the comparison of the non-MHD case with the MHD cases. Artificially increasing the B-field shows a significant impact for the 6 magnets case. It can be concluded that a strong enough magnetic field is required to change the flow field, which agrees with the literature. In general, the results show an increase in the aperture angle for the MHD cases with increasing magnetic field strength. It is promising that further increasing the magnetic field strength will reduce or totally avoid the radio blackout. Another consequence of the radiation pattern analysis is that a brownout case needs to be further defined. If the receiving antenna aperture is not covering the aperture of the refracted signal, blackout conditions are present. In case the receiver receives the signal the power density can be stronger because of bundling the radiated energy or even weaker and noisier due to refraction.

The next step will be to analyze fluid simulations with stronger magnetic fields and re-entry vehicles like ARD or ExoMars with an applied filed. Furthermore, satellite communication aspects need to be implemented to fully analyze the signal quality. Additionally, collisions could be considered for stronger magnetic fields.

5 Signal characterization: Two-dimensional study

To enhance its capabilities for predicting signal propagation in the plasma domain surrounding a hypersonic vehicle, the BlackOut RAy Tracer (BORAT) underwent further development. A critical aspect of a comprehensive understanding of the communication cutoff phenomenon, thus blackout, is the characterization of the electromagnetic signal emitted from a radiation source like an antenna. This functionality has been integrated into BORAT 5.1. This updated version employs two methods: the first method utilizes the standard Friis equation to determine the received power at a receiving antenna, while the second method analyzes the electric field along the ray trajectory, coupled with an extended version of the Friis equation, to calculate the received power at the receiver side. The signal characteristics analysis focuses on a narrow area around the antenna, aiming for improved accuracy while achieving convergence with a slight increase in computational resources. The validity of the latter method is confirmed through plasma wind tunnel experiments conducted at the von Karman Institute for Fluid Dynamics (VKI). The experimental setup involves a transmitting antenna and a receiving antenna linked by a Vector Network Analyzer (VNA) to measure scattering parameters, including the magnitude and phase of the ratio between received and transmitted signals. The numerical tools exhibit a strong correlation with the experimental measurements conducted at VKI. Potential sources of error, such as plasma fluctuations, numerical inaccuracies, and signal losses, are duly addressed.

This chapter is based on the work published in the following research paper:

- J. S. Laur, V. F. Giangaspero, V. Sharma, A. Lani, D. Luis, A. Viladegut, J. L. Gonzales Rios, J. Querol, J. A. Vasquez Peralvo, J. C. Merlano Duncan, A. M. Hein, and J. Thoemel, "Radio Communication Blackout Mitigation: Validation of 2D Ray Tracing and Signal Analysis in Non-Magnetized Plasmas," AIAA Journal. (not published yet)

Contents

5.1 Overview

In this work, we present the progress of raytracing algorithms based on the Eikonal equations and Snell's law and include the physics of wave propagation. The latest version of BORAT can perform a 2D ray tracing analysis for non-magnetized plasma in combination with the signal characterization. The scattering parameter is calculated by applying an extended Friis transmission equation on the rays reaching the receiving antenna considering various effects like the effect of plasma, polarization changes, interference, and transmission mismatches.

5.1.1 BORAT 5.1 rationale and scheme

The signal characterization is added in BORAT 5.1 to investigate the effects of the plasma on a radio signal without the effect of an applied magnetic field. The rationale of version 5.1 is shown in Fig. 5.1. A numerical analysis of the radio

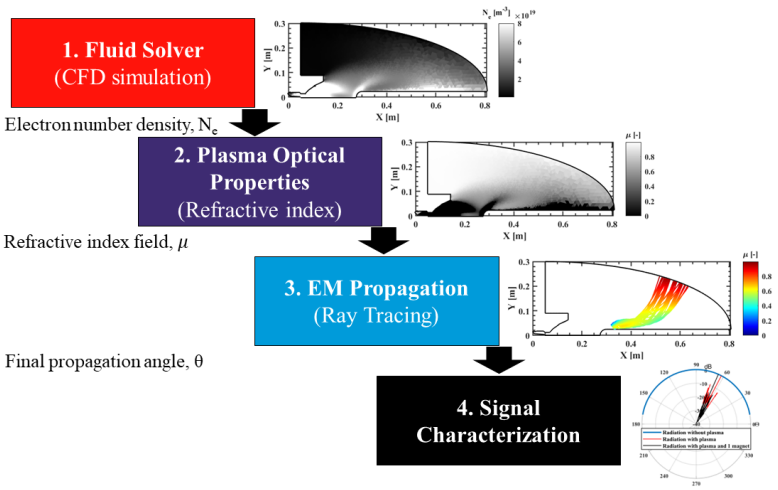

Figure 5.1: Rationale for BORAT 5.1 with signal characterization for non-magnetized plasmas.

communication blackout using BORAT 5.1 requires a Computational Fluid Dynamics (CFD) simulation as input. Providing fluid properties inside the flow domain, e.g., gas composition, temperature models, and magnetic field information. In the next step, the electron number densities in the flow domain are obtained.

Afterward, the plasma optical properties are calculated using the Appleton-Hartree equation (see section 5.1.2). The Snell's law solver or the Eikonal solver is then used to predict the ray propagation depending on the antenna aperture, antenna position, the refractive index field.

The ray tracing solution together with the information of the transmitting antenna characteristics is required as input to characterize the radio signal. The power received by the receiving antenna and the scattering parameter are calculated and possible errors are estimated. A detailed workflow is described in Fig. 6.1.

5.1.2 BORAT 5.1: Plasma optical properties

The cold plasma approximation, which neglects the thermal motion of the electrons, is valid for atmospheric entries or hypersonic flow plasmas since hypersonic atmospheric entry flows are weakly ionized and we are considering radio signals,

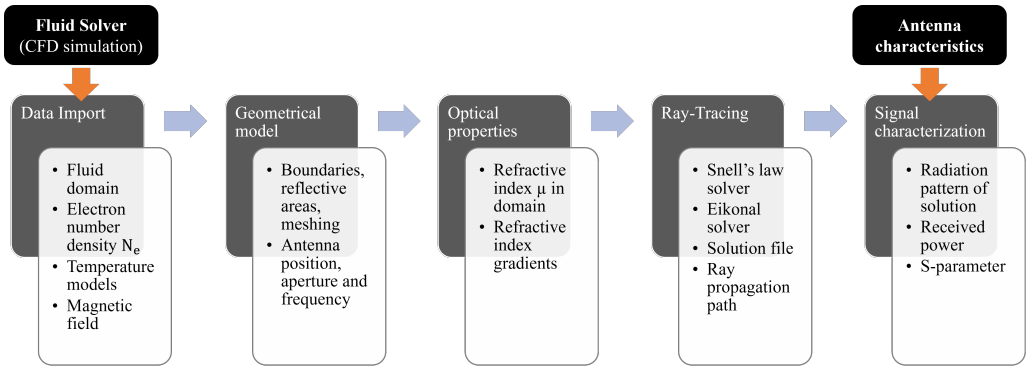

Figure 5.2: Workflow of BORAT 5.1 with signal characterization for non-magnetized Plasmas.

which travel close to the vacuum speed of light, in a plasma with a thermal electron velocity much smaller than the speed of light [54].

The governing equation to calculate the refractive index of a non-magnetized, collision-less plasma can be found in Section 2.1.3.4, Eq. 5.1 and is also repeated hereafter:

$$n = \mu = \sqrt{1 - X} = \sqrt{1 - \left(\frac{f_p}{f}\right)^2}, \tag{5.1}$$

with

$$f_p = \sqrt{kN_e}, \text{ and} \tag{5.2}$$

$$k = e^2 / \left(4\pi^2 \epsilon_0 m_e\right). \tag{5.3}$$

5.1.3 BORAT 5.1 ray tracing solvers

In version 5.1 the signal characterization is implemented for the Snell's law solver and the Eikonal solver. A detailed description of the Snell's law solver can be found in Section 2.1.2.1. A detailed description of the Eikonal solver can be found in Section 2.1.2.3.

5.1.4 Signal characterization

The novel signal characterization model to analyze the effect of plasma was added. A detailed description can be found in Section 2.2.3. The most important equation, the extended Friis equation, to account for plasma effects is repeated hereafter (see Eq. ??):

$$P_r = (1 - |\Gamma_t|^2) \cdot (1 - |\Gamma_r|^2) \cdot |\hat{\rho}_t \cdot \hat{\rho}_r|^2 \cdot \frac{|E_{t,end}|^2}{2\sqrt{\frac{\mu_0 \mu_r}{\epsilon_0 \epsilon_r}}} \cdot \frac{\lambda^2}{4\pi} \frac{|E_i(r,\Theta,\Phi)|^2}{\frac{\sum_i^N |E_i(r,\Theta,\Phi)|^2}{N}} e_{cdr}, \tag{5.4}$$

with the caclulation of the electric field along the ray trajectory (see Eq. 2.43):

$$E_1 = E_0 e^{i\omega t - nk_0} e^{-\omega(n_r - 1)\frac{\Delta r}{c_0}} e^{-\omega\chi\frac{\Delta r}{c_0}} SF. \tag{5.5}$$

The S-parameter is then calculated using Eq. 6.5 considering the convergence criterion, which is described in Section 2.2.3.4 to deliver the required number of rays to reduce numerical errors. The Ray Density Refinement method is used to perform the signal characterization at relevant antenna positions.

5.2 Results and Discussion

5.2.1 Non-plasma model verification using CST Studio Suite

5.2.1.1 Test case description

The first verification cases are a comparison of antenna simulations using Daussalt Systems' CST Studio Suite [72]. A two antenna configuration facing each other with various distances is simulated in CST and the calculated S-parameters are compared. In these cases, only the free space loss is relevant. Polarization losses, plasma attenuation, and interference are negligible because of the absence of plasma the ray trajectories are straight lines with almost similar lengths when reaching the receiving antenna, and therefore no contribution to polarization changes is present. In CST the Time Domain Solver is used for the calculations, which is a 3D full-wave solver, with both finite integration technique and transmission line matrix implementations. The test case parameters are summarized in Table 5.1: Four

Table 5.1: CST non-plasma verification test case parameters.

Antenna distance [m]	Field region	Transmitted power [W]	Efficiency [%]
0.1	Near field	0.343	36.4
0.2	Far field	0.343	31.5
0.4	Far field	0.343	33.8
0.8	Far field	0.343	33.5

different distances are analyzed in which the shortest, with 0.1 m, is in the near field. The other three distances of 0.2 m, 0.4 m, and 0.8 m are in the far field regime. The transmitted power for all cases is 0.343 W. The power value was obtained from CST and corresponds to the accepted antenna power. The efficiencies for distances of 0.1 m, 0.2 m, 0.4 m, and 0.8 m are 36.4 %, 31.5 %, 33.8 %, and 33.5 %, respectively, and are obtained from CST. The schematic of the antenna used for the CST simulations

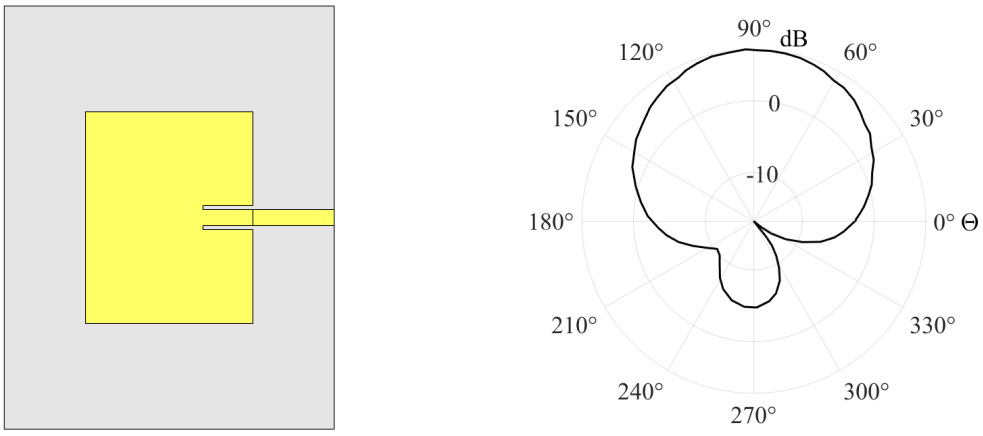

(a) (b)

Figure 5.3: Schematic of the 2.4 GHz patch antenna (a) and its directivity pattern in $\Phi = 0°$ direction reconstructed in Matlab (b).

and its radiation pattern is shown in Fig. 5.3 (a), and (b) respectively. It is a

rectangular 2.4 GHZ patch antenna with a substrate thickness of 1.6 mm and 35 μm copper electrodes. The accepted input power at the port is 0.343 W for all test cases, which was calculated in CST for a single antenna configuration.

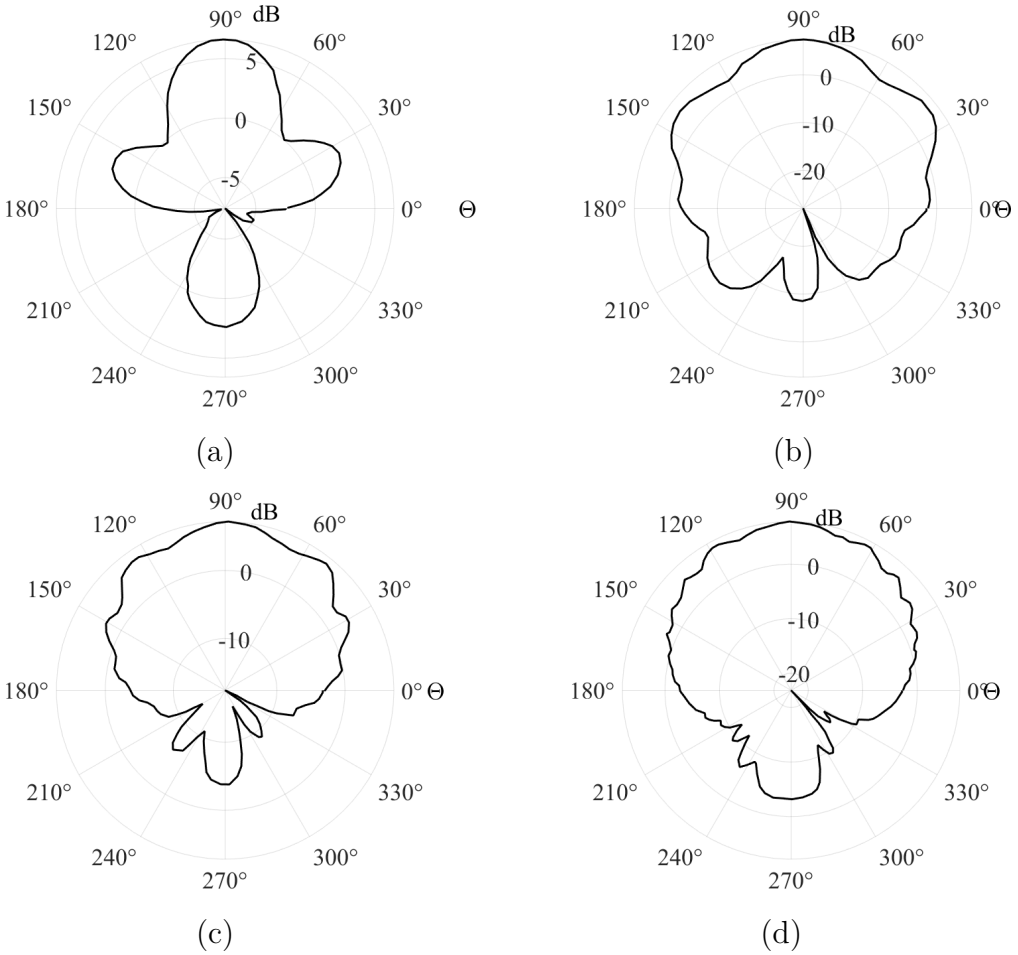

Figure 5.4: Directivity patterns of the 2.4 GHz patch antenna at $\Phi = 0°$ direction for antenna distances of (a) 0.1 m, (b) 0.2 m, (c) 0.4 m, and (d) 0.8 m.

Various distances from 0.1 m (near field) to 0.8 (far field) are analyzed to identify if there is an antenna coupling effect and the validity of the signal characterization model in the near field. The radiation patterns differ if the two antennas face each other and gradually adjust towards the single antenna pattern for greater distances as seen in Fig. 5.4. This shows a strong coupling between the antennas decreasing for greater distances. However, this coupling has an influence on the signal characterization method for near field distances.

The computational domains and their ray tracing solution for the four test cases with a ray density of 0.5 rays per degree are shown in Fig. 5.5. A constant number of rays per degree shows the necessity to increase the number of rays per degree with increasing distance. A non-plasma case results in a ray-tracing solution with straight lines and a constant refractive index of one. The radiation aperture for all cases is 180 ∘ from 90 ∘ to 270 ∘.

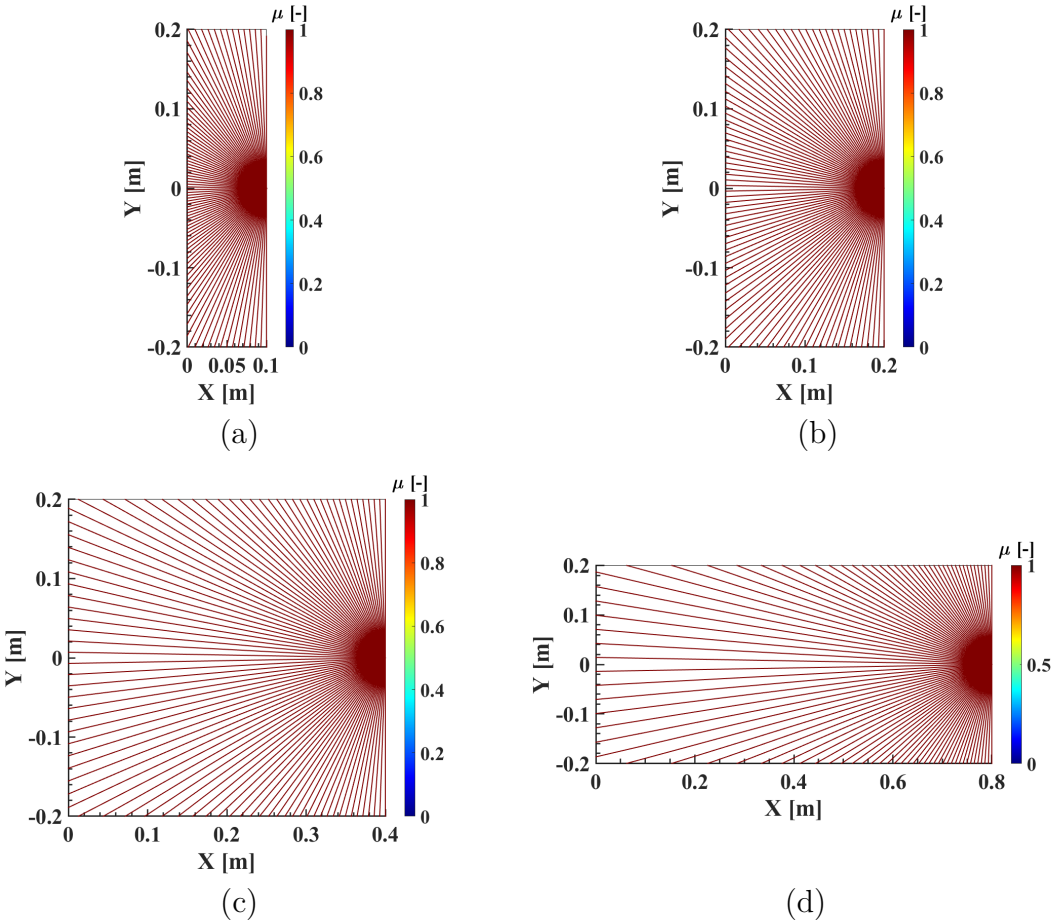

Figure 5.5: Computation domain and ray tracing solution of BORAT for antenna distances of (a) 0.1 m, (b) 0.2 m, (c) 0.4 m, and (d) 0.8 m.

5.2.1.2 Convergence analysis

It is obvious from Fig. 5.5 that the ray density needs to increase for greater distances to reach the receiving antenna at coordinates X = Y = 0. The required ray density for each case according to the convergence criterion is summarized in Table 5.2. For an antenna distance of 100 mm, a ray density of 2.13 rays per degree is required. In the case of a distance of 200 mm, the convergence criterion indicates that 4.57 rays per degree are necessary. 9.27 rays per degree and 18.59 rays per degree are required for a distance of 400 mm and 800 mm, respectively. Since the

Table 5.2: Rays per degree required to reach convergence for CST non-plasma verification test cases.

Antenna distance [m]	Rays per degree
0.1	2.13
0.2	4.57
0.4	9.27
0.8	18.59

number of rays per degree required to reach convergence might lead to a value, which is not an integer but a floating number, the number of rays applied in the Ray Density Refinement method is rounded to the closest integer value. This leads to ray densities of 2.11, 4.57, 9.29, and 11.14 rays per degree for the 100 mm, 200 mm, 400 mm, and 800 mm cases, respectively. A detailed convergence analysis was performed

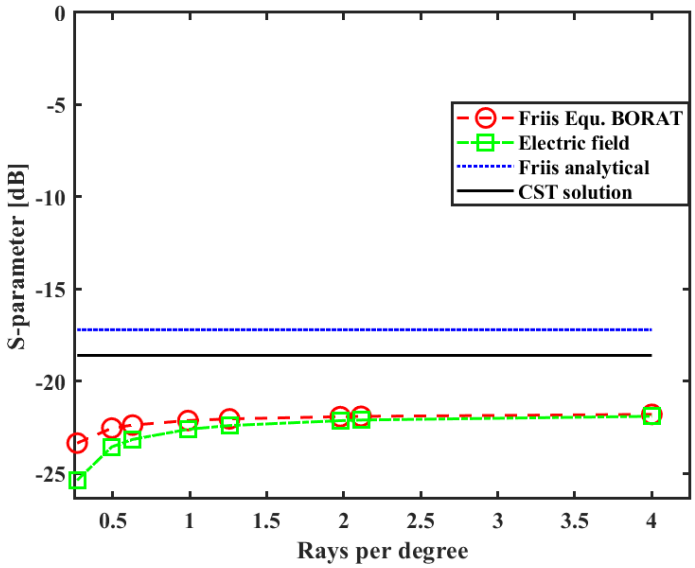

Figure 5.6: Convergence analysis in BORAT for antenna distances of 0.1 m.

for the case with 0.1 m distance (see Fig. 5.6. Comparing the S-parameters for various numbers of rays per degree shows a convergence of the solution to around -22 dB at 2 rays per degree for both the Friis equation and the Friis equation coupled with the electric field. The analytical solution of the Friis equation using the antenna directivity and the solution calculated using CST are plotted as well. The analytical Friis solution is -17.2 dB and the CST solution is -18.6 dB. The difference between

the solutions is probably due to the antenna coupling effects, which was expected since we are in the near field. In a non-plasma case, the numerical Friis equation and the Friis equation coupled with the analysis of the electric field along the ray trajectory are very similar. This is because the angles in the spread factor equation (see Eq. 2.44) are constant and therefore the spread factor is only a function of the distance similar to the free space loss of a spherical radiator. Further analysis only considers the Friis equation coupled with the electric field.

5.2.1.3 Signal intensity and radiation pattern

Part of the novel signal characterization method allows the analysis of the signal intensity along the ray trajectory. Figure 5.7 shows the signal intensity for the four distances normalized to their maximum value, which is in these cases the initial intensity. Since the ray trajectory is not altered from a straight path because no plasma is present, the intensity is decreasing similar for all cases. The only difference is the signal intensity with greater distances.

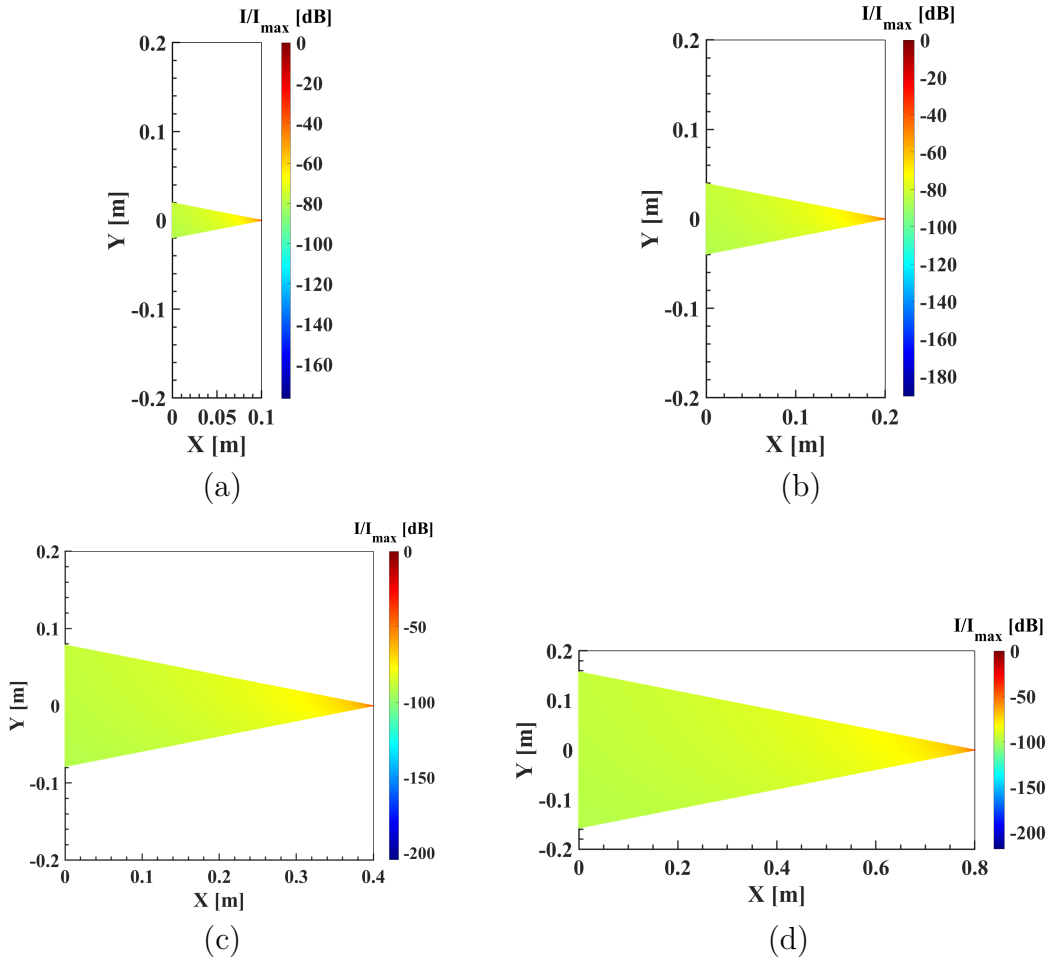

Figure 5.7: Intensity along rays of BORAT for antenna distances of (a) 0.1 m, (b) 0.2 m, (c) 0.4 m, and (d) 0.8 m.

A better insight to the final signal intensities at receiving antenna position gives the intensity pattern in Fig. 5.8. The intensity values are normalized to the maximum intensity of the initial intensity leading to an almost constant intensity value of zero for the initial radiation pattern. At a distance of 0.1 m the mean signal intensity is

Table 5.3: Normalized mean intensity in dB for antenna distances of 0.1 m, 0.2 m, 0.4 m, and 0.8 m, and the normalized initial radiation intensity.

	Initial	0.1 m	0.2 m	0.4 m	0.8 m
Normalized mean intensity [dB]	0	-78.42	-84.33	-90.31	-96.31

reduced by 78.42 dB as shown in Table 5.3. When increasing the distance by a factor of two, the mean intensity decreases by 6 dB (see Table 5.3). This makes sense since the distance is quadratic in the free space loss.

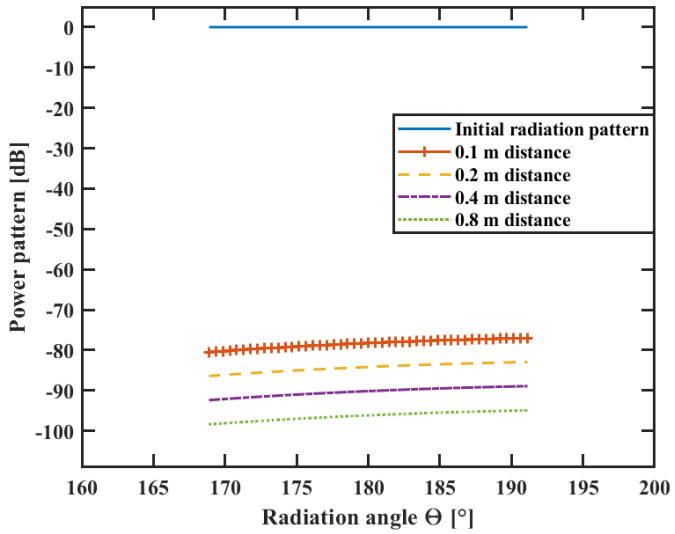

Figure 5.8: Power density pattern in dB for antenna distances of 0.1 m, 0.2 m, 0.4 m, and 0.8 m.

5.2.1.4 S-parameter analysis

Analysing the S-parameter in Fig. 5.17 for the four distances shows that the Friis equation and the Friis equation coupled with the electric field result in almost identical solutions. The offset discussed before from the BORAT solution at 0.1 m distance is reduced significantly when reaching far field conditions. This simple case shows the developed numerical tool's principle functionality to estimate an antenna network's signal characteristics. Polarization mismatches and plasma effects are not present here.

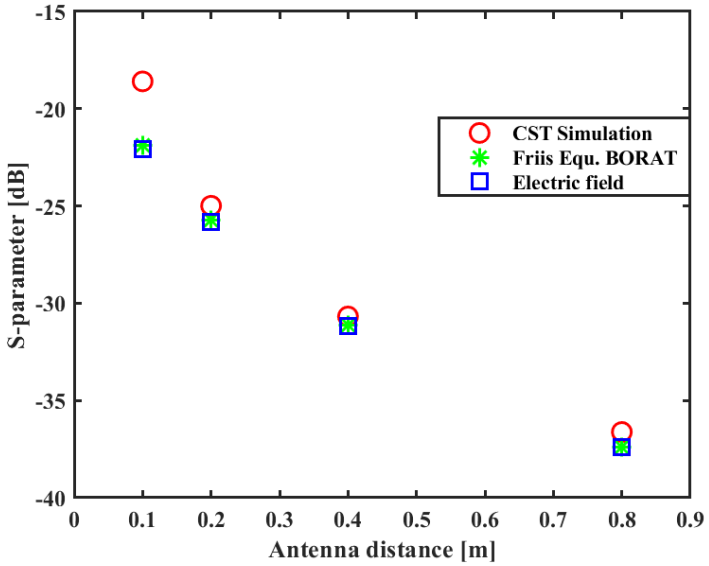

Figure 5.9: S-parameter analysis of the CST test case with antenna distances of (a) 0.1 m, (b) 0.2 m, (c) 0.4 m, and (d) 0.8 m.

5.2.2 BORAT validation with on-ground experiments at VKI

The on-ground validation experiments are performed in the Plasmatron plasma wind tunnel facility at VKI [38]. The static chamber pressure of the selected operating conditions is 15 mbar with an input power of 100 kW. Since the BORAT analysis is performed in 2D and wall reflections are not considered the operating conditions are limited to cases in which the rays are not totally reflected by the plasma stream. A broader analysis will be performed in 3D including the effect of an applied magnetic field in future work. The experimental setup consists of one receiving antenna and one transmitting antenna on opposite sides of the vacuum chamber with an axial distance of 300 mm from the torch exit as sketched in Fig. (5.10) [4]. The antennas are conical horn antennas with linear polarization (MI-wave 262A-15/0.250), each connected to a mode transition (MI-wave 284-0.250) and a waveguide to coax adapter (MI-wave 411A). The transmitting side is connected via a 3 m, and the receiving side via a 3.5 microwave cable from Huber-Suhner (SUCOFLEX 102). The S-parameters are measured using a VNA (Rhode and Schwarz ZNB 40), with DC blocks (MI-wave 8141A) installed in each port. Details of each component can be found in Table (5.4) [4]. The antenna radiation patterns are experimentally measured in the anechoic chamber at the Universitat Politecnica de Catalunya (UPC) [73]. The measurements are taken at frequencies between 33 and 40 GHz. The measured

Table 5.4: Details about the equipment used for the experiments [4].

Instruments	Antenna	Mode transition	Adapter	Cable	DC block	VNA
Connectors	custom flange	custom flange	custom flange - 2.92 mm (f)	2.92 mm (m-f)	2.92 mm (m-f)	2.92 mm (m)
Operating frequency [GHZ]	33 - 38.5	33 - 38.5	26.5 - 40	up to 46	0.01 - 40	0.01 - 40
Link budget	15 dBi	0 dB	- 0 .4 dB	-2.62 dB/m	- 0.75 dB	0 dBm

electric fields radiated by the antenna at 34, 37, and 40 GHz are converted into

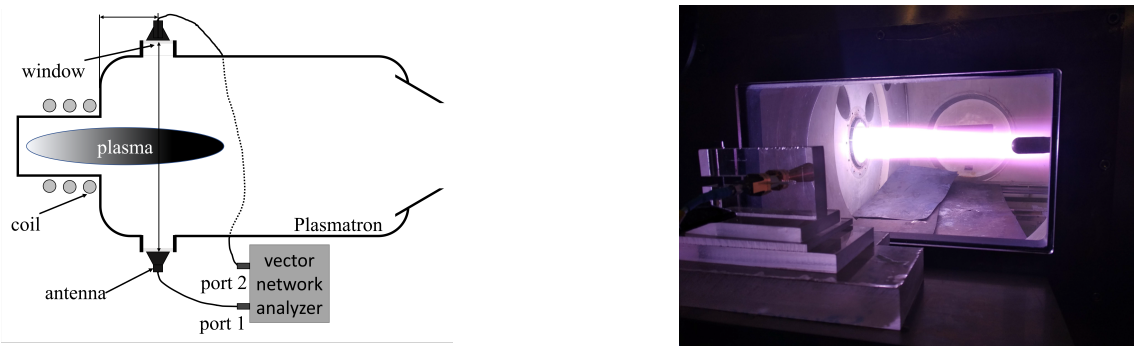

(a) (b)

Figure 5.10: Schematic of the antenna positions with respect to the CFD domain (a) and a photograph with one of the antennas during a test in the Plasmatron (b) [4].

directivity patterns as can be seen in Fig. (5.10). Those radiation patterns are rotated into the transmitting antenna direction. The corresponding pattern for the receiving antenna is rotated by 180°.

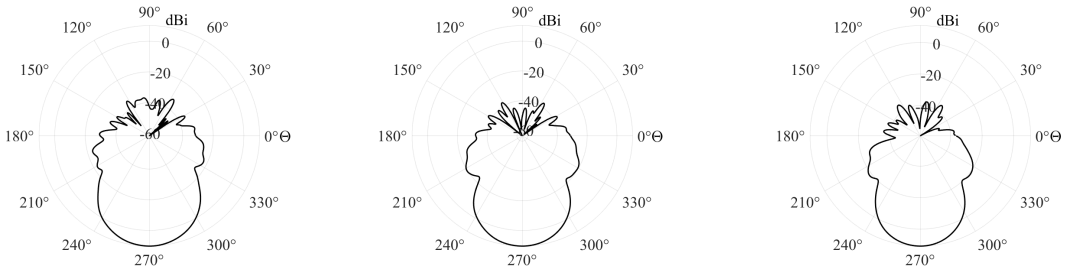

(a) (b) (c)

Figure 5.11: Antenna directivity pattern for frequencies of (a) 34 GHz, (b) 37 GHz, and (c) 40 GHz [4].

5.2.2.1 Non-plasma validation case

The ray tracing solution for the non-plasma case is shown in Fig. (5.12 (a)). The straight lines starting from the transmitting antenna at the top of the domain (x = 0.786 m, y = 0.999 m) are computed until they reach the domain boundary. The vacuum chamber diameter of the Plasmatron is 1.4 m with a depth of the window areas of 0.3 m. The distance between the antennas is therefore 2.0 m. The computational flow domain is increased to a 2 m diameter to capture the losses related to distance. The flow domain is increased around the torch area compared to the schematic in Fig. (5.10 (a)). Showing the non-plasma ray tracing solution shall give a better understanding of how the signal propagation changes when an input power of 100 kW is applied 5.2.2.2 over various frequencies. Since no plasma is present, the radiation patterns are not affected, similar to the ray propagation.

The error estimation of the experiment takes the standard deviation of the measurements into account, as well as the manufacturing errors of 0.5 dB of the antenna gain. No error estimation of the BORAT simulations is performed for the non-plasma cases. The antenna efficiency is assumed to be 100%. The signal characterization method shows a good agreement with the experimental S-parameter values as can be seen in Fig. (5.12 (b)). The S-parameter analysis was performed with

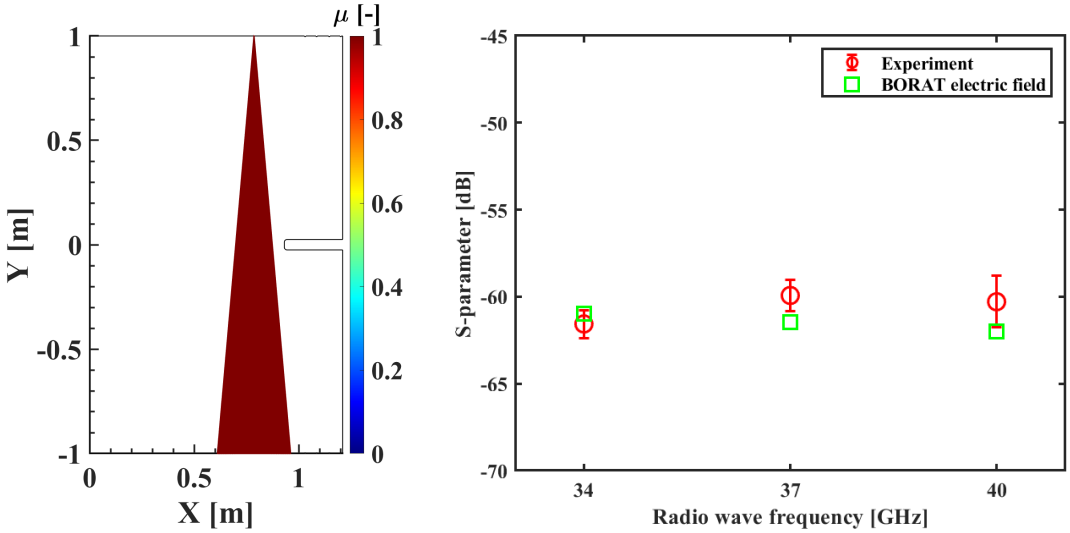

(a) (b)

Figure 5.12: Ray tracing solution of the MEESST side-to-side non-plasma case (a), and the resulting S-parameter over various radio frequencies (b).

a ray density of 40 rays per degree to reach the convergence criteria. A ray density of 20 rays per degree would be suitable for all frequencies according to the convergence analysis shown in Fig. 5.13. At 34 GHz the BORAT signal characterization results in a S-parameter close to the experimental measurements. The numerical S-parameter solutions decrease for greater frequencies since the free space loss is higher for higher frequencies. In a non-plasma case, no additional effects except the Faraday rotation due to Earth's magnetic field are relevant. However, the difference at 37 GHz is 1.5 dB, if taking the error into account the difference reduces to 0.64 dB. The S-parameter solution at 40 GHz shows that the numerical result is within the error margin of the experimental solution with a difference to the center value of 1.7 dB. Overall, the novel signal characterization method is in good agreement with the experimental solutions for non-plasma cases. Uncertainties in the numerical solutions are difficult to predict but of interest to analyze.

5.2.2.2 Plasma validation case

The electron number density in the flow domain of a plasma case at 50 mbar static chamber pressure and 100 kW input power is shown in Fig. (5.14). The electron number densities are limited to their critical electron number density of $14.3 \cdot 10^{18}$ m^{-3}, $17.0 \cdot 10^{18}$ m^{-3}, and $19.9 \cdot 10^{18}$ m^{-3} for 34 GHz, 37 GHz, and 40 GHz, respectively.

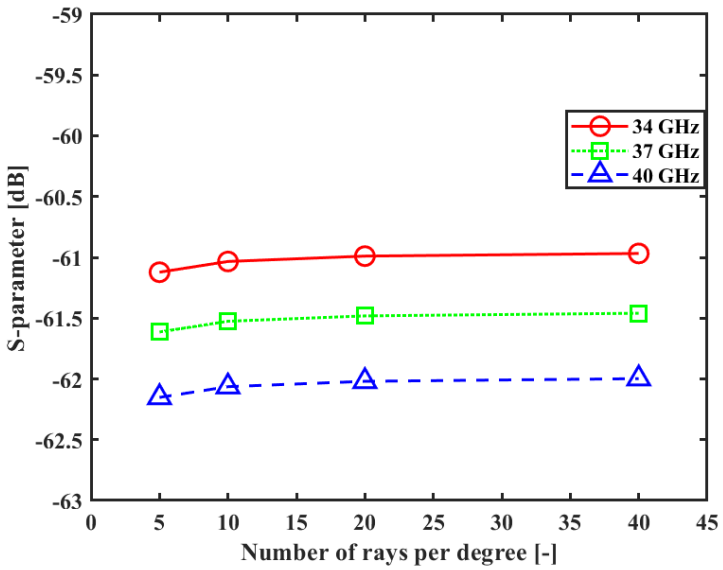

Figure 5.13: Convergence analysis for the MEESST side-to-side non-plasma case for various frequencies.

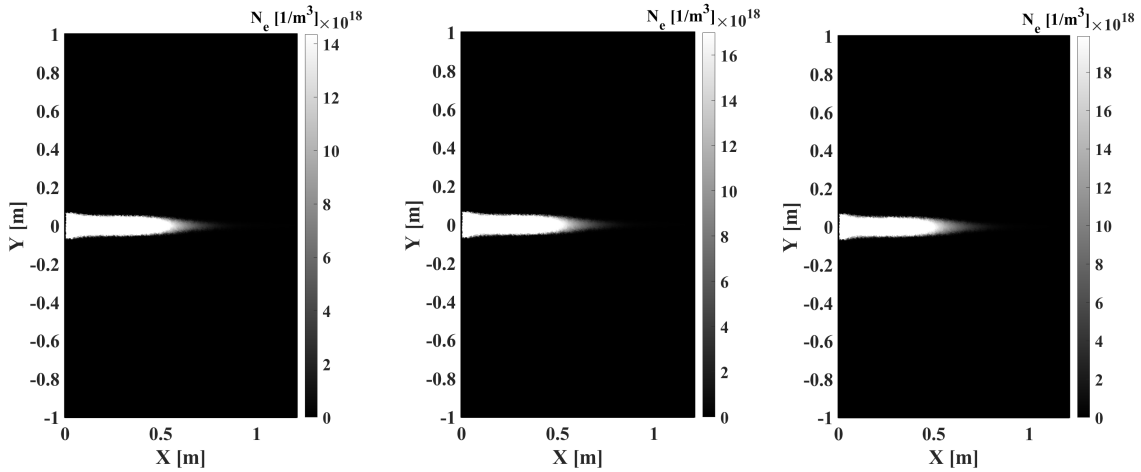

(a) (b) (c)

Figure 5.14: Electron number density in the flow domain of the MEESST side-to-side plasma case at 50 mbar static chamber pressure and 100 kW power for (a) 34 GHz, (b) 37 GHz, and (c) 40 GHz.

The differences are small but the area of the critical electron is moving upstream with higher frequency as expected. The thickness of the critical electron area in the Y-direction is similar for all frequencies.

A similar situation, as for the electron number densities in Fig. 5.14, is shown for the refractive index in the flow domain in Fig. 5.15. The refractive index for collision-less plasma is limited to a range from zero, where the critical electron number density and therefore the critical plasma frequency exceeds the radio frequency, to one, where no plasma is present. In this figure, a noticeable decrease of the critical electron number density is measurable towards upstream with a similar thickness in Y-direction for all frequencies.

The Eikonal solver has a variable step size with step size refinement at relevant

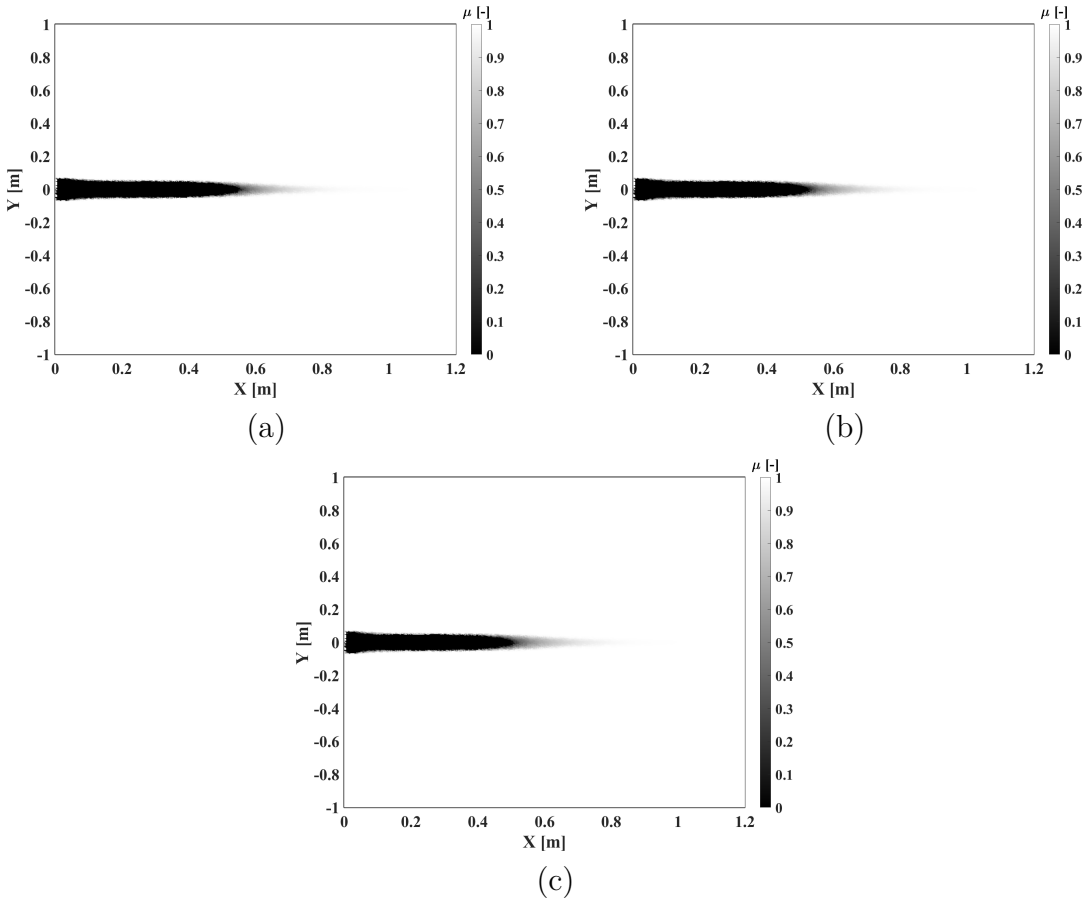

Figure 5.15: Refractive index in the flow domain of the MEESST side-to-side plasma case at 50 mbar static chamber pressure and 100 kW power for (a) 34 GHz, (b) 37 GHz, and (c) 40 GHz.

positions. However, we experienced that if the step size is too large in these cases, the ray tracing solution does not capture the plasma area in the middle of the domain. The solver oversteps the plasma area. Therefore, a step size analysis was performed to identify the maximum allowed solver step size. Figure 5.16 shows the ray tracing solutions for a maximum step size of (a) 0.125 m, (b) 0.06 m, (c) 0.03 m, and (d) 0.015 m. Larger step sizes do not account for the plasma area. As can be seen in Fig. 5.16, the ray tracing solution is not changing for max. step sizes of 0.06 m or less. 20 rays per degree are used to generate the plots.

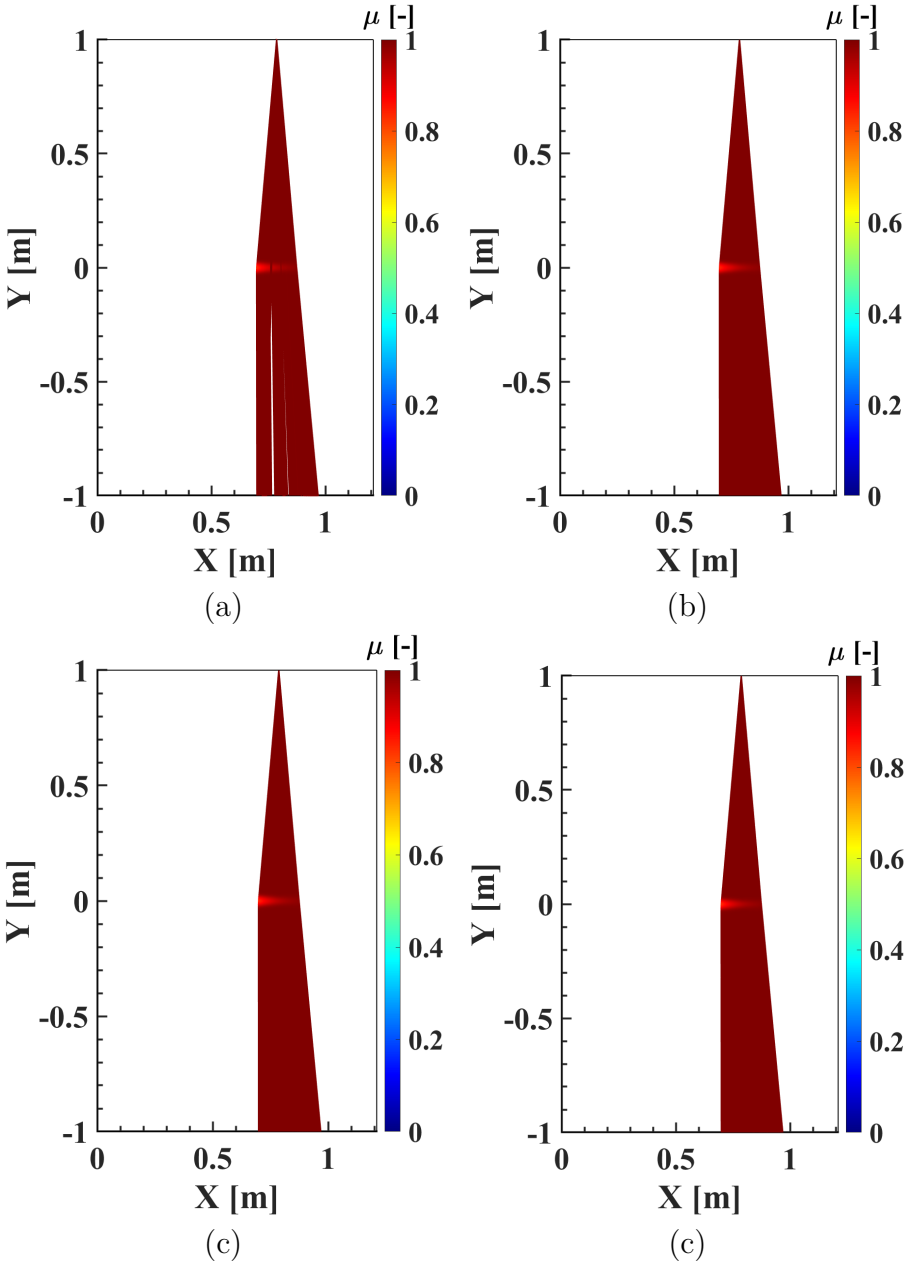

Figure 5.16: Ray tracing solutions for the MEESST side-to-side plasma case at 50 mbar static chamber pressure and 100 kW power for 34 GHz with a maximum solver step size of (a) 0.125 m, (b) 0.06 m, (c) 0.03 m, and (d) 0.015 m.

The S-parameter for step sizes from 0.5 m to 0.015 m are analyzed for all three frequencies of case at 50 mbar static chamber pressure and 100 kW power and the results for 34 GHz are shown in Fig. 5.17 using the inverse steps size as the X-axis. The S-parameter analyses are performed for a ray density of 40 rays per degree to match the convergence criteria mentioned above. This analysis shows a high fluctuation of the results for larger step sizes. The fluctuations are small when the convergence of the ray-tracing solution (at a max. step size of 0.06 m) is reached. The remaining fluctuations may be caused due to the mesh size and quality. The fluctuations remind one of a damped oscillation. This behavior is displayed in the spline fit curve.

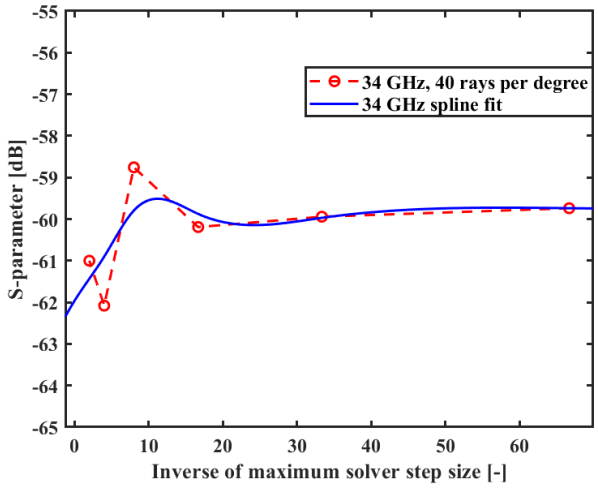

Figure 5.17: Convergence analysis for the MEESST side-to-side plasma case at 50 mbar static chamber pressure and 100 kW power for 34 GHz.

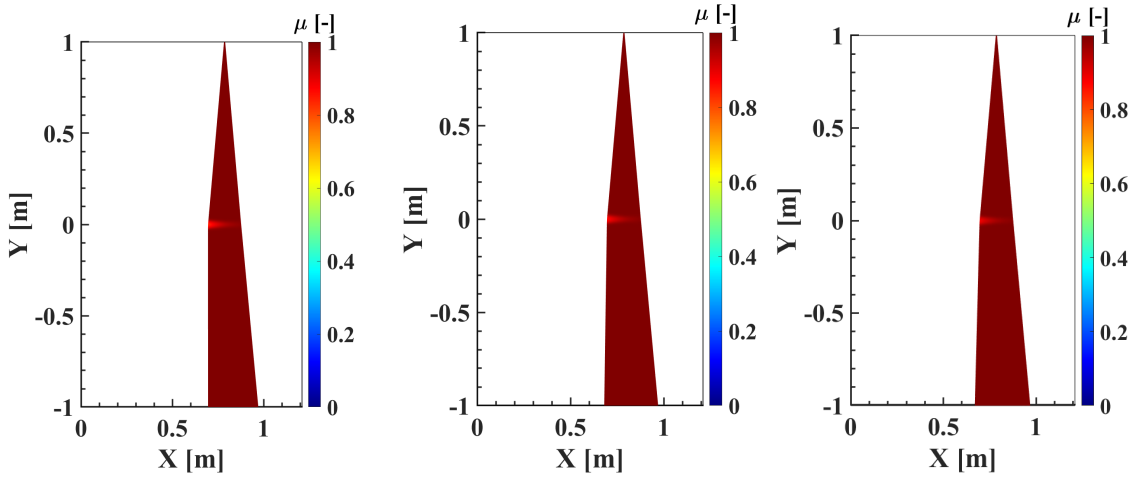

Figure 5.18: Ray tracing solutions for the MEESST side-to-side plasma case at 50 mbar static chamber pressure and 100 kW power for (a) 34 GHz, (b) 37 GHz, and (c) 40 GHz.

The ray tracing solutions, with 20 rays per degree, for the plasma case at 50 mbar static chamber pressure and 100 kW input power are shown in Fig. (5.19). The effect of the plasma on the ray propagation is decreasing if the frequency is increasing as expected. The rays upstream are less bend due to the presence of the plasma.

Investigating the normalized intensity along the ray trajectory shows a similar reduced effect of the plasma for larger frequencies as shown in Fig. 5.19. The intensities are normalized to their initial value at the transmitting antenna. The intensity is decreasing towards the plasma due to the spread factor (free space loss). Since the plasma is bending the rays downstream the spread factor is greater than one leading to an increase of the intensity which unit is in watts per square meter. After propagating through the plasma area the intensity is decreasing again.

The corresponding radiation (power/intensity) patterns after propagating through the plasma at the receiving antenna position are shown in Fig. (5.20). The ray

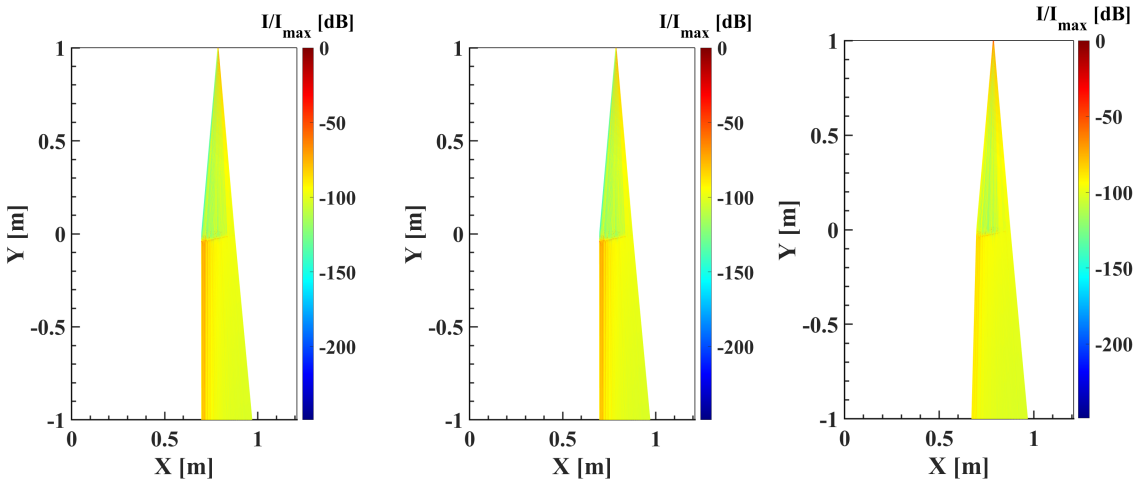

Figure 5.19: Normalized signal intensity along the ray trajectory for the MEESST side-to-side plasma case at 50 mbar static chamber pressure and 100 kW power for (a) 34 GHz, (b) 37 GHz, and (c) 40 GHz.

tracing solution is limited to an initial aperture angle of 10° according to the required aperture identified by the ray density refinement method. This results in displaying the relevant section of the total radiation pattern. The radiation intensities are normalized to the initial intensity of the transmitting antenna. All three frequencies show a higher attenuation of the signal due to the plasma at smaller propagation angles. The reduced bending for higher frequencies is visible as well in the form of smaller final propagation angles due to the reduced bending of the rays. Since the free space loss is larger for higher frequencies in combination with the reduced plasma effect the intensity at 40 GHz is lower at the whole aperture.

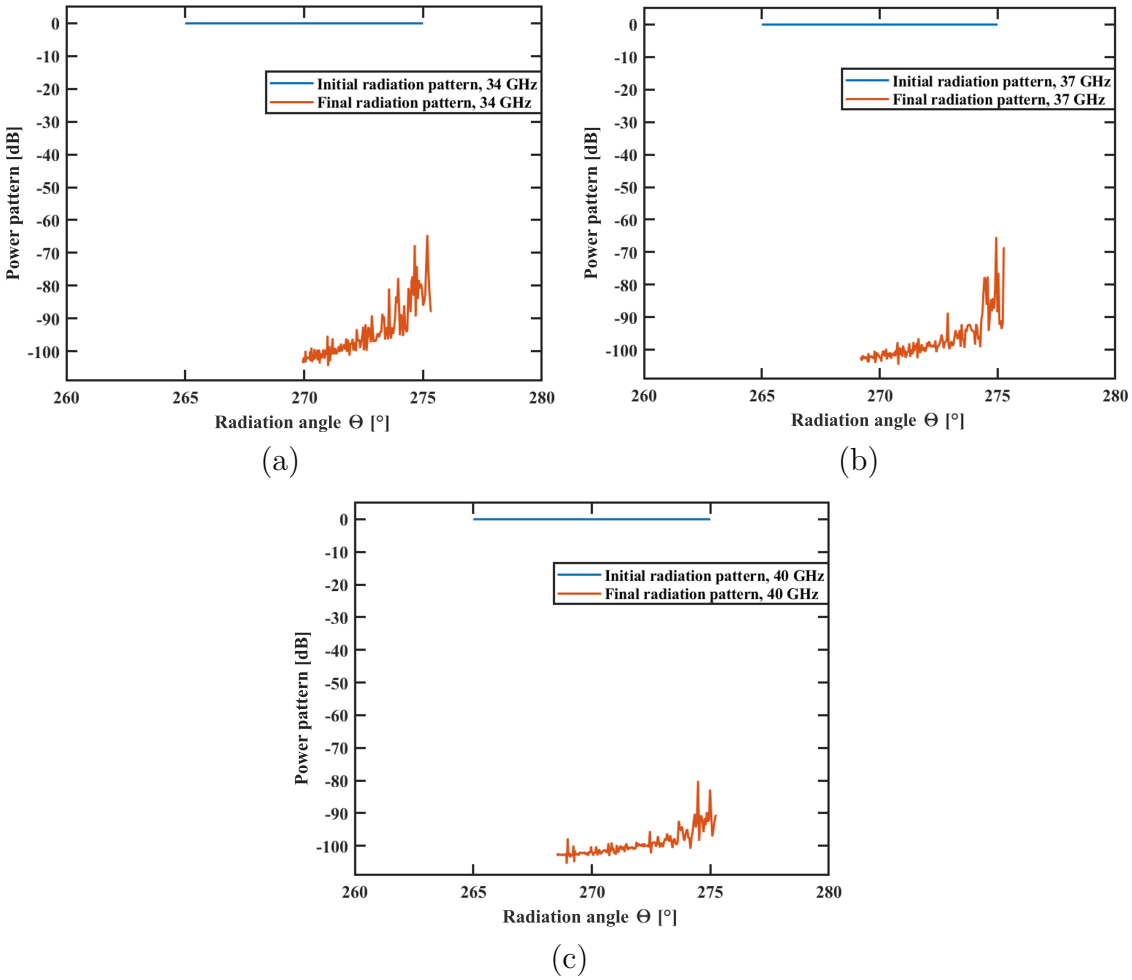

Figure 5.20: Power pattern for the MEESST side-to-side plasma case at 50 mbar static chamber pressure and 100 kW power for (a) 34 GHz, (b) 37 GHz, and (c) 40 GHz after propagation through the plasma.

The S-parameter analysis is shown in Fig. (5.21). Since heavy particle collisions are neglected in the refractive index calculation, no plasma attenuation is present. The numerical results are in good agreement with the experiment. The error margins of the experiment contain the standard deviation as well as a 0.5 dB variation due to the manufacturing uncertainties of the antenna. The error margins for the numerical solutions are due to the before-described fluctuations in the max solver step size analysis. The numerical results are within the error margins at 34 GHz, and 37 GHz and are almost identical to the experimental value at 40 GHz. The interference with the rays reaching the receiving antennas was analyzed and showed no impact on the solution.

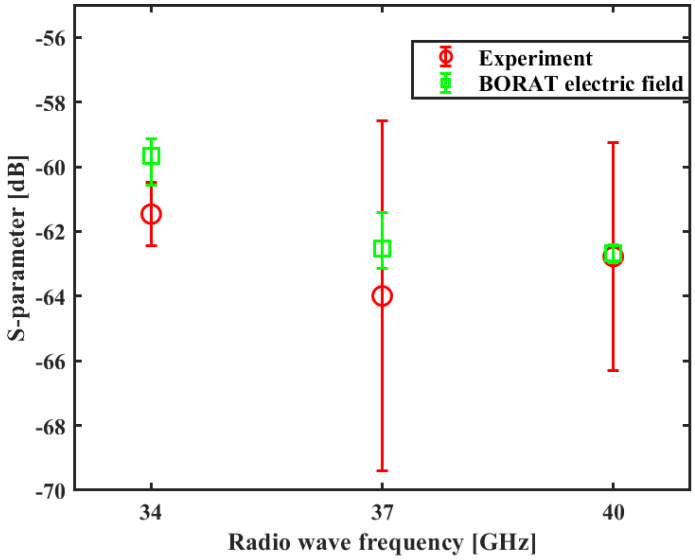

Figure 5.21: S-parameter over various radio frequencies for the MEESST side-to-side plasma case at 50 mbar static chamber pressure and 100 kW power.

5.3 Conclusion

The novel signal characterization method, which analyses the electric field along the ray trajectory, shows a good agreement with the verification and validation cases. Analyzing the electric field along the ray path allows a better insight into the physical phenomenon causing the radio blackout. The analyzed plasma case shows that the plasma causes an increase in intensity because the rays are bent toward each other leading. This effect seems to have a greater impact than losses due to the refraction process. The free space loss, which is increasing for higher frequencies, and the effect of the plasma on the spread factor seem to be counterparts.

Finally, the validation with the on-ground experiments at VKI is successful and the developed signal characterization method gives valuable insights into the physics causing radio blackout. Further investigations to analyze the effect of an applied magnetic field including experimental on-ground validation are subject to future research, as well as a 3D analysis to capture possible neglected 3D effects.

6 Magnetized plasma & signal characterization: Two-dimensional study

Further enhancing its capabilities for predicting signal propagation in magnetized plasma, the BlackOut RAy Tracer (BORAT) underwent further development. The behavior of the optical properties of a magnetized plasma is analytically analyzed and the effect on the ray propagation path of the ordinary and extraordinary rays is analyzed. The validity of the latter method is analyzed through plasma wind tunnel experiments conducted at the von Karman Institute for Fluid Dynamics (VKI). The experimental setup involves a transmitting antenna and three receiving antennas linked by a Vector Network Analyzer (VNA) to measure scattering parameters, including the magnitude and phase of the ratio between received and transmitted signals. The results of the numerical tool agree with the experimental measurements conducted at VKI for non-plasma cases. In the presence of a (magnetized) plasma, the numerical solutions could not reproduce the experimental results. Potential sources of error, such as plasma fluctuations, numerical inaccuracies, and signal losses, are not considered due to partially large discrepancies between the numerical and experimental results, thus, error estimations are negligible. The suitability of the of the magnetic windowing method to mitigate radio blackout is analyzed and further insights are gained.

This chapter is based on the work published in the following research paper:

- J. S. Laur, V. F. Giangaspero, V. Sharma, A. Lani, D. Luis, A. Viladegut, J. L. Gonzales Rios, J. Querol, J. A. Vasquez Peralvo, J. C. Merlano Duncan, A. M. Hein, and J. Thoemel, "Radio Communication Blackout Mitigation: Validation of 2D Ray Tracing and Signal Analysis in Magnetized Plasmas," AIAA Journal. (not published yet)

Contents

6.1 Overview

In this work, we present the progress of ray-tracing algorithms based on the Eikonal equations and including the physics of wave propagation, The latest version of BORAT is capable of performing a two-dimensional ray tracing analysis for magnetized plasma including possible bi-refraction in combination with the signal characterization. The ray tracing method is extensively tested and verified to literature and validated with on-ground experiments performed by our MEESST project partner at the Von Karman Institute for Fluid Dynamics (VKI).

The scope of this section is to answer the following questions:

1. How are the ray propagation and the signal affected by the magnetic field?

2. Is the magnetic window method sufficient to mitigate radio communication blackout?

6.1.1 BORAT 5.2 rationale and scheme

BORAT 5.2 was designed to study the impact of plasma on a radio signal, along with the influence of an applied magnetic field. The working principle of BORAT 5.2 is illustrated in Fig. 6.1.

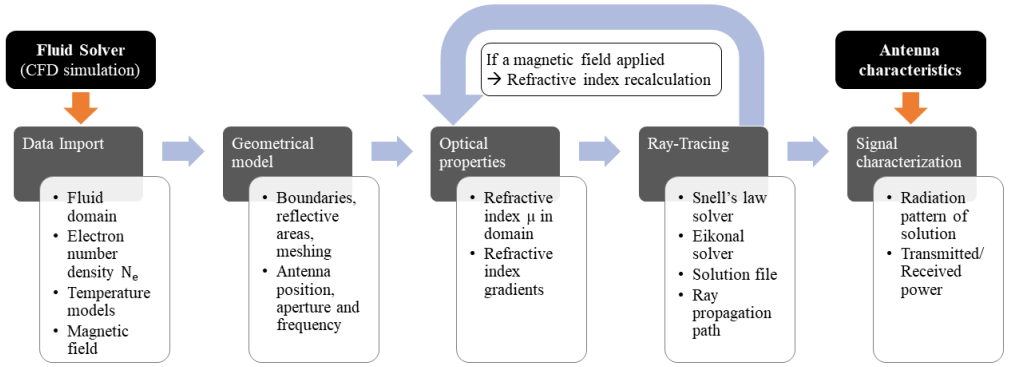

Figure 6.1: Workflow of BORAT 5.2 with signal characterization for magnetized plasmas.

BORAT 5.2 necessitates a Computational Fluid Dynamics (CFD) simulation as input. The necessary fluid properties within the flow domain, such as gas composition, temperature models, and magnetic field data are gathered. Subsequently, the electron number densities in the flow domain are obtained.

Subsequently, the plasma optical properties are determined using the Appleton-Hartree equation (see Section 6.1.2). Depending on the antenna aperture, antenna position, and the refractive index field, either the Snell's law solver or the Eikonal solver is employed to predict the ray propagation. The refractive index is coupled to the wave propagation, as given in Eq. 2.15, it is iteratively determined.

The ray tracing solution, combined with the transmitting antenna characteristics, is necessary to characterize the radio signal. The received power at the receiving antenna and the scattering parameter are then calculated, with possible errors being estimated. A detailed workflow is depicted in Fig. 6.1.

6.1.2 BORAT 5.2: Plasma optical properties

The equation governing the calculation of the refractive index of a magnetized, collision-less plasma is provided in Section 2.1.3.2, Eq. 2.15, and is reiterated below:

$$(\mu - \chi i)^2 = 1 - \frac{X(1-X)}{1 - X - Y^2 sin^2(\Theta) \pm \sqrt{\frac{1}{4}Y^4 sin^4(\Theta) + Y^2 (1-X)^2 cos^2(\Theta)}}. \quad (6.1)$$

This study does not analyze the differences between collision and collision-free magnetized plasma. However, literature such as [56] mentions the increased sensitivity to collisions. This topic will be addressed in a future article.

6.1.3 BORAT 5.2: Signal characterization

Figure 6.2 presents the previously introduced schematic of the electric field calculation along a ray trajectory. Tx and Rx denote the transmitting and receiving antennas, respectively. The varying gray scales indicate regions with different refractive indices, while the black horizontal line at position E_7 represents a reflective surface.

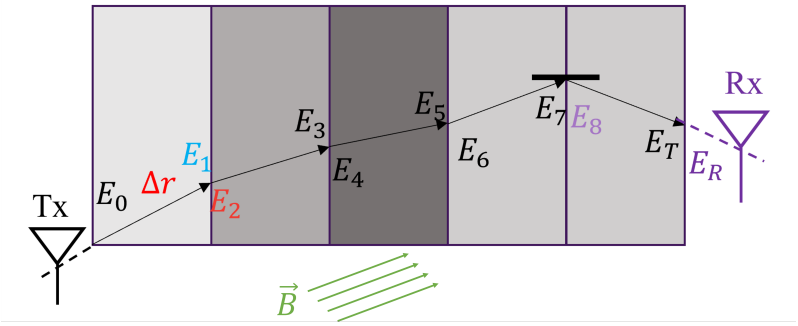

Figure 6.2: Schematic of the electric field calculation along a ray trajectory. The different gray scales represent different refractive indexes in a domain with an arbitrary magnetic field.

The amplitude of the electric field along the ray trajectory with a constant refractive index is determined using the wave equation [59]:

$$E_1 = E_0 e^{i\omega t - nk_0} e^{-\omega(n_r - 1)\frac{\Delta r}{c_0}} e^{-\omega\chi\frac{\Delta r}{c_0}} SF, \quad (6.2)$$

By converting the amplitude of the electric field vector $E_{t,end}$ at the Rx antenna into the Poynting vector for each ray, and combining Equations 2.37, 2.38, and 2.40 while incorporating the losses in the antenna network as described by the Friis equation (Eq. 2.34), we obtain:

$$P_r = (1 - |\Gamma_t|^2) \cdot (1 - |\Gamma_r|^2) \cdot |\hat{\rho}_t \cdot \hat{\rho}_r|^2 \cdot S_{t,end} \cdot \frac{\lambda^2}{4\pi} \cdot D_r \cdot e_{cdr} \cdot ILF, \tag{6.3}$$

$$D_r = \frac{|E_i(r,\Theta,\Phi)|^2}{\frac{\sum_i^N |E_i(r,\Theta,\Phi)|^2}{N}},$$

$$S_{t,end} = \frac{|E_{t,end}|^2}{2\sqrt{\frac{\mu_0\mu_r}{\epsilon_0\epsilon_r}}},$$

$$ILF = cos\left(\frac{\Delta L}{\lambda} \cdot 2\pi\right).$$

Equation 6.1.3 is introduced in Section 2.2.3.

$$P_{Rx} = \frac{1}{N}\sum_k^N P_{r,k}. \tag{6.4}$$

The aggregate power received by an Rx antenna from all rays reaching it is computed using Eq. 6.4. This calculation is essential for conducting S-parameter analysis to validate the results.

$$\begin{aligned} S_{b_2,a_1} &= \sqrt{\frac{P_{b_2}}{P_{a_1}}}, \\ &..., \\ S_{b_n,a_1} &= \sqrt{\frac{P_{b_n}}{P_{a_1}}} \end{aligned} \tag{6.5}$$

Hereby, P_{a_1} stands for the transmitted power, and P_{b_i} with $i = 2 - n$ stands for the received power P_r at each receiving antenna.

6.2 Results

6.2.1 Analytical and numerical verification of the MHD effect onto the refractive index and ray tracing

The refractive index was analyzed for a magnetized and non-magnetized collisionless plasma. In case no magnetic field is applied the refractive index depends only on the radio frequency according to Eq. 5.1 independent of the propagation direction of the EM wave.

As soon as a magnetic field is applied the extended version of the Appleton-Hartree equation accounting for the magnetic field (see equation 2.15) becomes of importance. The refractive index becomes a function of the radio frequency, the magnetic field strength and direction, and the electron number density. The refractive index was calculated for three different angles between the wave vector and the magnetic field vector (0, 45, and 90 degrees), and for five different electron number densities with corresponding refractive indexes of 0.999, 0.9, 0.7, 0.5, 0.2, and 0.1 in non-magnetized plasma for a frequency of 2.4 GHz (see Eq. 5.1).

It showed that the refractive index of a ordinary wave propagating in a magnetized plasma with a magnetic field parallel to the wave vector is greater than the refractive index in a non-magnetized plasma and increases with magnetic field strength. This

increase in refractive index with the magnetic field strength is greater with increasing electron number densities (decreasing refractive index in non-magnetized plasma).

The refractive index of the extraordinary wave also increases with increasing magnetic field strength until reaching a peak value at around 0.1 T further decreasing again and asymptotically converging to a refractive index of one. Also interesting is the reduced refractive index to roughly zero increasing electron number densities and small magnetic field strengths. This can lead to cut-off conditions in case where the ray is propagating away from a magnet with a gradient in magnetic field strength in a domain with constant or increasing electron number density.

Analyzing a wave propagation perpendicular to the magnetic field vector shows the unaffected refractive index for the ordinary wave. The refractive index of the extraordinary wave is asymptotically converging to a refractive index of one with increasing magnetic field strength. There is one exception in the analyzed data for a magnetic field strength of 0.05 T and an electron number densities of $3.65\mathrm{E}+16\mathrm{m}^{-3}$ (refractive index of 0.7 in non-magnetized plasma) in which the refractive index results in roughly zero.

With an angle of 45 degrees between the wave vector and the magnetic field vector the refractive index of the extraordinary wave behaves in a similar manner to the extraordinary wave in the perpendicular case. The refractive index of the ordinary wave is also higher when a magnetic field is applied compared to a non-magnetized plasma. However, the effect is significantly smaller compared to a wave vector parallel to the magnetic field. This leads to the conclusion that the effect of a magnetic field is best when the EM wave is traveling in a magnetic field vector direction getting weaker until reaching the unaffected case where the EM wave propagates perpendicular to the magnetic field vector.

When a wave travels parallel to a constant magnetic field parallel with variable electron number density the gradient in the refractive index is small causing small refraction angles. However, after the first refraction process, no further predictions can be made in the following refractive index corresponding to the angle between the wave vector and the magnetic field vector for an arbitrary case.

When a wave travels perpendicular to a constant magnetic field parallel with variable electron number density the gradient in the refractive index can become large causing significant refraction angles. Again, after the first refraction process, no further predictions can be made in the following refractive index corresponding to the angle between the wave vector and the magnetic field vector for an arbitrary case.

The results of the analytical refractive index analysis of the effect of an applied magnetic field are illustrated in Fig. 6.3. The left side corresponds to the extraordinary wave and the right side to the ordinary wave, respectively.

The ray tracing solutions for a constant electron number density field with various magnetic field strengths are shown in Fig. 6.4. The refractive index in Fig. 6.4 (a) is 0.2 without an applied magnetic field. All three rays (0, 45, and 90 degrees) result in straight lines as expected with a constant refractive index along the ray trajectories. No rays a displayed in Fig. 6.4 (b) for the extraordinary wave with a magnetic field of 0.01 T in the X-direction since this case represents a cut-off condition for all rays. This behavior was mentioned before. The refractive index in Fig. 6.4 (c) of the ordinary wave in a magnetic field of 0.01 T is different for each ray. The refractive index is increasing with a reduced angle between the magnetic field vector and the

wave vector. When a magnetic field of 0.25 T is applied the refractive index of the extraordinary wave becomes one or greater than 1 (Fig. 6.4 (d)), and the increase of refractive index with reduced angle between the wave propagation vector and magnetic field vector becomes more significant (Fig. 6.4 (e)).

Rays starting from a region with a refractive index of 0.2 and traveling in a region with a refractive index of one without an applied magnetic field are shown in Fig. 6.5 (a). The ray towards the Y-direction is in a constant refractive index field, and results in a straight line. The ray towards negative X-direction is also a straight line but its refractive index changes. Since the angle between the incident ray and the normal of the refractive index domain is zero, the ray is not bent. The ray traveling in 45 degrees to the X-, and Y-direction is refracted according to Snell's law. In a magnetic field of 0.01 T towards the negative X-direction, the extraordinary wave is in cut-off conditions (Fig. 6.5 (b)), and the ordinary wave (Fig. 6.5 (c)) shows the increase of refractive index along the ray trajectory for propagation direction with an angle of fewer than 90 degrees between the wave vector and the magnetic field vector with less bending at the refraction position in the middle of the domain at X = 0.2 m. Similarly, the ordinary wave (Fig. 6.5 (d)) in a magnetic field of 0.25 T shows the same behavior with further increased refractive indexes. The extraordinary waves show a refractive index of at least one for all three rays (Fig. 6.5 (d)).

A scenario in which rays start in an area with a refractive index of 0.7 in a non-magnetized plasma is shown in Fig. 6.6 (a). The refractive index for $X < 0.4$ is equal to one. The refractive index along the trajectory is as expected according to Snell's law with a refraction process that bends the ray traveling initially toward 45 degrees of the X- or Y-direction. The extraordinary wave in Fig. 6.6 (b) is not in cut-off conditions because the low electron number density in combination with the magnetic field strength of 0.01 T enables the ray propagation (see Fig. 6.3 (a, c, e)). The refractive index for $X > 0.4$ is smaller than in the non-magnetized plasma case. The ray tracing solution for the ordinary wave at 0.01 T and 0.25 T shows a similar behavior as described earlier. The magnetic field causes an increase in the refractive index for angels between the wave vector and the magnetic field vector less than 90 degrees. The rays starting at 45 degrees to the Y-direction experience therefore less bending at the refraction position (see Fig. 6.6 (c, e). When a magnetic field of 0.25 T is applied the refractive index of the extraordinary wave is at least one in the whole domain as can be seen in Fig. 6.6 (d).

In the case of a non-magnetized plasma with rays starting in a domain with a larger refractive index ($X > 0.4$ m), in this case, a refractive index of one, and a domain with a smaller refractive index below $X = 0.4$ m the ray traveling in 45 degrees to the Y-direction gets reflected due to the large refractive index gradient. The ray propagating in the Y-direction is unaffected. Ray propagation in the negative X-direction causes refraction without bending but a significant reduction in the electron number density. An applied magnetic field is significantly reducing this reduction of the electron number density for ordinary waves. The magnetic field does not affect rays propagating 90 degrees toward the magnetic field vector and has a small influence on the ray propagating at an angle of 45 degrees toward the magnetic field vector. A magnetic field strength of 0.25 T is causing a straight ray propagation for the extraordinary wave. In case only 0.01 T is applied, the ray in the negative X-direction of the extraordinary wave gets reflected because of cut-off conditions at larger electron number densities. The ray in 45 degrees towards the

magnetic field vector gets reflected due to the large refractive index gradient. For visualization see Fig. 6.7.

When the refractive index gradient is smaller (from one to 0.7 at X = 0.4 m) the ray traveling at 45 degrees to the Y-axis follows a curved path and is not directly reflected. The lens effect of the refractive index causes the ray to travel backward. As soon as a magnetic field is applied the refraction angle becomes significantly smaller for the ordinary wave. The extraordinary wave at 45 degrees to the Y-axis is also traveling backward after the refraction process with a smaller bending radius due to the smaller refractive index below X = 0.4 m. The extraordinary wave at 0.25 T is unaffected as mentioned before. The graphical representation of the described behavior can be found in Fig. 6.8.

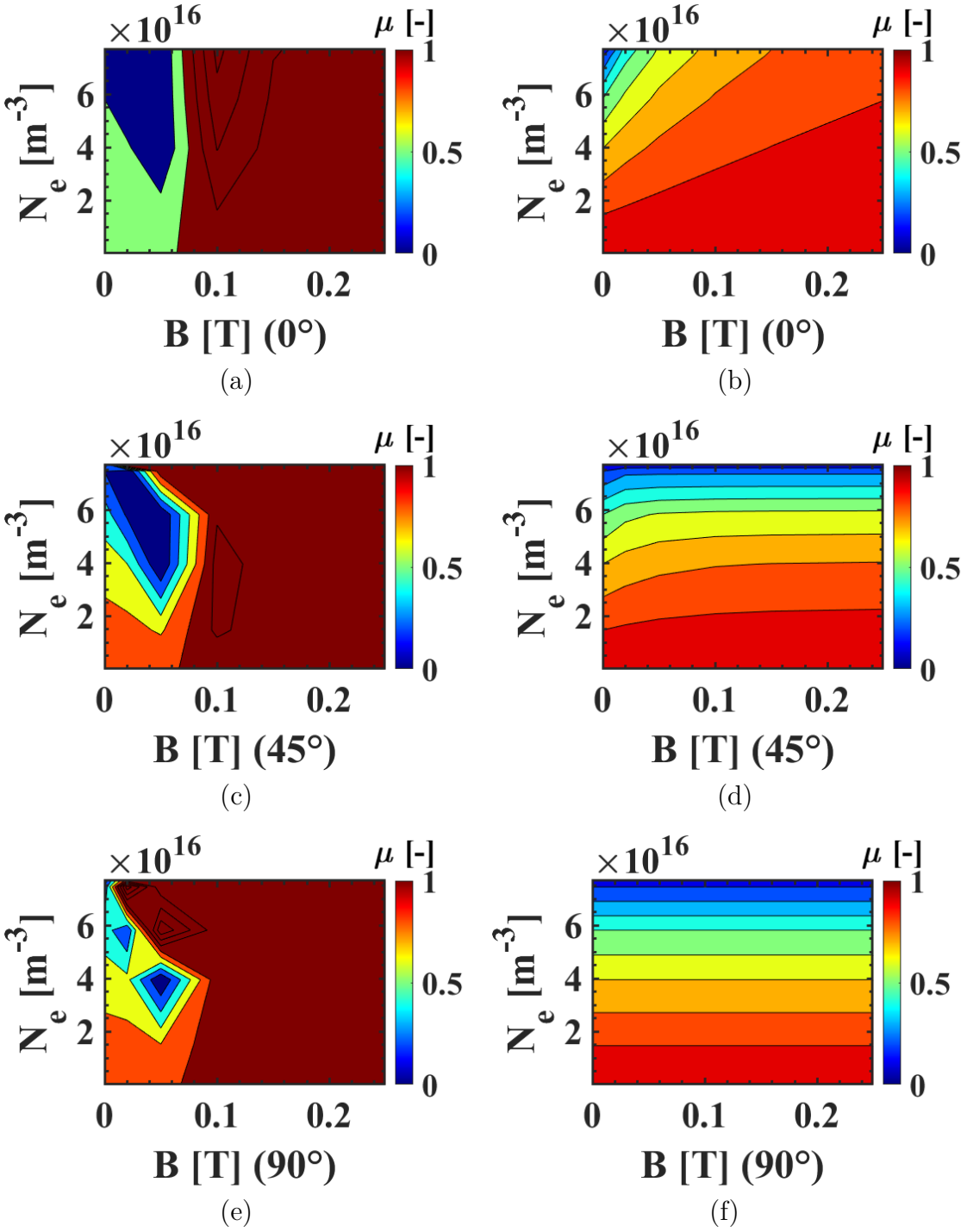

Figure 6.3: The results of the analytical refractive index analysis of the effect of an applied magnetic field for a wave propagating parallel to the magnetic field vector of the (a) extraordinary and (b) ordinary wave, a wave propagation at an angle of 45 degree to the magnetic field vector of the (c) extraordinary and (d) ordinary wave, and a wave propagation perpendicular to the magnetic field vector of the (e) extraordinary and (f) ordinary wave.

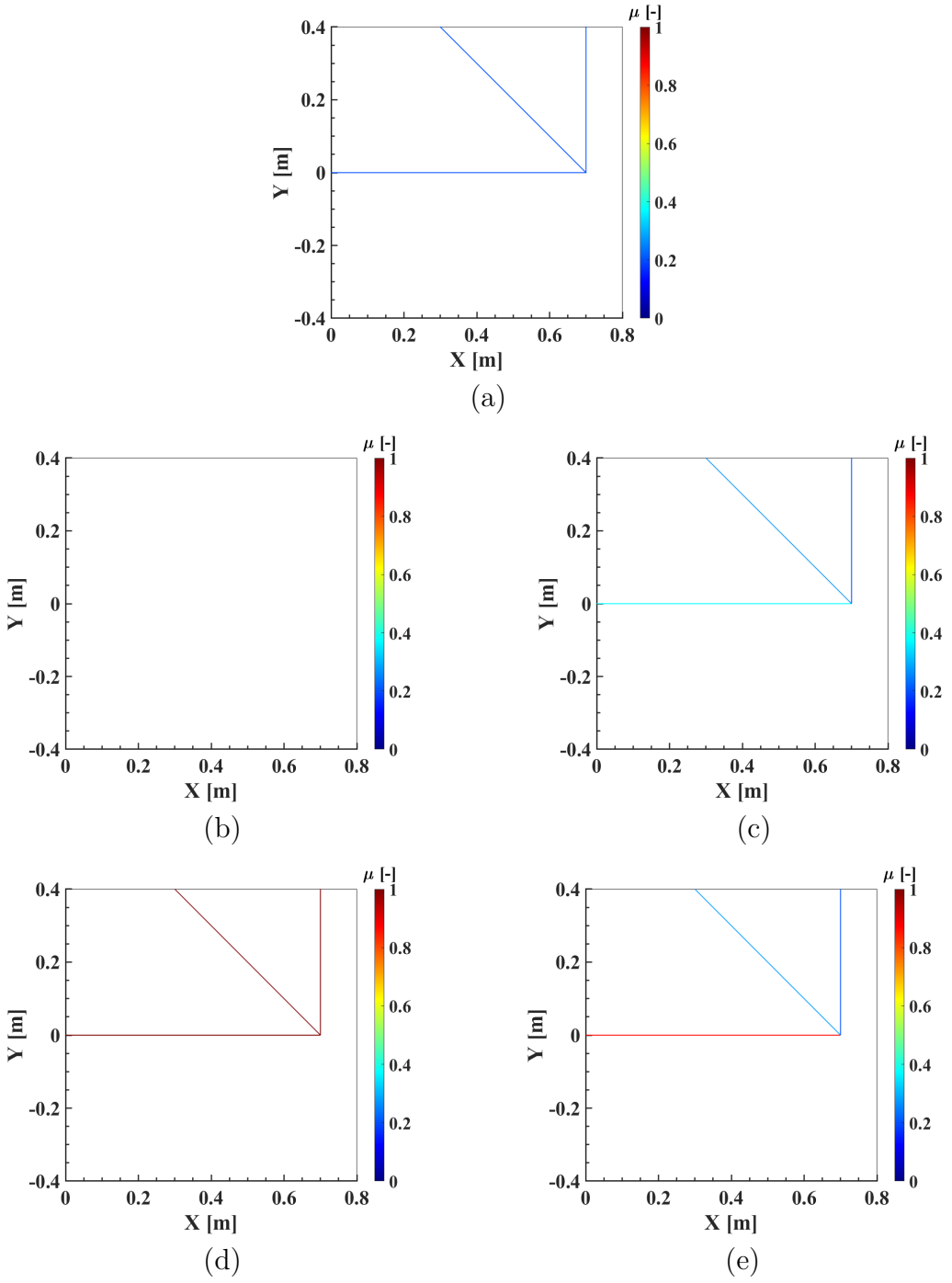

Figure 6.4: Ray tracing analysis for a constant electron number density in the domain (a) with an applied magnetic field in negative X direction of 0.01 T (b, c), and 0.25 T (d, e) for propagation parallel, perpendicular and 45 degrees to the magnetic field vector.

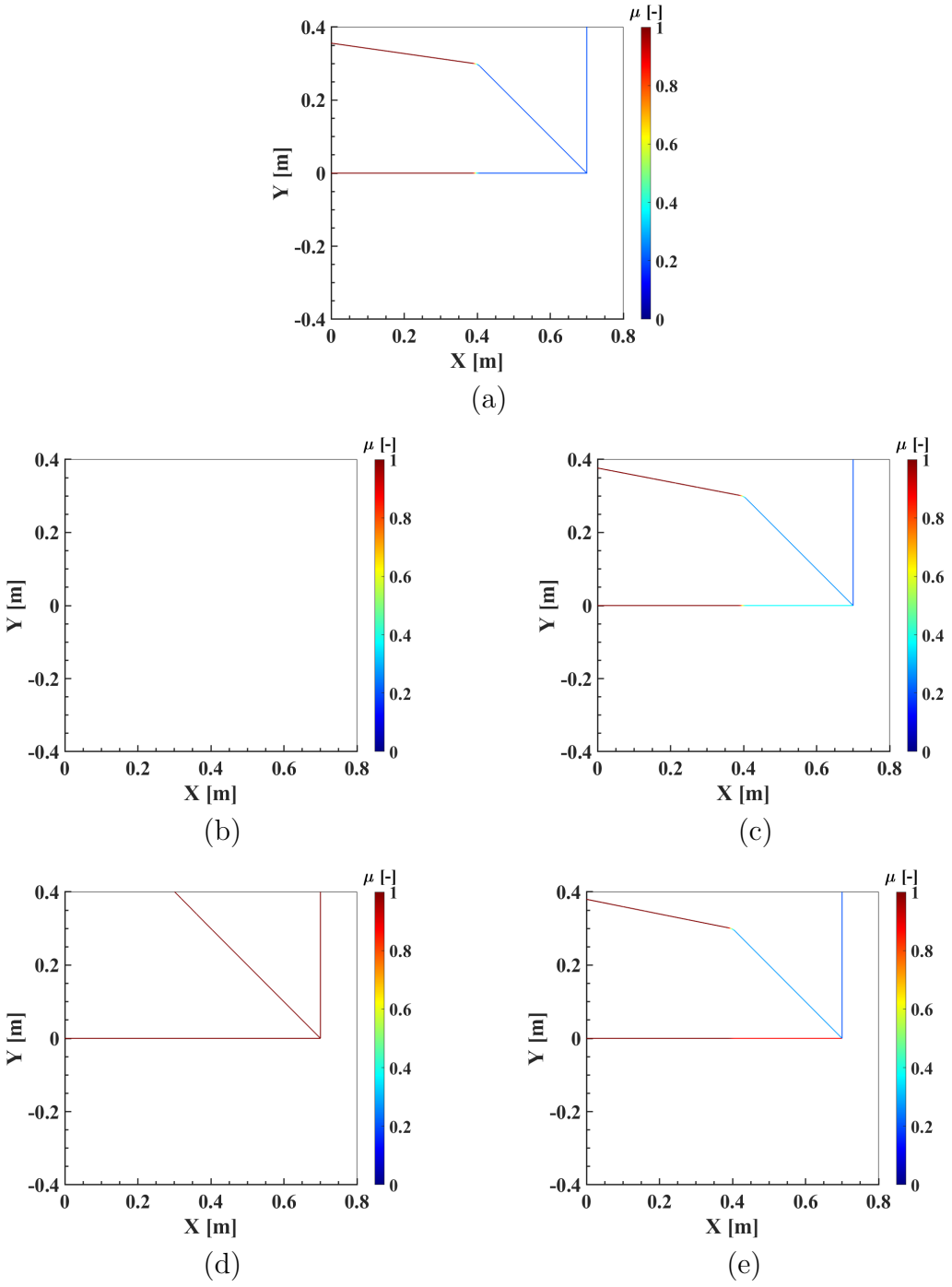

Figure 6.5: Ray tracing analysis for a changing electron number density in the domain (a) with an applied magnetic field in negative X direction of 0.01 T (b, c), and 0.25 T (d, e) for a propagation parallel, perpendicular and 45 degree to the magnetic field vector. The non-magnetized refractive index is 1 for X $<$ 0.4 m and 0.2 for X $>$ 0.4 m.

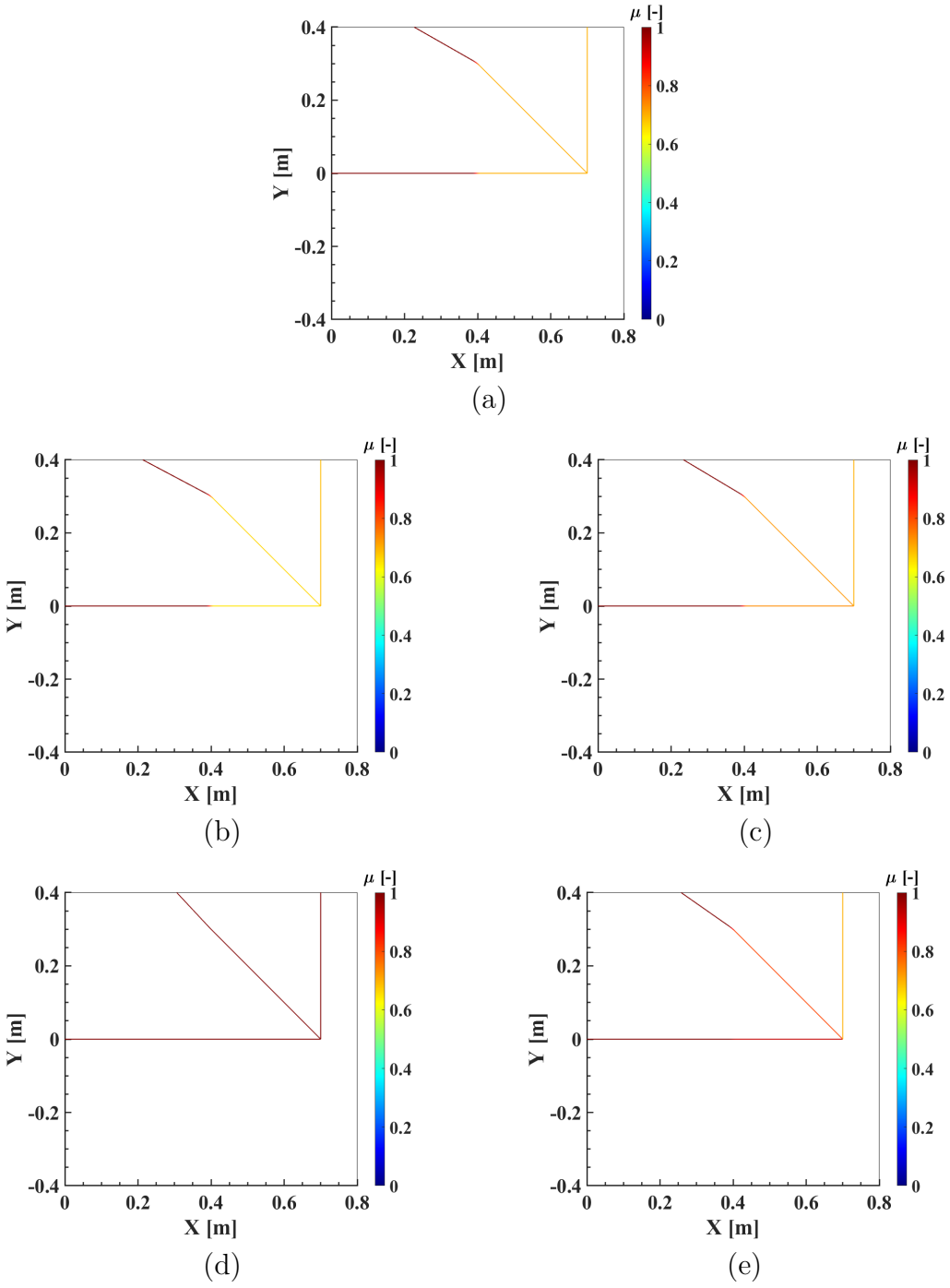

Figure 6.6: Ray tracing analysis for a changing electron number density in the domain (a) with an applied magnetic field in negative X direction of 0.01 T (b, c), and 0.25 T (d, e) for a propagation parallel, perpendicular and 45 degree to the magnetic field vector. The non-magnetized refractive index is 1 for X $<$ 0.4 m and 0.7 for X $>$ 0.4 m.

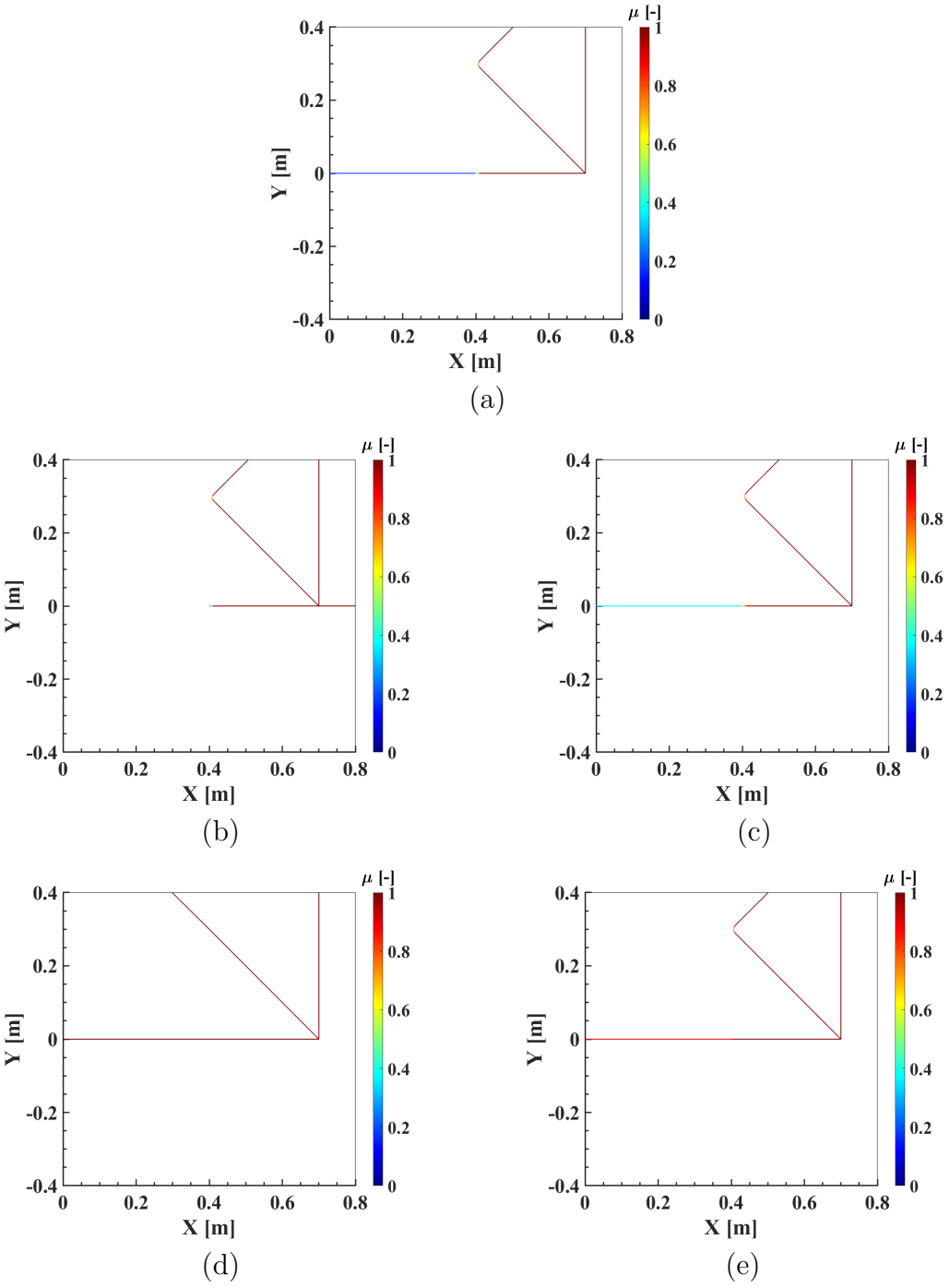

Figure 6.7: Ray tracing analysis for a changing electron number density in the domain (a) with an applied magnetic field in negative X direction of 0.01 T (b, c), and 0.25 T (d, e) for a propagation parallel, perpendicular and 45 degree to the magnetic field vector. The non-magnetized refractive index is 0.2 for X $<$ 0.4 m and 1 for X $>$ 0.4 m.

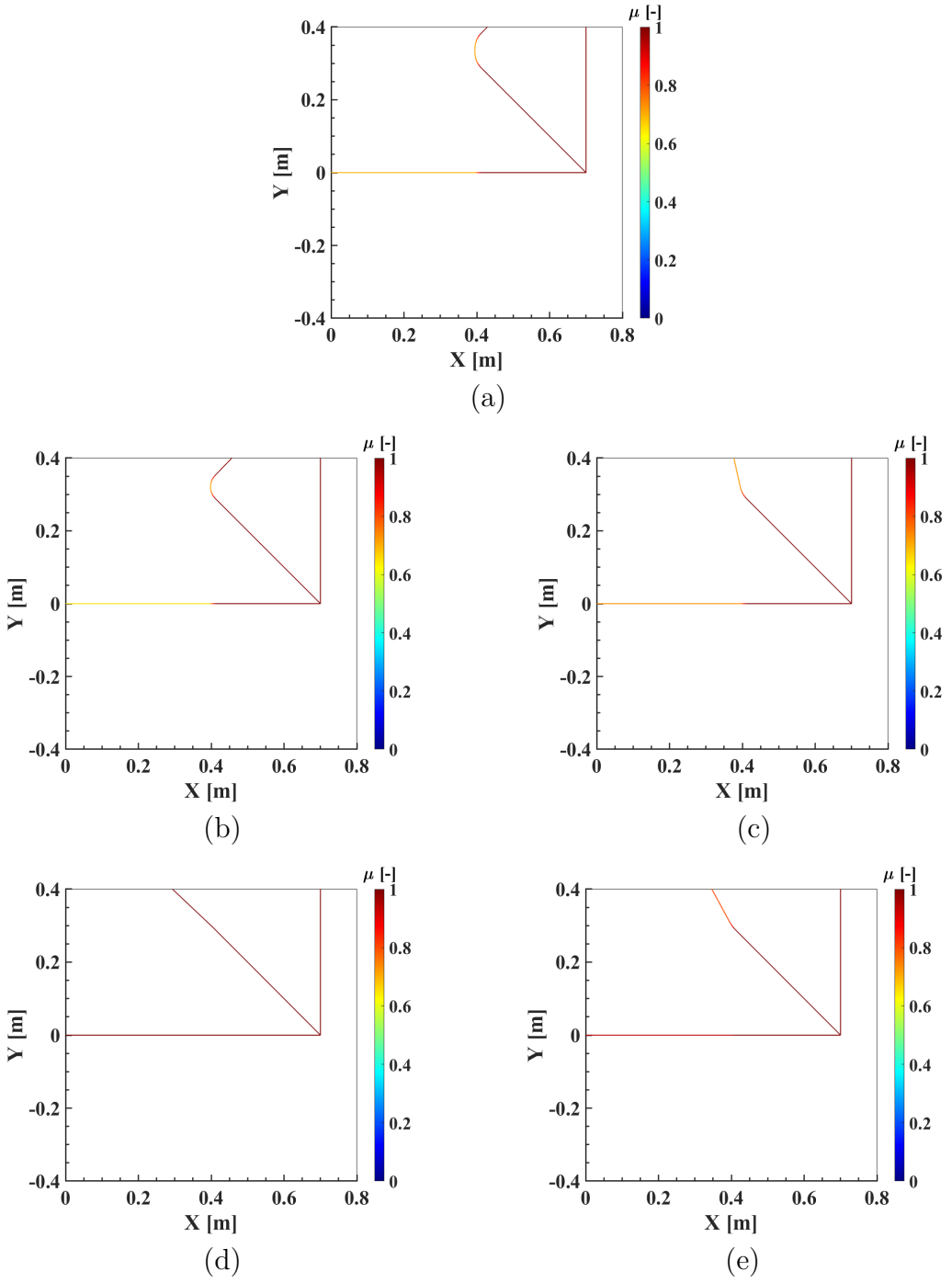

Figure 6.8: Ray tracing analysis for a changing electron number density in the domain (a) with an applied magnetic field in negative X direction of 0.01 T (b, c), and 0.25 T (d, e) for a propagation parallel, perpendicular and 45 degree to the magnetic field vector. The non-magnetized refractive index is 0.7 for X $<$ 0.4 m and 1 for X $>$ 0.4 m.

6.2.2 Validation with on-ground experiments

The following section outlines the principal elements of the communication blackout experiment carried out at VKI. A comprehensive description of this endeavor is available in Deliverable 2.5: "Radio blackout experiments with magnet" [74].

6.2.2.1 Plasma Wind Tunnel (PWT) facility at VKI: Plasmatron

The Plasmatron at VKI functions as an inductively coupled plasma (ICP) wind tunnel, as detailed in Bottin et al. [75, 76], generating a highly dissociated, high enthalpy subsonic gas flow. This setup mimics the aerothermodynamic conditions observed behind shockwaves in hypersonic flight regimes. The facility features a quartz tube with a 200 mm internal diameter and 5 mm thickness, surrounded by a coil connected to a 1.2 MW generator providing high voltage and high-frequency current (2 kV, 400 kHz). This induces an electromagnetic (EM) field within the tube, generating eddy currents from residual charged particles in the flow, which heat the gas through the Joule effect. Gas injection occurs through an annular inlet upstream of the coil. Ionization of the gas due to the EM field results in a plasma plume, 16 cm in diameter, exiting the torch into a 1.4 m diameter vacuum chamber.

The plasma then passes through a diffuser and is cooled by a water-cooled heat exchanger. After proper dilution, the recombined gases are released to the atmosphere through an exhaust system. The vacuum system includes three pumps, and additional systems manage gas circulation, cooling, and diagnostics. The electric power (P_{el}) supplied to the induction coil is monitored and recorded by the Plasmatron control system. Up to three probes can be remotely inserted and retracted from the plasma jet for diagnostics purposes.

6.2.2.2 Communication setup

The Ka-band communication setup comprises four sets, each including a conical horn antenna with circular waveguide, linear polarization, and 15 dBi gain (MI-wave 262A-15/0.250), a mode transition (MI-wave 284-0.250), and a waveguide to coax adapter (MI-wave 411A). Each set is connected to a flexible microwave cable (Huber-Suhner SUCOFLEX 102) and a DC block (MI-wave 8141A). The transmitting antenna uses a 6 m cable, while each receiving antenna is connected with a 5 m cable. Signal transmission and reception are facilitated by a vector network analyzer (VNA, Rohde and Schwarz ZNB40), allowing frequency sweeps from 33 to 40 GHz.

This chosen communication system is deemed suitable given the design constraints imposed by the probe equipped with the HTS-magnet, which include:

- Testing under conditions where the system faces a stagnating flow,
- Ensuring the emitting antenna diameter does not exceed 25 mm to fit into the HTS-magnet bore-hole,
- Maximizing the directive radiation pattern of the antenna,
- Positioning the receiver antennas to point towards the emitter antenna but at a distance from the axis of the plasma jet.

While plasma frequencies based on measured electron densities at 300 mm from the torch exit typically remain above the Ka-band, testing scenarios where the plasma is neither fully transparent nor fully opaque to the radio signal are preferred for blackout mitigation analysis. Testing within this range allows evaluation of any signal enhancement due to the applied magnetic field. Thus, the Ka-band is chosen due to its flexibility in tuning Plasmatron power and pressure settings, as well as the

varying electron concentration gradients in the plasma jet. While 40 GHz might be lower than ideal for high-power conditions, it can adequately cover the outer and cooler layers of the plasma jet closer to the receiving antennas.

6.2.2.3 Stagnation probe for MEESST experiments

The impact of an applied magnetic field on signal propagation is investigated using a specialized plasma probe called the `MHD` probe, developed within the MEESST consortium by Absolut System. This probe is designed to accommodate a high-temperature superconducting (HTS) magnet developed by the Karlsruhe Institute of Technology (KIT), featuring a coil constructed as a stack of five pancakes using a total length of 900 m of 70 μm thick REBCO tape from Theva D"uennschichttechnik GMBH. Details regarding the design, manufacturing, and testing of the magnet can be found in technical notes [77] and [78].

Absolut System also designed and assembled the cryogenic system responsible for cooling the magnet. This system includes two heat exchangers: one located at the coldhead and another at the rear of the HTS magnet. The coldhead utilizes a Cryomech AL325 combined with a Cryomech CPA1110 compressor. A cryofan from Absolut System circulates the cryogenic fluid through a 5-meter cryoline to the probe. In the cryogenic circulation loop, gaseous helium flows through both heat exchangers. The helium is cooled at the coldhead heat exchanger and absorbs the thermal load near the magnet's cold plate.

The magnet is supplied with current from an Agilent 6671A current source, and the voltages across the magnet and shunt are monitored using a data acquisition system (Agilent 34970A) connected to a nanovoltmeter (Keysight 34420A). Temperature monitoring of the magnet and current leads is handled by a temperature monitor (Lake Shore LS218). The rack's primary power supply operates at 400 V, 16 A, while other electronic devices within the rack are powered by 230 V AC.

The magnetic field at the front of the quartz head is monitored using a Hall probe. The maximum magnetic field strengths recorded for the applied currents are detailed in Table 6.1.

Table 6.1: Maximum magnetic field strength measured for applied current.

Current [A]	Magnetic field strength [T]
0	0
10	0.092
20	0.170
30	0.250
40	0.340
50	0.410

6.2.2.4 Experimental setup and operating conditions

Defining the xx direction as perpendicular to the plane of the torch exit, positive towards the interior of the chamber, and the yy and zz axes as horizontal and vertical within the plane of the torch exit wall, respectively, the coordinates of the antenna centers are positioned as follows (distances in mm, with the origin depicted in Fig.

6.9):

$$\begin{aligned} &\text{Antenna 1: } (x_1, y_1, z_1) = (445, 0, 0) \text{ mm}, \\ &\text{Antenna 2: } (x_2, y_2, z_2) = (22, 150, 165) \text{ mm}, \\ &\text{Antenna 3: } (x_3, y_3, z_3) = (25, -155, 135) \text{ mm}, \\ &\text{Antenna 4: } (x_4, y_4, z_4) = (25, -295, 330) \text{ mm}. \end{aligned} \tag{6.6}$$

These distances are 478.18 mm between Antenna 1 and Antenna 2, 467.60 mm between Antenna 1 and Antenna 3, and 610.18 mm between Antenna 1 and Antenna 4. This corresponds to solid angles of $\alpha_{12} = 19.53°$, $\alpha_{13} = 20.26°$, and $\alpha_{14} = 35.08°$. A schematic of the setup is shown in Fig. 6.9 (a), and a photograph taken during the test can be seen in Fig. 6.9 (b).

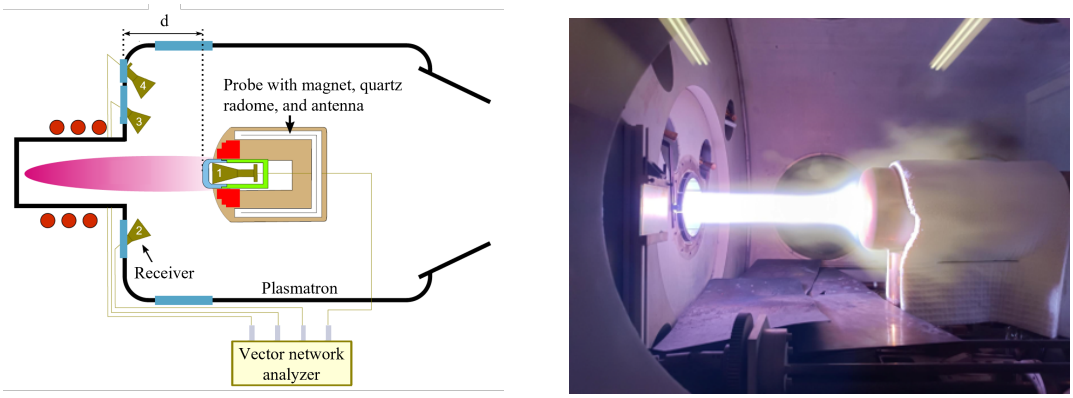

(a) (b)

Figure 6.9: A schematic of the experimental setup with the MHD probe (a), and a picture of the MHD probe under testing in an air plasma (b).

The following operating conditions are analyzed:

1. Plasmatron effective input powers: 0 kW, 125 kW, 150 kW, 175 kW, and 200 kW
2. Radio frequencies: 34 GHz, 37 GHz, and 40 GHz
3. Maximum magnetic field strengths: 0 T, 0.25 T, 0.41 T, and 1 T

6.2.2.5 Numerical domain and magnetic field

The numerical domain for the validation with the on-ground experiments is shown in Fig. 6.10 (a). This domain is a simplified geometry of the Plasmatron at VKI with a diameter of 1.4 m. The geometry of the probe is highlighted in green. The transmitting antenna is placed at the tip of the probe radiating with a radiation aperture of 180° towards minus X direction as illustrated with the red dotted half circle. The plasma stream comes from the left, flowing around the probe and leaving the domain on the right side. The three receiving antenna positions are marked in red as well. Since the analyzed cases are axis symmetrical the numerical results are presented with the half of the domain (Y greater zero or Y smaller zero). The radiation pattern of the transmitting antenna with a quartz radome is shown in Fig. 6.10 (b). The 180° radiation aperture is marked with a red dotted half circle.

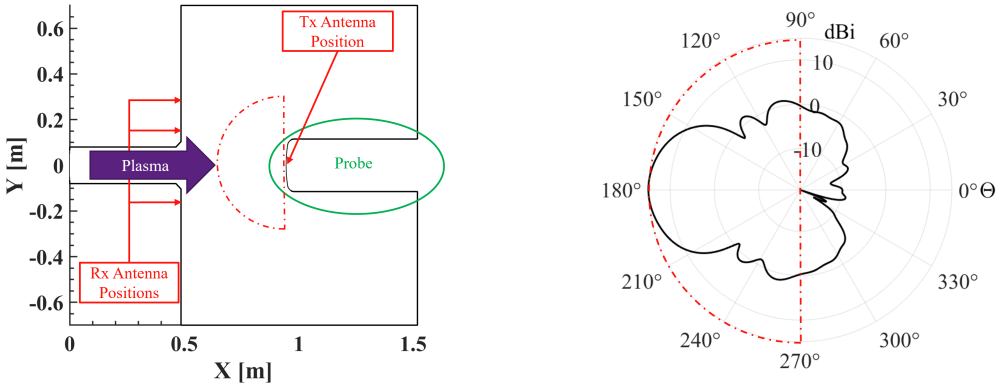

(a) (b)

Figure 6.10: Schematic of the full numerical flow domain (a), and the antenna radiation pattern of the transmitting antenna with quartz radome (b).

The magnitude of the magnetic field strength for the three analyzed cases with a maximum of 0.25 T, 0.41T, and 1 T are displayed in Fig. 6.11. Sub-figures (a), (c), and (e) show the magnetic field strengths with a limit of 1 T. Sub-figures (b), (d), and (f) show the magnetic field strengths with a limit of 0.25 T. Those two styles were chosen to provide a better understanding of the range of the applied magnetic fields. The sub-figures on the left side of Fig. 6.11 indicate, that the magnetic fields of 0.25 T and 0.41 T are negligible compared to the 1 T case. However, if the maximum magnetic field strength displayed is limited to 0.25 T, as shown in the sub-figures on the right side of Fig. 6.11, the magnetic field is visible in a significant area around the probe for the 0.25 T case. Previous analysis with a small magnetic field strength of 0.05T or less showed an impact on the ray propagation path (see Chapter 4). The previous analysis of the effect of an applied magnetic field on the refractive index (see Fig. 6.3) leads to the assumption that the area in which the ray path is less affected or in some conditions unaffected by the plasma is greater for larger magnetic fields.

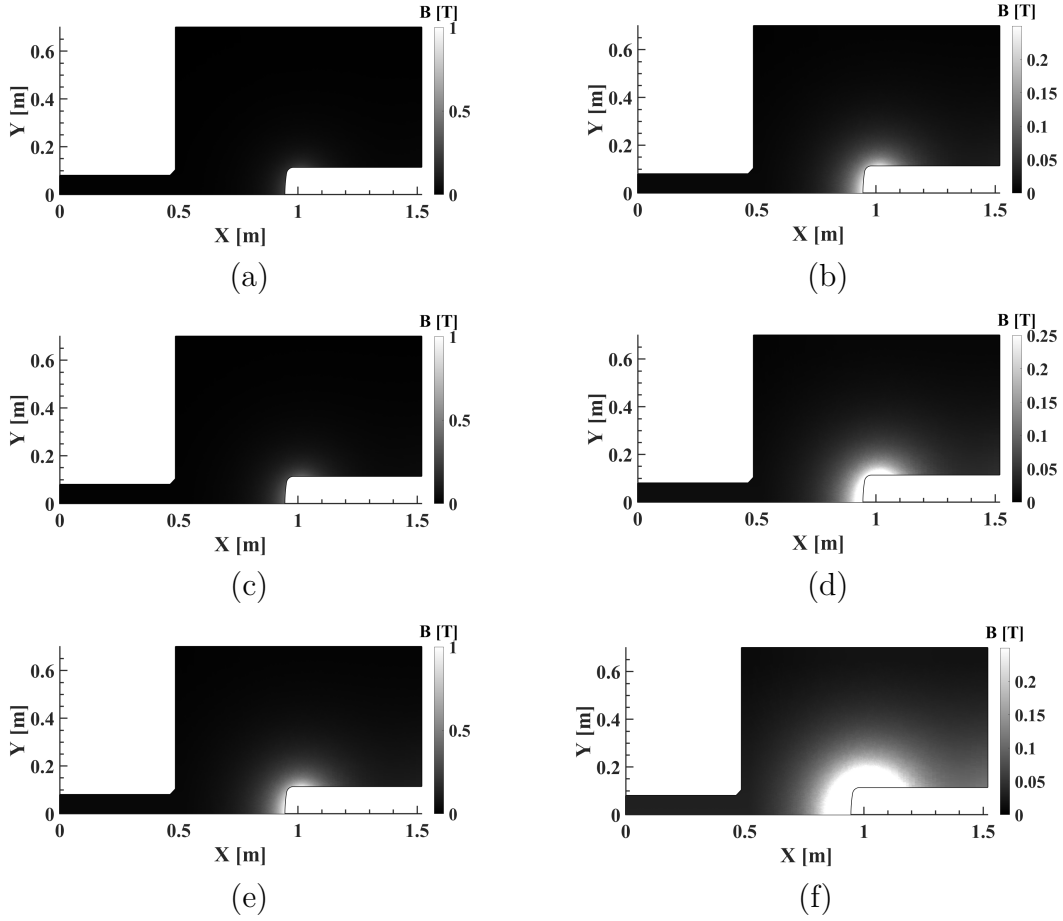

Figure 6.11: The magnitude of the magnetic field strength for cases with a maximum of (a) 0.25 T, (c) 0.41 T, (e) 1 T limited to 1 T, and for better visualization the magnetic field is limited to a value of 0.25 T for (b) 0.25 T, (d) 0.41 T, and (f) 1 T.

6.2.2.6 MHD effect on electron number density

The electron number densities in the flow domain for various magnetic field strengths for the case with a Plasmatron input power of 200 kW at a radio frequency of 34 GHz are shown in Fig/ 6.12. These operating conditions are chosen to be displayed here since the electron number density is highest at the maximum power level in combination with the lowest frequency and shall show the effect of a magnetic field on the electron number density. It can be seen that the electron number density field does not significantly change when a magnetic field with a maximum magnetic field strength of 0.25 T (b), or 0.41 T (c) is applied compared to an non-magnetic case (a). The distance between the probe and the area in which the critical electron number density is reached is increased for the case with a maximum magnetic field strength of 1 T (d). The plasma stream is thickened close to the probe in the case of 1 T.

This leads to the conclusion that the established Lorentz force due to the presence of the magnetic field is negligible for the cases of 0.25 T, and 0.41 T but significant for the case of 1 T.

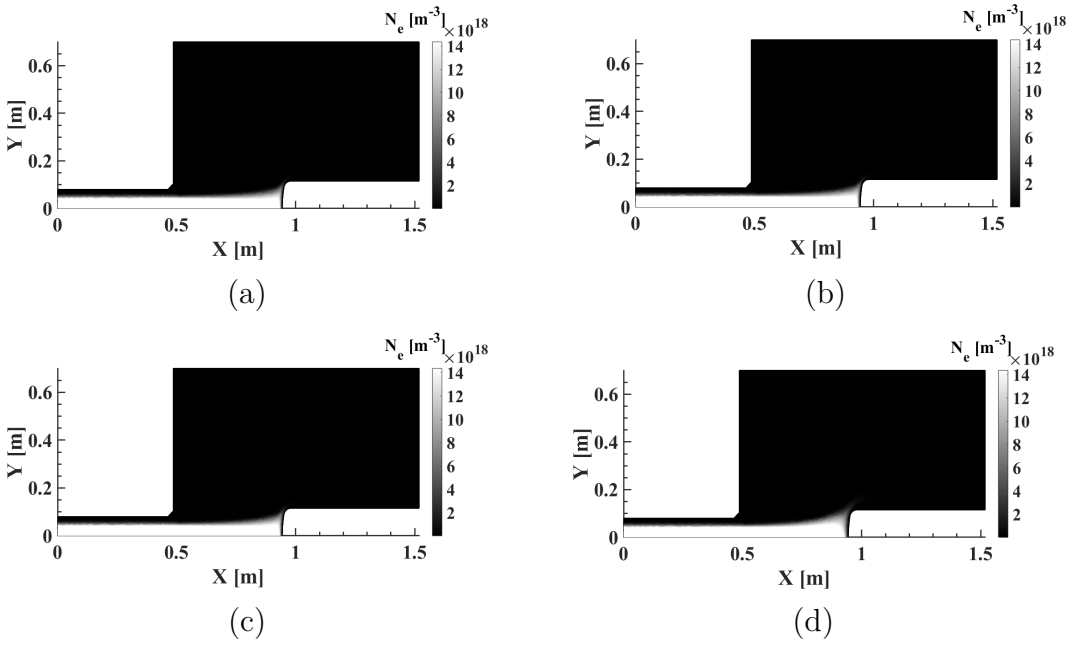

Figure 6.12: The electron number density in the flow domain for a Plasmatron input power of 200 kW at a radio frequency of 34 GHz for (a) 0 T, (b) 0.25 T, (c) 0.41T, and (d) 1 T limited to the corresponding critical electron number density.

Increasing the radio frequency is more effective in increasing the distance of the area with overcritical electron number density to the surface of the probe according to Fig. 6.13 when comparing with the effect of the magnetic field on the electron number density field.

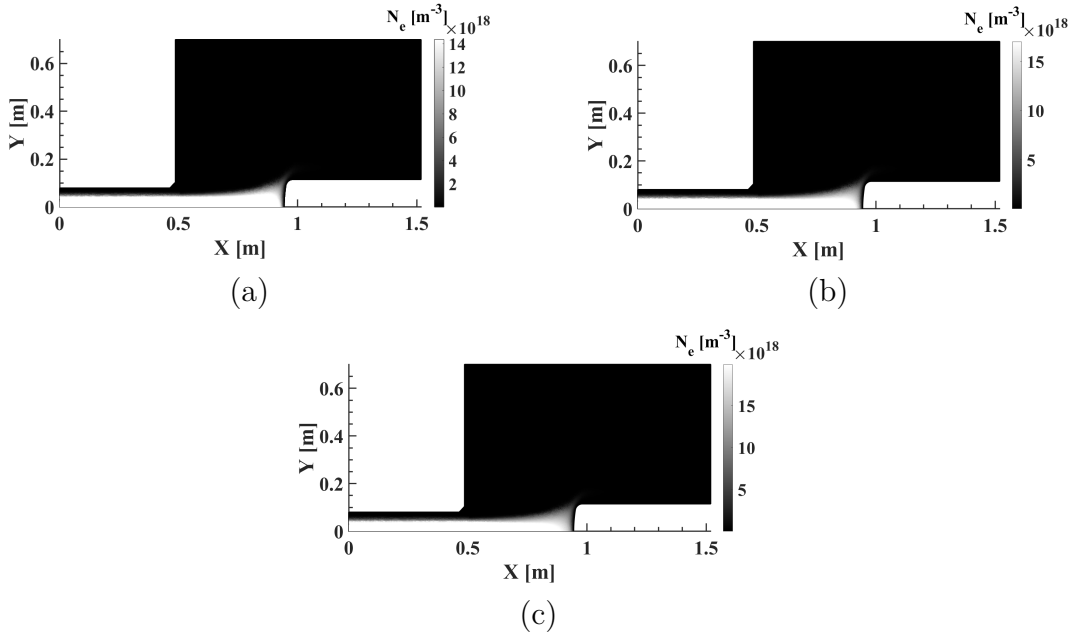

Figure 6.13: The electron number density in the flow domain for a Plasmatron input power of 200 kW at radio frequencies of (a) 34 GHz, (b) 37 GHz, and (c) 40 GHz limited to the corresponding critical electron number density.

6.2.2.7 Ray tracing analysis

In the following the ray-tracing analyses are presented. All ray-tracing solutions are performed with a maximum number of three specular wall reflections. The ray density was chosen to be 0.5 rays per degree for better visualization.

Firstly, the ray-tracing solutions without plasma and magnetic field are analyzed for various radio frequencies (see Fig. 6.14. Since no plasma is present, the ray-tracing solutions result in straight lines with a constant refractive index of one. The displayed ray tracing solutions are identical for all three frequencies.

In a second step, the non-MHD plasma cases are analyzed. In Fig. 6.15 the ray-tracing solutions for efficient input powers of (a) 125 kW, (b) 150 kW, (c) 175 kW, and (d) 200 kW are shown. At 125 kW the rays are bent the least as expected due to the least electron number density compared to the other three power levels. However, only reflected rays are getting close to the antenna positions. Increasing the power levels leads to larger electron number densities and therefore higher refractive index gradients closer to the transmitting antenna position. Since the number of reflections are limited to three the amount of rays leaving the domain is reduced as well. This can be observed especially at power levels of 175 kW and 200 kW. Eight rays out of 45 are able to leave the domain at a power of 200 kW.

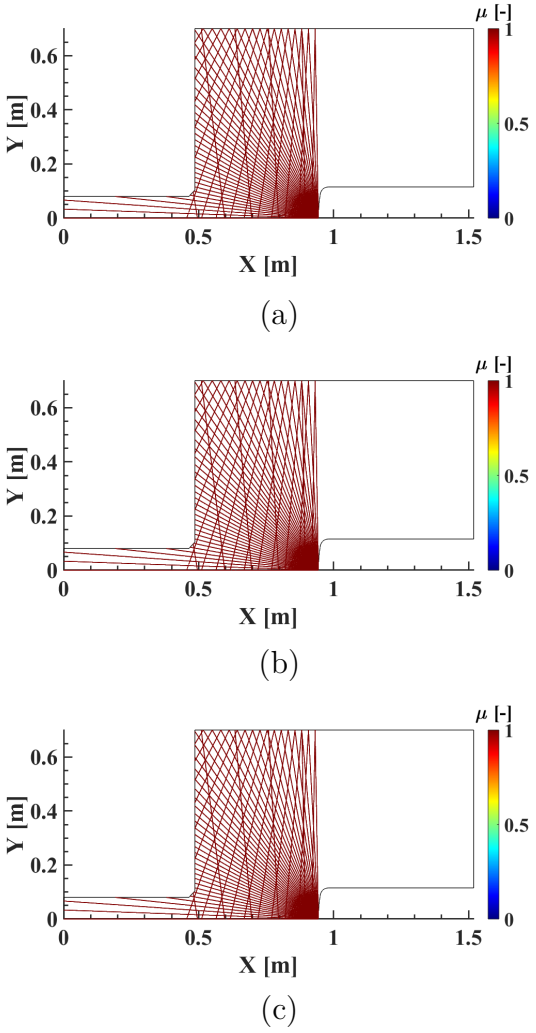

Figure 6.14: Ray-tracing solutions for non-plasma, non-MHD cases at radio frequencies of (a) 34 GHz, (b) 37 GHz, and (c) 40 GHz.

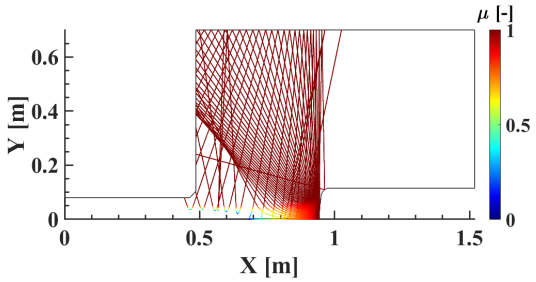

(a)

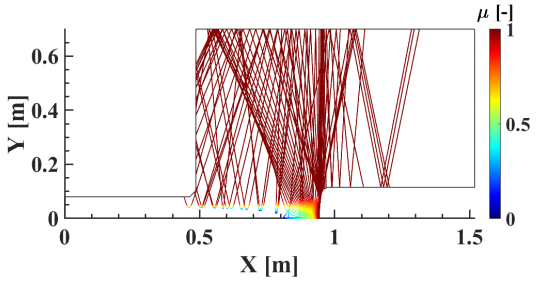

(b)

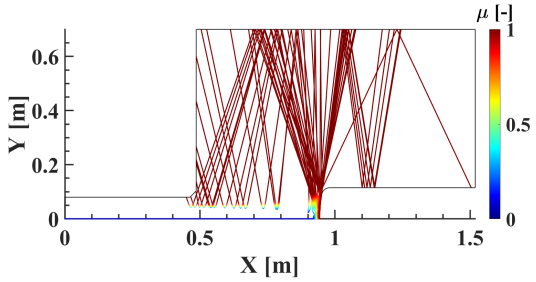

(c)

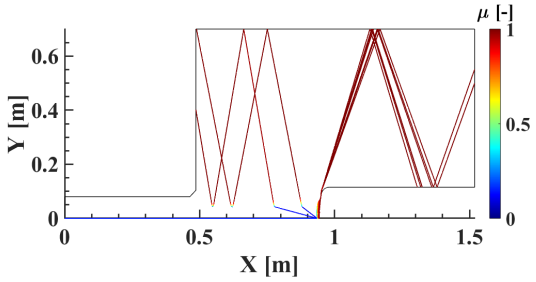

(d)

Figure 6.15: Ray-tracing solutions for non-MHD plasma cases at a radio frequency of 34 GHz at 125 kW, (b) 150 kW, (c) 175 kW, and (d) 200 kW effective input power.

In the following, the MHD ray-tracing solutions are discussed. It is of interest how the ray-tracing solution is affected by an applied magnetic field. In Figures 6.16 to 6.27 the top ray-tracing solution represents the full MHD effect including the recalculation of the refractive index after each step. The Figures on the bottom (b) are the ray-tracing solutions of the MHD flow field neglecting MHD effects in the ray path calculation meaning no refractive index recalculation and no consideration of the magnetic field in the initial refractive index calculation (see Eq. 2.17). Additionally, only cases at 34 GHz are analyzed here due to the higher plasma effect at smaller radio frequencies. This was chosen to keep a decent figure-to-text ratio. A similar behavior can be seen for higher frequencies and therefore no information is missing. Lastly, the MHD ray-tracing solutions contain the ray-tracing solution of the ordinary and extraordinary ray paths leading to the double number of rays per figure.

The ray-tracing solution of a case with 0.25 T at 125 kW is analyzed in Fig. 6.16. Comparing the ray-tracing solution with the neglected MHD effect in the ray path calculation shows no significant differences to the non-MHD ray-tracing solution in Fig. 6.15 (a). This is expected since the electron number density field has not noticeably changed at a magnetic field strength of 0.25 T. However, the full MHD ray-tracing analysis considering MHD effects on the ray path calculation shows a higher ray density close to the receiving antenna position. It is noticeable that rays reaching the receiving (Rx) antenna positions are reaching the Rx antenna from a larger angle away from the antenna bore-sight since only reflected rays reach the Rx antenna areas.

The full MHD ray-tracing solution at 0.25 T and a power of 150 kW shows that the ray paths are more bent away from the Rx antenna positions compared to the ray-tracing solution at 0.25 T and a power of 125 kW and the non-MHD case (see Fig. 6.17). More rays are reaching the area upstream on the opposite of the Rx antenna positions. Neglecting the MHD effects in the ray-tracing solutions shows a similar ray-tracing solution as for the non-MHD case.

If neglecting the MHD effects on the ray-tracing solutions at 0.25 T with an input power of 175 kW and 200 kW (see Figures 6.18 (b), and 6.19 (b)) does not change the ray-tracing solution compared to the non-MHD ray-tracing solution. However, considering the MHD effects on the ray-tracing path significantly changes the ray-tracing solution (see Figures 6.18 (a), and 6.19 (a)). At 175 kW the rays are less bent leading to an increased aperture angle. The highest concentration of rays is still in a small cone towards the radial direction. The most significant effect of the magnetic field can be observed at 200 kW. The extraordinary rays are contributing to an increased number of rays reaching the Rx antenna area. The ordinary rays are reflected several times after leaving the transmitting antenna, leading to a small amount of rays leaving the domain upstream.

Analyzing the ray-tracing solutions for a magnetic field strength of 0.41 T, neglecting the MHD effects on the ray path calculation, gives similar solutions compared to the non-MHD ray-tracing results as can be seen in Figures 6.20 (b), 6.21 (b),6.22 (b), and 6.23 (b). The electron number density does not change significantly if a magnetic field of 0.41 T is applied.

However, considering the MHD effects in the ray path calculation the rays are less bent compared to non-MHD cases and cases with an applied magnetic field of 0.25 T. Rays reaching the Rx antenna areas are reflected several times and reach the Rx antenna area with an angle away from the antenna bore-sight (see Figures 6.20 (a),

6.21 (a),6.22 (a), and 6.23 (a)). Again, the main contribution to the rays reaching the Rx antenna positions at high power levels is because of the extraordinary rays.

In case a magnetic field of 1 T is applied, the flow field is altered leading to a significant change in the ray path calculation when neglecting MHD effects in the ray-tracing calculation (see Figures 6.24 (b), 6.25 (b),6.26 (b), and 6.27 (b)). Nevertheless, it is unlikely that rays will reach the Rx antenna positions at 200 kW.

Considering the MHD effects in the ray tracing calculation shows an increased number of rays reaching the Rx antenna positions for all four power levels (see Figures 6.24 (a), 6.25 (a),6.26 (a), and 6.27 (a)) as well as an increase of number of rays leaving the domain. Ordinary rays are not reaching the Rx antenna areas at 200 kW.

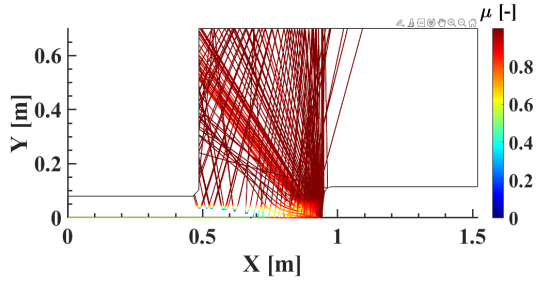

(a)

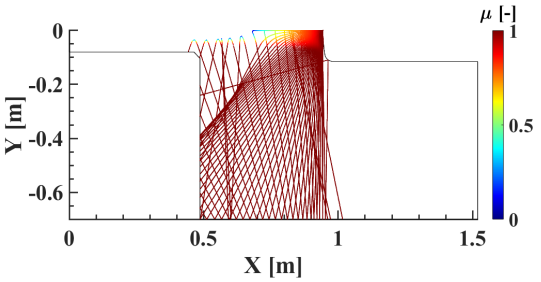

(b)

Figure 6.16: Ray-tracing solutions for an MHD plasma case with an applied magnetic field of 0.25 T at an effective power of 125 kW, and a radio frequency of 34 GHz considering the magnetic field in the ray tracing calculation (a), and neglecting the magnetic field in the ray tracing calculation (b).

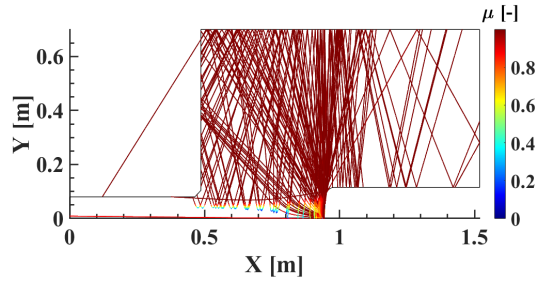

(a)

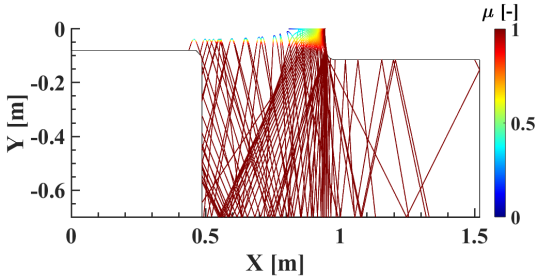

(b)

Figure 6.17: Ray-tracing solutions for an MHD plasma case with an applied magnetic field of 0.25 T at an effective power of 150 kW, and a radio frequency of 34 GHz considering the magnetic field in the ray tracing calculation (a), and neglecting the magnetic field in the ray tracing calculation (b).

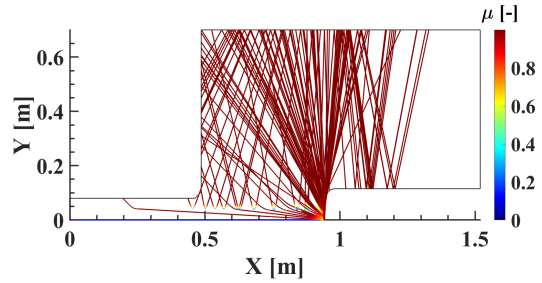

(a)

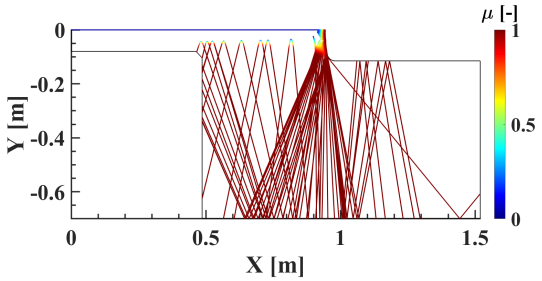

(b)

Figure 6.18: Ray-tracing solutions for an MHD plasma case with an applied magnetic field of 0.25 T at an effective power of 175 kW, and a radio frequency of 34 GHz considering the magnetic field in the ray tracing calculation (a), and neglecting the magnetic field in the ray tracing calculation (b).

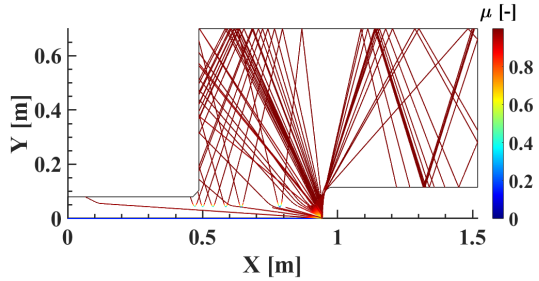

(a)

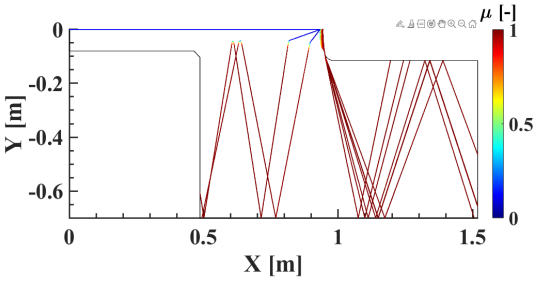

(b)

Figure 6.19: Ray-tracing solutions for an MHD plasma case with an applied magnetic field of 0.25 T at an effective power of 200 kW, and a radio frequency of 34 GHz considering the magnetic field in the ray tracing calculation (a), and neglecting the magnetic field in the ray tracing calculation (b).

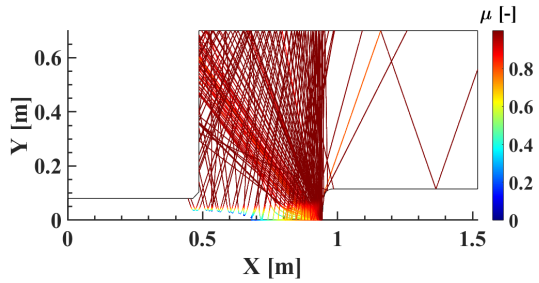

(a)

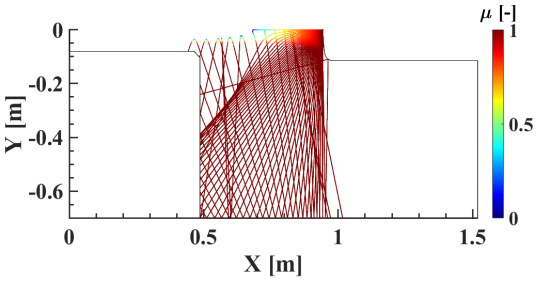

(b)

Figure 6.20: Ray-tracing solutions for an MHD plasma case with an applied magnetic field of 0.41 T at an effective power of 125 kW, and a radio frequency of 34 GHz considering the magnetic field in the ray tracing calculation (a), and neglecting the magnetic field in the ray tracing calculation (b).

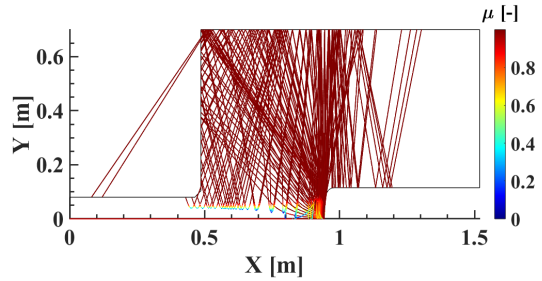

(a)

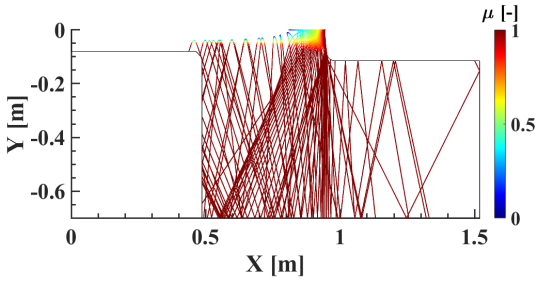

(b)

Figure 6.21: Ray-tracing solutions for an MHD plasma case with an applied magnetic field of 0.41 T at an effective power of 150 kW, and a radio frequency of 34 GHz considering the magnetic field in the ray tracing calculation (a), and neglecting the magnetic field in the ray tracing calculation (b).

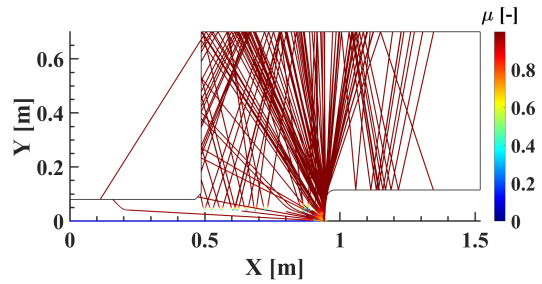

(a)

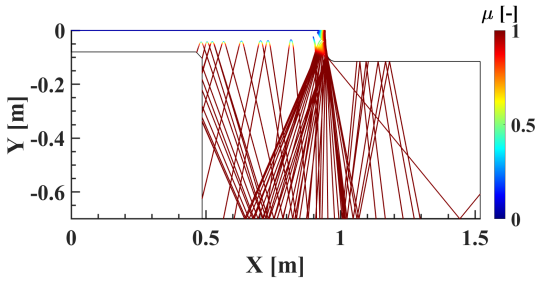

(b)

Figure 6.22: Ray-tracing solutions for an MHD plasma case with an applied magnetic field of 0.41 T at an effective power of 175 kW, and a radio frequency of 34 GHz considering the magnetic field in the ray tracing calculation (a), and neglecting the magnetic field in the ray tracing calculation (b).

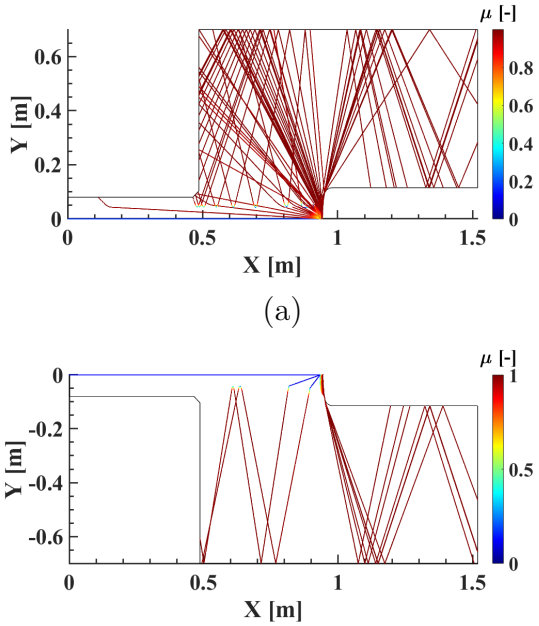

(a)

(b)

Figure 6.23: Ray-tracing solutions for an MHD plasma case with an applied magnetic field of 0.41 T at an effective power of 200 kW, and a radio frequency of 34 GHz considering the magnetic field in the ray tracing calculation (a), and neglecting the magnetic field in the ray tracing calculation (b).

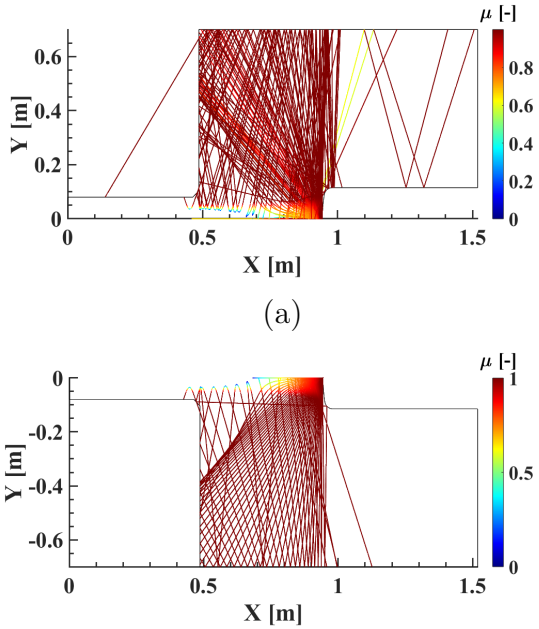

(a)

(b)

Figure 6.24: Ray-tracing solutions for an MHD plasma case with an applied magnetic field of 1 T at an effective power of 125 kW, and a radio frequency of 34 GHz considering the magnetic field in the ray tracing calculation (a), and neglecting the magnetic field in the ray tracing calculation (b).

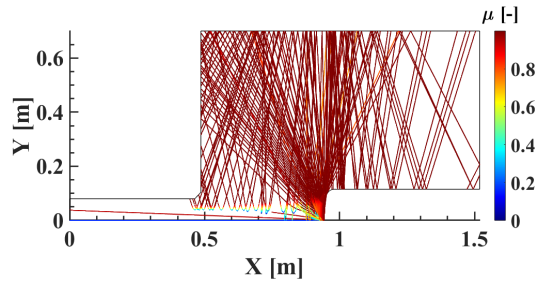

(a)

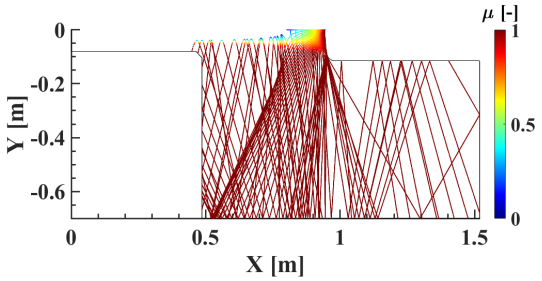

(b)

Figure 6.25: Ray-tracing solutions for an MHD plasma case with an applied magnetic field of 1 T at an effective power of 150 kW, and a radio frequency of 34 GHz considering the magnetic field in the ray tracing calculation (a), and neglecting the magnetic field in the ray tracing calculation (b).

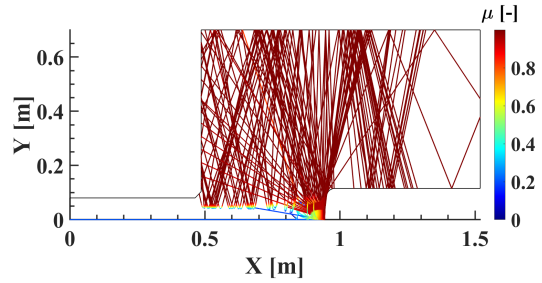

(a)

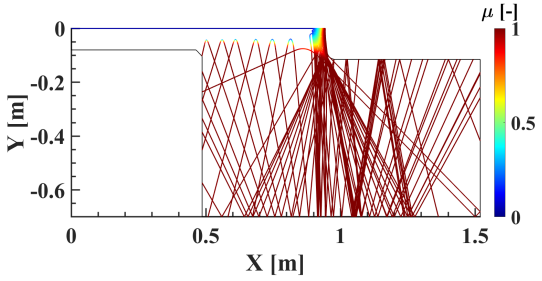

(b)

Figure 6.26: Ray-tracing solutions for an MHD plasma case with an applied magnetic field of 1 T at an effective power of 175 kW, and a radio frequency of 34 GHz considering the magnetic field in the ray tracing calculation (a), and neglecting the magnetic field in the ray tracing calculation (b).

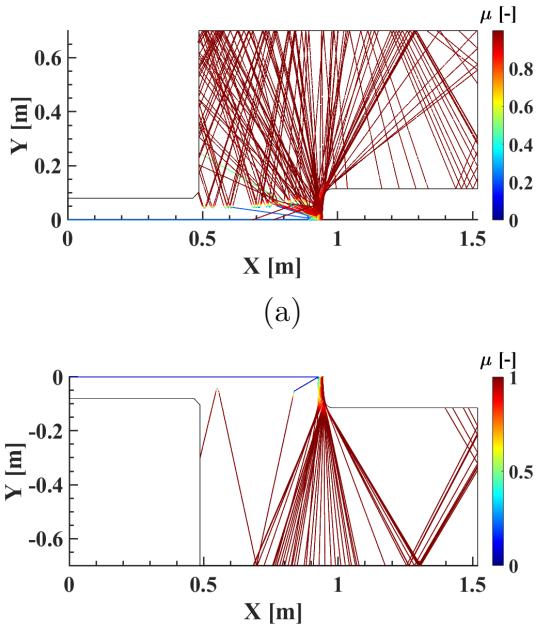

Figure 6.27: Ray-tracing solutions for an MHD plasma case with an applied magnetic field of 1 T at an effective power of 200 kW, and a radio frequency of 34 GHz considering the magnetic field in the ray tracing calculation (a), and neglecting the magnetic field in the ray tracing calculation (b).

6.2.2.8 EM wave intensity analysis

The analysis of the intensity of the electromagnetic waves along the ray trajectory is discussed in the following section. The intensities are normalized to the maximum intensity value of all rays launched. The minimum intensity is limited to -400 dB for better comparison. The electric field and therefore intensity values along the trajectory depend highly on the spread factor of a ray. This leads to intensity increases along the ray path in case rays are bent towards each other. Since the spread factor is related to the behavior of the adjacent ray numerical uncertainties may arise.

The results of the intensity analysis for non-plasma, and non-MHD cases at 34 GHz, 37 GHz, and 40 GHz are shown in Fig. 6.28. The intensities are decreasing with increasing distance from the transmitting antenna. The loss in intensity is significant after the wall reflection in those cases. Rays reach the Rx antenna area mostly in the bore-sight direction with a contribution of the reflected rays.

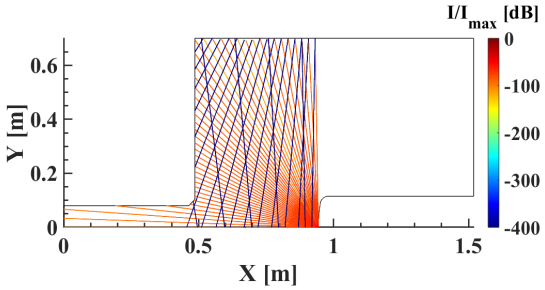

(a)

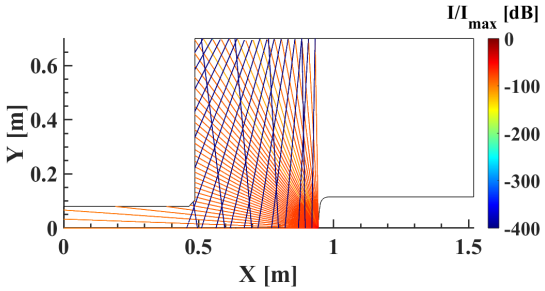

(b)

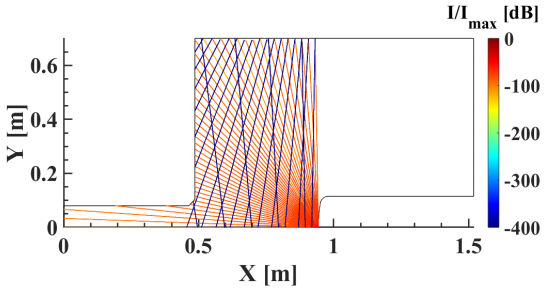

(c)

Figure 6.28: Normalized intensity for non-plasma, non-MHD cases at radio frequencies of (a) 34 GHz, (b) 37 GHz, and (c) 40 GHz.

In Fig. 6.29 the cases without a magnetic field applied are shown. At an input power level of 125 kW the intensities of the rays reaching the Rx antenna area are low. This is also related to the losses during the reflection process. From 125 kW to 175 kW, the intensity of the rays reaching the Rx antenna area seems to increase and the losses during the reflection process seem to decrease. The losses during the reflection processes seem to be higher for high-energy rays. Interestingly, the high-energetic rays launched in the bore-sight of the transmitting antenna are reflected from the plasma stream at 175 kW and leave the domain upstream. This indicates a separation of the low energetic waves traveling downstream less affected by the plasma close to the transmitting antenna. Similar behavior can be observed for the 200 kW case although most rays do not leave the domain due to the limited amount of reflections allowed. This is an example of why limiting the number of reflections to three does not significantly affect the possible received power at a receiving antenna due to the high losses during the reflection process.

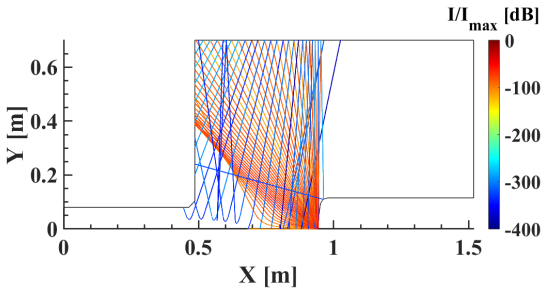

(a)

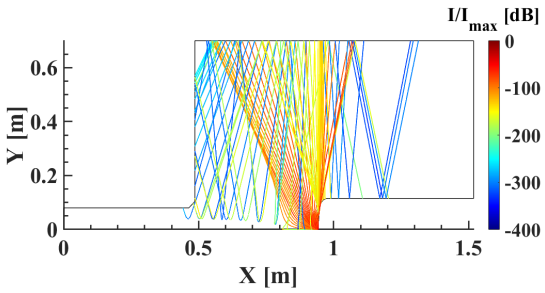

(b)

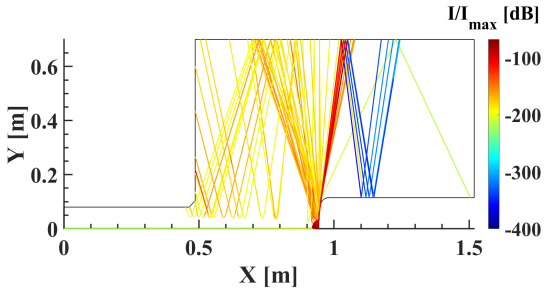

(c)

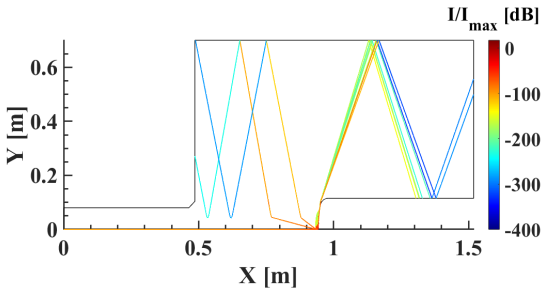

(d)

Figure 6.29: Normalized intensity for non-MHD plasma cases at a radio frequency of 34 GHz at 125 kW, (b) 150 kW, (c) 175 kW, and (d) 200 kW effective input power.

Although the ray-tracing solutions are not significantly altered if neglecting the MHD effects on the ray path calculation the intensities can be altered noticeably.

In the case with an input power of 125 kW with an applied magnetic field of 0.25 T the intensity along the ray trajectory is not changing compared to the non-MHD case as can be seen in Fig. 6.30 (b). Further increasing the input power to 150 kW and 175 kW seems to result in a higher intensity loss (Fig. 6.31 (b), and 6.32 (b)). At a power level of 200 kW (Fig. 6.33 (b)), besides the slightly altered ray paths, the intensities of the rays propagating downstream are higher while the intensities of the rays propagating upstream are lower.

Considering the MHD effects in the ray-tracing analysis and therefore in the intensity analysis shows in Fig. 6.30 (a) that the intensities reaching the Rx antenna areas are lower compared to the corresponding non-MHD case. However, the increased number of rays reaching the Rx antenna position increases the overall intensity at this position.

In the case of an applied magnetic field of 0.25 T at 150 kW, as shown in Fig. 6.31 (a), the intensities reaching the Rx antenna positions are higher compared to the non-MHD case (see Fig. 6.29 (b)). The high-energetic rays in bore-sight direction are reflected and refracted toward the upstream direction away from the antenna.

Further increasing the power to 175 kW results in a reduced intensity as can be seen in Fig. 6.32 (a) compared to the intensity along the trajectory of the corresponding non-MHD case in Fig. 6.29 (c).

Despite the case that no ray is reaching the receiving antenna area for 0 T and 200 kW (see Fig. 6.29 (d)) if applying a magnetic field of 0.25 T (Fig. 6.32 (a)) rays can reach the Rx antenna positions with an intensity less than those intensities indicated in the non-MHD case.

Comparing the four power levels at 0.25 T gives no clear indication that an applied magnetic field will increase or decrease the intensity of a ray. An increase in intensity at a specific antenna position may be established due to the presence of an increased amount of ray at this position.

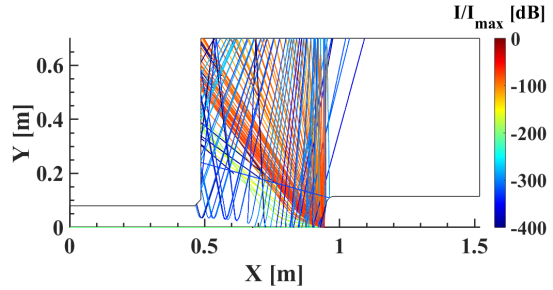

(a)

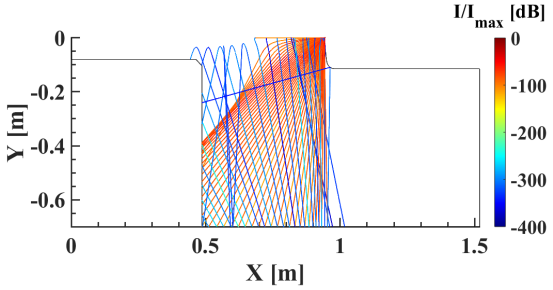

(b)

Figure 6.30: Normalized intensity for an MHD plasma case with an applied magnetic field of 0.25 T at an effective power of 125 kW, and a radio frequency of 34 GHz considering the magnetic field in the ray tracing calculation (a), and neglecting the magnetic field in the ray tracing calculation (b).

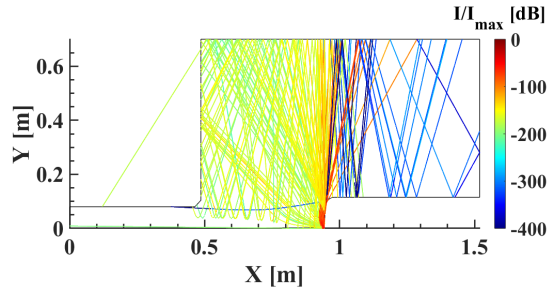

(a)

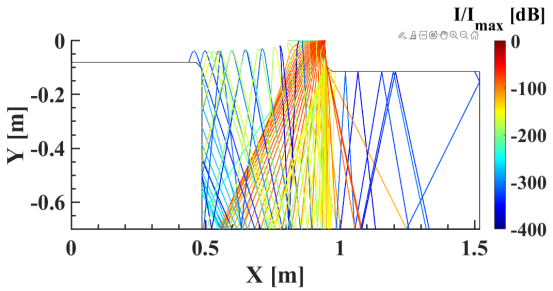

(b)

Figure 6.31: Normalized intensity for an MHD plasma case with an applied magnetic field of 0.25 T at an effective power of 150 kW, and a radio frequency of 34 GHz considering the magnetic field in the ray tracing calculation (a), and neglecting the magnetic field in the ray tracing calculation (b).

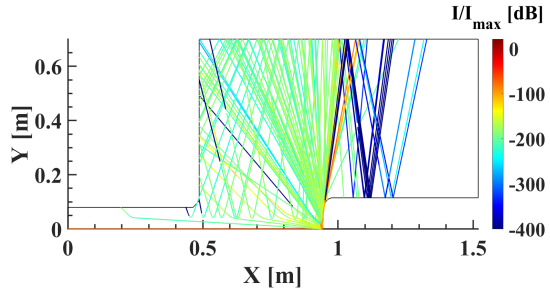

(a)

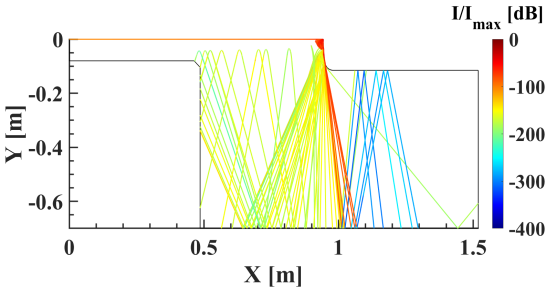

(b)

Figure 6.32: Normalized intensity for an MHD plasma case with an applied magnetic field of 0.25 T at an effective power of 175 kW, and a radio frequency of 34 GHz considering the magnetic field in the ray tracing calculation (a), and neglecting the magnetic field in the ray tracing calculation (b).

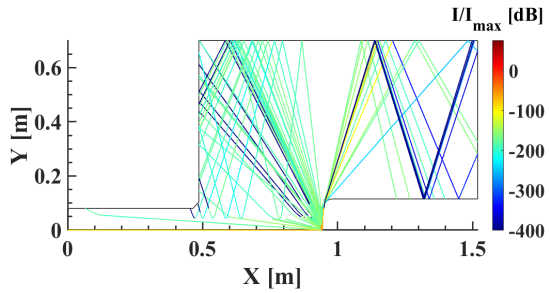

(a)

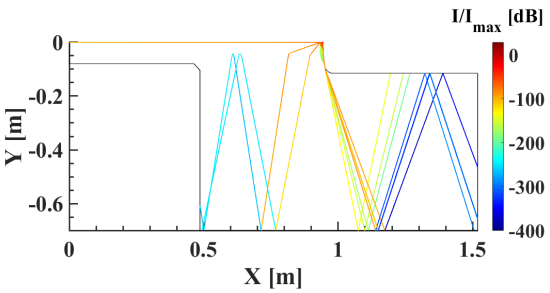

(b)

Figure 6.33: Normalized intensity for an MHD plasma case with an applied magnetic field of 0.25 T at an effective power of 200 kW, and a radio frequency of 34 GHz considering the magnetic field in the ray tracing calculation (a), and neglecting the magnetic field in the ray tracing calculation (b).

Applying a magnetic field with a maximum magnetic field strength of 0.41 T and neglecting the MHD effects in the ray tracing analysis (see Figures 6.34 - 6.37 (b)) results in similar intensity values compared to the corresponding non-MHD cases in Fig. 6.29.

A magnetic field applied with a maximum magnetic field strength of 0.41 T at 125 kW and considering the MHD effects (Fig. 6.34 (a)) the intensity values at the relevant Rx antenna positions are lower than those compared to the corresponding non-MHD case. This behavior is similar to the case at 125 kW and 0.25 T.

Increasing the power to 150 kW at 0.41T results in an increased intensity at the relevant position compared to the corresponding non-MHD case as can be seen in Fig. 6.35 (a). Compared with the 150 kW at 0.25 T shows consistency.

This consistency in intensity is also given for the cases at 175 kW. The intensities at 175 kW (Fig. 6.36 (a)) are below those calculated for the corresponding non-MHD case while at 200 kW (Fig. 6.37 (a)) the intensities of the rays reaching the relevant antenna positions seem to be higher.

Comparing the four power levels at 0.41 T also gives no clear indication that an applied magnetic field will increase or decrease the intensity of a ray except for the 200 kW case. Again, an increase in intensity at a specific antenna position may be established due to the presence of an increased amount of rays at this position.

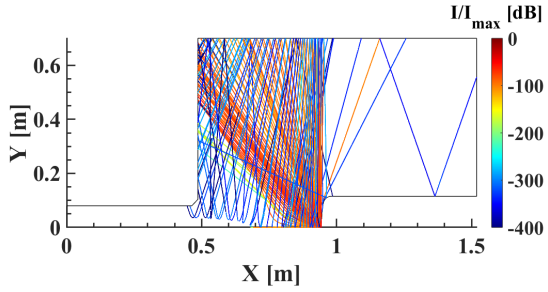

(a)

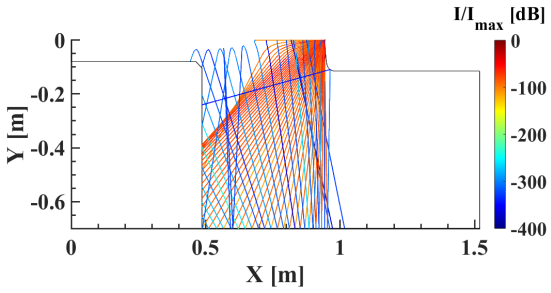

(b)

Figure 6.34: Normalized intensity for an MHD plasma case with an applied magnetic field of 0.41 T at an effective power of 125 kW, and a radio frequency of 34 GHz considering the magnetic field in the ray tracing calculation (a), and neglecting the magnetic field in the ray tracing calculation (b).

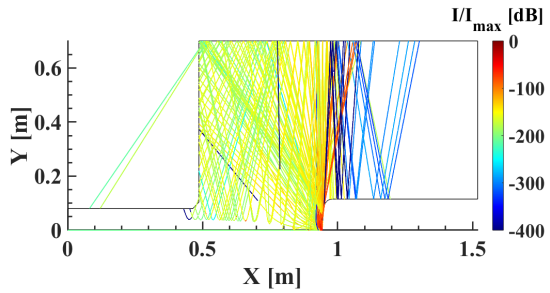

(a)

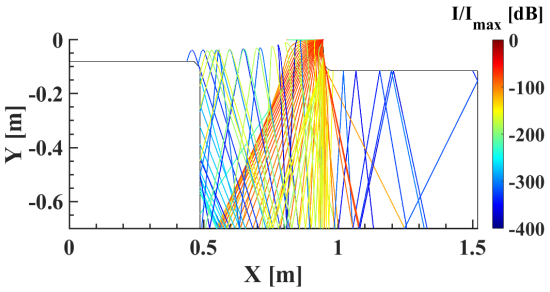

(b)

Figure 6.35: Normalized intensity solutions for an MHD plasma case with an applied magnetic field of 0.41 T at an effective power of 150 kW, and a radio frequency of 34 GHz considering the magnetic field in the ray tracing calculation (a), and neglecting the magnetic field in the ray tracing calculation (b).

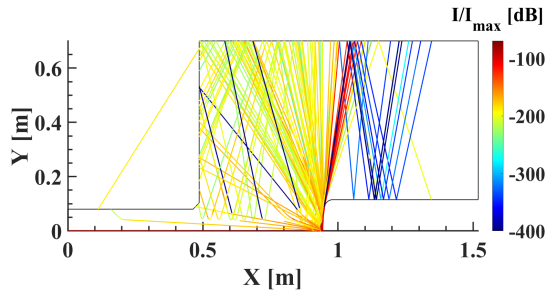

(a)

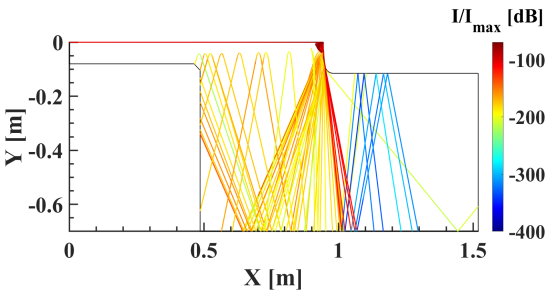

(b)

Figure 6.36: Normalized intensity for an MHD plasma case with an applied magnetic field of 0.41 T at an effective power of 175 kW, and a radio frequency of 34 GHz considering the magnetic field in the ray tracing calculation (a), and neglecting the magnetic field in the ray tracing calculation (b).

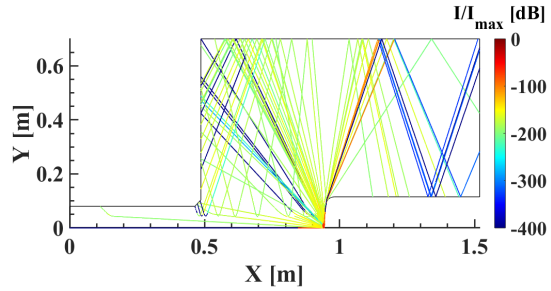

(a)

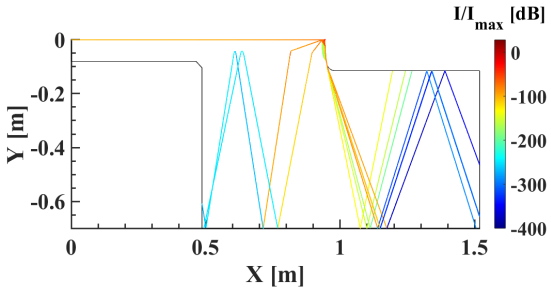

(b)

Figure 6.37: Ray-tracing solutions for an MHD plasma case with an applied magnetic field of 0.41 T at an effective power of 200 kW, and a radio frequency of 34 GHz considering the magnetic field in the ray tracing calculation (a), and neglecting the magnetic field in the ray tracing calculation (b).

As mentioned earlier, if a magnetic field of 1 T is applied the ray-tracing solutions neglecting the MHD effects alter compared to the non-MHD cases, especially for the case at 200 kW power. The intensity values for the cases at 125 kW and 150 kW (see Figures 6.38, and 6.39) are similar to their corresponding non-MHD cases at the relevant positions. In the case of an input power of 175 kW at 1 T, the intensities are less than the corresponding non-MHD case. At an input power of 200 kW, the intensities increase significantly overall when a magnetic field of 1 T is applied.

Considering the MHD effects in the ray-tracing the resulting intensities at a power level of 125 kW at 1 T are below the corresponding non-MHD case if comparing Fig. 6.38 (a) with Fig. 6.29 (a). Again, more rays are reaching the relevant positions and therefore the intensity may be higher. The same behavior is observed for the case at 1 T and 150 kW (Fig. 6.39 (a)) and the case at 1 T and 175 kW (Fig. 6.40 (a)). The intensities at the relevant positions are decreased compared to the non-MHD cases with more rays reaching the aforementioned positions. The results are significantly different for the 200 kW at 1T case (see Fig. 6.41 (a)) in which the intensity values increased.

If a magnetic field of 1 T is applied, the aforementioned reflection and refraction of the bore-sight rays toward the upstream is reduced significantly.

Comparing the four cases at 1 T leads to the conclusion that the intensity values increase with increasing power levels. This is counter-intuitive since a higher electron number density leads to higher refractive index gradients thus leading to more disruption in non-MHD cases. However, a magnetic field of 1 T in combination with a high electron number density seems to result in smoother refractive index gradients and therefore in less attenuation of the electromagnetic wave. Nevertheless,

the number of rays reaching the Rx antenna positions is less at 200 kW compared to the other three power levels.

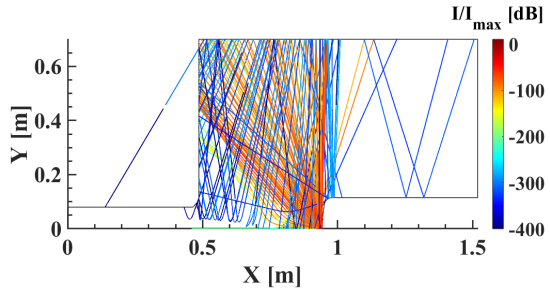

(a)

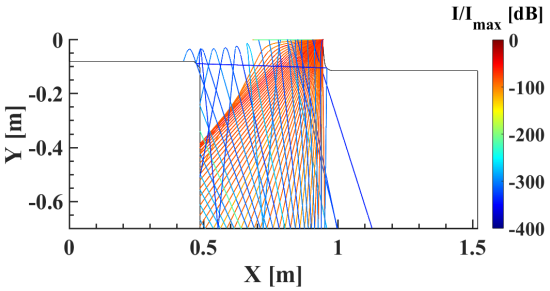

(b)

Figure 6.38: Normalized intensity for an MHD plasma case with an applied magnetic field of 1 T at an effective power of 125 kW, and a radio frequency of 34 GHz considering the magnetic field in the ray tracing calculation (a), and neglecting the magnetic field in the ray tracing calculation (b).

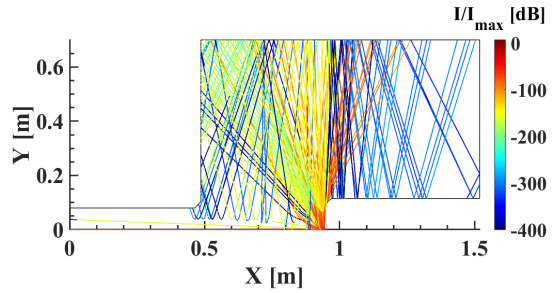

(a)

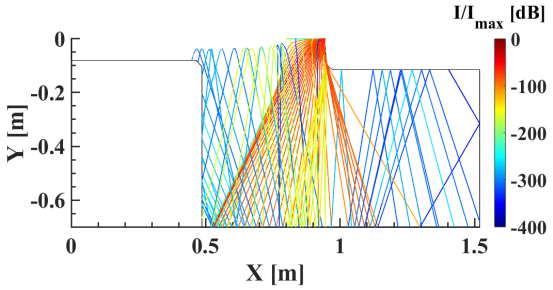

(b)

Figure 6.39: Normalized intensity for an MHD plasma case with an applied magnetic field of 1 T at an effective power of 150 kW, and a radio frequency of 34 GHz considering the magnetic field in the ray tracing calculation (a), and neglecting the magnetic field in the ray tracing calculation (b).

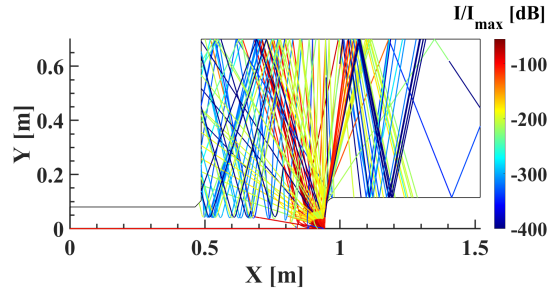

(a)

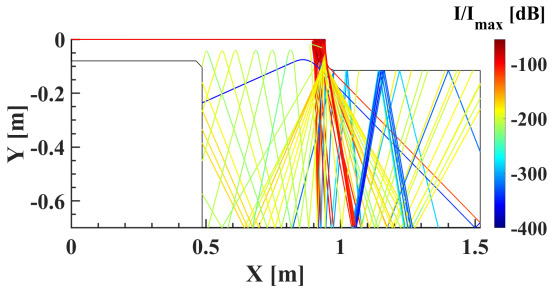

(b)

Figure 6.40: Normalized intensity for an MHD plasma case with an applied magnetic field of 1 T at an effective power of 175 kW, and a radio frequency of 34 GHz considering the magnetic field in the ray tracing calculation (a), and neglecting the magnetic field in the ray tracing calculation (b).

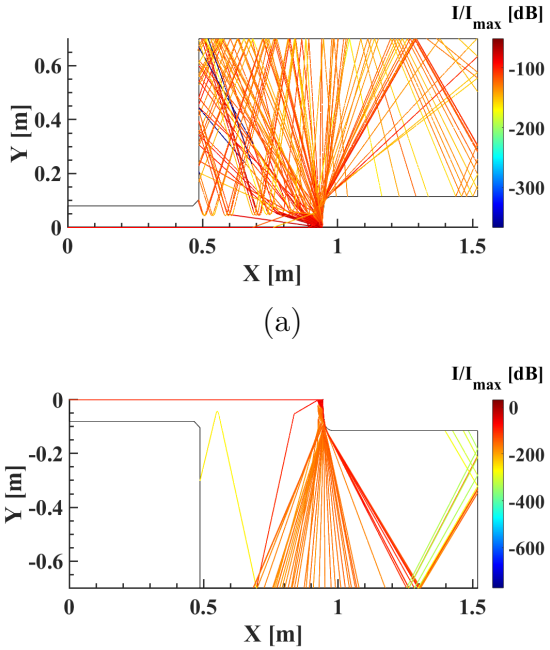

Figure 6.41: Normalized intensity for an MHD plasma case with an applied magnetic field of 1 T at an effective power of 200 kW, and a radio frequency of 34 GHz considering the magnetic field in the ray tracing calculation (a), and neglecting the magnetic field in the ray tracing calculation (b).

6.2.2.9 Validation with on-ground experiments: S-parameter analysis

The S-parameter for a radio frequency of 34 GHz is analyzed for magnetic field strengths of 0.25 T and 0.41 T and power levels to validate BORAT against on-ground experiments at VKI. The experiment was not performed at a magnetic field strength of 1 T. The results of the S-parameter validation study are presented in table form at first because the numerical results differ partially drastically compared to the experimental results, which makes a visual presentation of the results less intuitive. An error estimation was neglected due to the partially large discrepancies. The nomenclature of the S-parameter is as follows:

1. $S_{21,O}$ is the calculated S-parameter from the ordinary wave.
2. $S_{21,X}$ is the calculated S-parameter from the extraordinary wave.
3. $S_{21,t}$ is the total calculated S-parameter.
4. $S_{21,exp}$ is the measured S-parameter in the experiment.

Difficult operating conditions for the ray tracer and therefore difficulties in generating solutions in combination with the heavy computational cost for MHD calculations lead to the choice of reducing the ray density. The nature of anistropic plasma leading to unforecastable ray trajectories makes it difficult to predict the initial radiation direction by keeping the maximum number of rays limited for calculations on an HPC.

Table 6.2: Comparison of the S-parameter for non-MHD cases at various power levels at a radio frequency of 34 GHz

B-field [T]	0				
Power [kW]	0	125	150	175	200
$S_{21,t}$ [dB]	-44.82	-304.66	-272.63	-137.19	-194.37
$S_{21,exp}$ [dB]	-45.47	-42.88	-43.41	-47.81	-46.97
$S_{31,t}$ [dB]	-44.05	-318.59	-274.54	-145.04	-196.90
$S_{31,exp}$ [dB]	-44.72	-46.63	-48.90	-49.75	-49.70
$S_{41,t}$ [dB]	-53.06	-297.77	-270.65	-154.81	-65.05
$S_{41,exp}$ [dB]	-53.30	-47.07	-51.41	-52.90	-51.88

Table 6.3: Comparison of the S-parameter for MHD cases at various power and magnetic field strength levels at a radio frequency of 34 GHz

B-field [T]	0.25				0.41			
Power [kW]	125	150	175	200	125	150	175	200
$S_{21,O}$ [dB]	-255.7	-154.3			-226.6	-183.1		
$S_{21,X}$ [dB]	-61.8	-148.2	-129.4	-127.5	-260.9	-121.6	-114.1	-110.6
$S_{21,t}$ [dB]	-61.8	-144.7	-129.4	-127.5	-226.5	-121.6	-114.1	-110.6
$S_{21,exp}$ [dB]	-41.9	-44.9	-46.9	-43.8	-40.9	-42.9	-45.4	-43.9
$S_{31,O}$ [dB]	-256.8	-152.0			-226.1	-179.6		
$S_{31,X}$[dB]	-61.3	-154.9	-131.9	-130.0	-260.2	-121.3	-117.6	-109.4
$S_{31,t}$ [dB]	-61.3	-147.3	-131.9	-130.0	-225.9	-121.3	-117.6	-109.4
$S_{31,exp}$ [dB]	-45.5	-50.6	-50.7	-47.9	-46.2	-50.1	-51.0	-48.4
$S_{41,O}$ [dB]	-248.3	-134.7			-252.0	-140.9	-210.4	-175.6
$S_{41,X}$ [dB]	-47.1	-83.2	-119.6	-143.2	-229.1	-112.7	-109.8	-96.8
$S_{41,t}$ [dB]	-47.1	-83.2	-119.6	-143.2	-229.1	-112.4	-109.8	-96.8
$S_{41,exp}$ [dB]	-47.7	-50.9	-51.1	-50.9	-48.0	-51.9	-51.4	-51.0

The results for non-MHD conditions can be found in Table 6.2. The numerical and experimental S-parameter for the non-MHD, non-plasma case match well. The differences are below 1 dB. This shows the principle functionality of the signal characterization method. The experimental measured S-parameter show neither a significant influence of an applied nor a significant change for various power levels. Analyzing the non-MHD cases for the four power levels shows a large discrepancy between the measured and numerically calculated S-parameters. The attenuation measured in the experiments is in the same order of magnitude as the non-MHD, non-plasma case. The gaps between the numerical and experimental results reach from 13 dB for $S_{41,t}$ at 200 kW up to 272 dB for $S_{31,t}$ at 125 kW. It is worth mentioning that a 3 dB difference is a factor of two in linear units. Interestingly, the discrepancy between the numerical and experimental results decreases with increasing power. Analyzing the ray trajectories shows that no direct rays are reaching the receiving antennas only reflected rays reach them. For low-power cases, the high-energetic rays in bore-sight are refracted away leaving the domain away from the receiving antennas. The low-energetic side lobe rays reach the antenna position through wall reflections reaching the receiving antenna at low-energetic side lobes leading to a high attenuation. When increasing the power more high-energetic rays from the original bore-sight direction reach the antenna due to refraction and reflection.

Analyzing the S-parameter for MHD cases shows that the main contribution to the total S-parameter is provided by the extraordinary wave. The refractive index of the extraordinary wave is higher compared to the refractive index of the ordinary wave in the presence of large magnetic fields leading to less disturbance along the trajectory except if cut-off conditions are reached (see detailed explanation in Section 6.2.1). Interestingly, at power levels of 175 kW and 200 kW, no ordinary rays reach the three receiving antenna positions except for antenna four at 0.41 T. As mentioned before the ray trajectories are not predictable in an anisotropic plasma due to the dependency of the refractive index on the angle between the wave propagation direction and the magnetic field vector.

The attenuation decreases with increasing power levels in case a magnetic field of 0.41 T is applied at all receiving antennas. This was also observed for the non-MHD cases. Interestingly, the attenuation increases with increasing power levels when a magnetic field of 0.25 T is applied.

The numerically calculated total S-parameters and the experimentally measured S-parameter are plotted over the four power levels in Fig. 6.42. As mentioned before neither an effect of the magnetic field nor the an effect in increasing electron number density can be seen in the experimental data. The $S_{21,t}$ and $S_{31,t}$ show a very similar behavior for different power levels. These two antenna positions are almost mirrored at the Y-axis. At these antenna positions, an applied magnetic field is in general reducing the attenuation. It seems like a weaker magnetic field performs better for lower power levels and vice versa when increasing the power levels. This would mean that the magnetic field needs to be adjusted to the flow conditions.

The outcome for the S-parameter analysis of antenna four ($S_{41,t}$) is different compared to the two other receiving antennas. A magnetic field of 0.25 T is also outperforming the non-MHD case and the 0.41 T case at lower frequencies. A stronger magnetic field shows a reduced attenuation with increasing frequencies but the lowest attenuation at 200 kW is reached without an applied magnetic field.

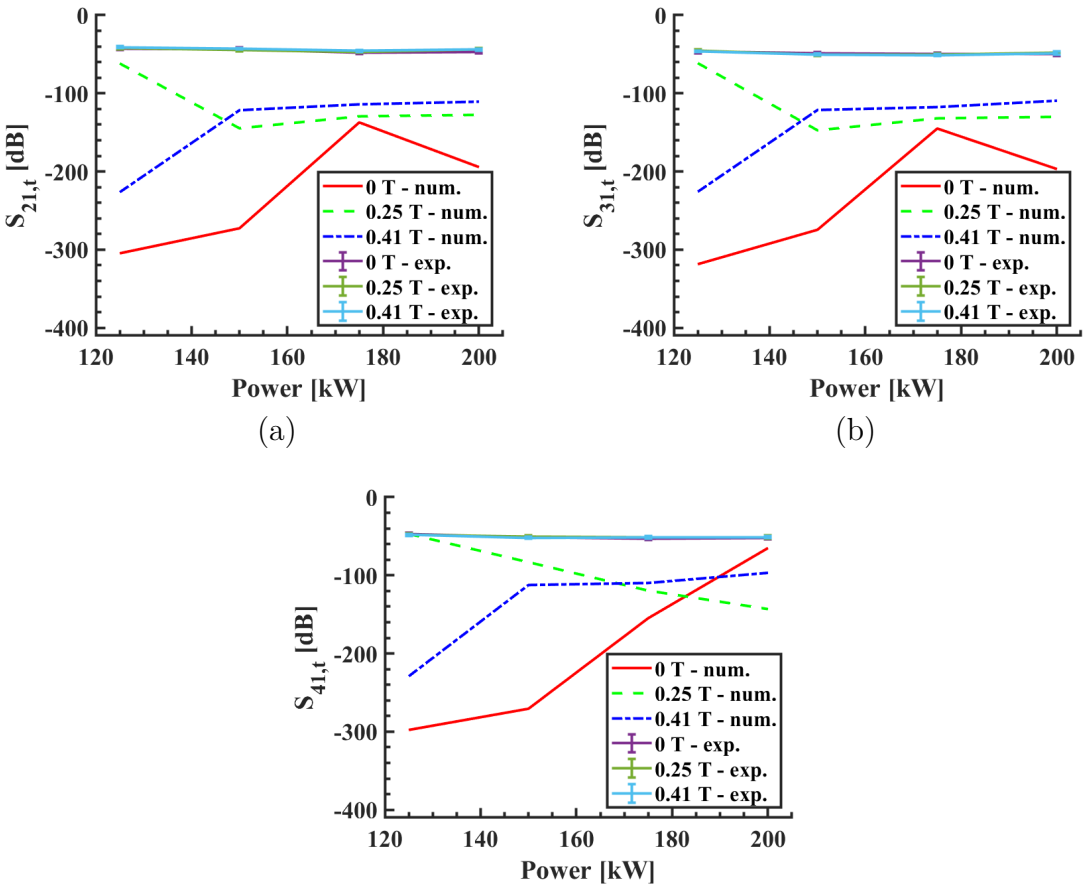

Figure 6.42: S-parameter analysis over various power levels for magnetic field strengths of 0 T, 0.25T, and 0.41T

6.3 Conclusion

The analytical analysis of the resulting refractive index of a magnetized plasma as a function of magnetic field strength and electron number density showed that the effect of a magnetic field on the ordinary wave is reduced from parallel to perpendicular propagation of the wave concerning the magnetic field vector. The resulting refractive index for the extraordinary wave is at least or greater than one if a certain magnetic field strength is reached depending on the electron number density and the angle between the wave vector and the magnetic field vector. An increase in the angle between the wave vector and the magnetic field vector reduces the

The outcomes of the validation show that large discrepancies exist between the numerically calculated and the experimentally measured S-parameter in the case a plasma (and a magnetic field) is present. Difficult operating conditions, complex physics, and a limited influence of the magnetic field and the electron number densities in the flow domain for the experimental data make validation difficult.

From the analysis of the S-parameter over various frequencies at different antenna positions, it can be concluded, that the magnetic field properties need to be adjusted to the flow conditions. Weaker magnetic field strengths seem to reduce the signal attenuation in lower electron number density plasmas. With increasing electron number densities stronger magnetic fields further reduce the signal attenuation. Furthermore, the position and the alignment between the transmitting and receiving antenna are important. Line-of-sight alignment is not automatically the best-case scenario depending on the flow properties, antenna characteristics, and the possible magnetic field properties.

Overall, an applied magnetic field shows a positive effect on the ray propagation and the signal characteristics.

The response to the initial research questions reads as follows:

1. How are the ray propagation and the signal affected by the magnetic field?

   An applied magnetic field reduces the attenuation in general but the magnetic field properties should be adjusted to the flow field properties.

2. Is the magnetic window method sufficient to mitigate radio communication blackout?

   According to the numerical analysis, the magnetic windowing method reduces the signal attenuation and is, therefore, a suitable radio blackout mitigation method.

A further analysis with larger magnetic field strengths will show if the effect of an applied magnetic field reaches a threshold. The effect and necessity of heavy particle collisions and additional energy splitting between the ordinary and extraordinary waves in magnetized plasma will also be analyzed in future work. A second validation campaign including further investigation in the experimental results might bring additional benefit and improve the agreement between the numerical solutions and the experimental results.

7 Conclusion

This chapter contains the conclusion and outlook of the PhD thesis. The research is summarized and the research questions mentioned in the Introduction are answered. An outlook of future research and applications of BORAT is given as well.

Contents

7.1 Summary of the work

Within this work, an existing ray tracing algorithm was further developed to analyze the effect of a magnetized plasma, besides the effect of a plasma, on the signal propagation path and how the signal properties are altered along the ray trajectory. Firstly, the reasons, historical missions, and the relevancy of the radio communication blackout mitigation research for current and future applications were introduced and different radio blackout mitigation schemes were mentioned.

The development of a Magnetohydrodynamics (MHD) ray tracer marks a significant advancement in the field of hypersonic flight and atmospheric entry analysis. This tool is capable of analyzing signal properties along the ray trajectory and performing comprehensive antenna network analysis. It effectively bridges the gap between high-speed fluid dynamics of plasma flows and electromagnetic wave theory, providing a more nuanced understanding of complex physical phenomena. The MHD ray tracer's ability to operate in the context of magnetized plasma and its capacity to analyze signal propagation in scenarios involving arbitrary inhomogeneous plasma, diverse incident waves, and a wide range of fluid compositions, sets it apart from existing models. Furthermore, the integration of signal characterization into the ray tracer allows for a detailed examination of how plasma and magnetic fields affect signal characteristics. The successful validation of this tool with on-ground experiments at the von Karman Institute for Fluid Dynamics (VKI) underscores its reliability and effectiveness. The development of this MHD ray tracer represents a promising step towards mitigating radio blackout, and enhancing the safety and success of space missions.

7.2 Contribution

The first question is to identify **the effect of plasma on the signal propagation path**. The plasma effect was analyzed in Chapter 4 to 6. A plasma can have several effects on the signal propagation path. In the case of a non-magnetized plasma, the signal trajectory can be completely attenuated or blocked if the electron number density is above the critical electron number density of the radio frequency. Low ionized plasma with an electron number density much smaller than the radio frequency and smooth gradients has a limited effect on the propagation path. High gradients, like a plasma stream in a vacuum chamber or the hot gas temperatures around the shoulder of a probe under testing or entry vehicle, cause a bending of the propagation path. Plasma has, depending on the refractive index gradient in the domain, a lensing effect causing the rays to converge or diverge. Line-of-sight (LOS) assumption in high refractive index gradient cases is often not applicable since we showed that the radio signal takes complex paths. The plasma region with an electron number density below the critical electron number density is called brownout. In a brownout case, there is the possibility of receiving a radio signal away from the vehicle with the transmitting antenna, but not necessarily in LOS direction. However, the pure analysis of the signal propagation path neither gives insights into the signal quality nor the signal intensity.

Second, **the effect of a magnetized plasma on the signal propagation path** is of interest. The physics in a magnetized plasma is more complex. The presence of a magnetic field affects on one side the flowfield and on the other side there is a dependency of the refractive index on the magnetic field vector and the

wave vector. The latter does not allow predictions of the (magnetized) plasma effect in arbitrary cases. Additionally, the refractive index of a magnetized plasma, even if heavy particle collisions are not considered, can become complex and therefore cause absorption in the plasma. The refractive index can also be greater than one. In cases where the magnetic field vector is perpendicular or parallel to the wave vector predictions can be made and compared with literature. It showed that the magnetized plasma, compared to similar operating conditions without an applied magnetic field, increases the radiation aperture angle with increasing magnetic field strength. The increased aperture angle makes a larger radius of possible communication directions possible. The refractive index gradients seem to be smaller in the analyzed cases leading to less ray bending.

Third, **the effect of plasma on the radio signal** was analyzed with the signal characterization method. In a collision-less non-magnetized plasma several factors affect the signal properties. The spread factor, which is comparable to the free space loss if no plasma is present, can increase or decrease the signal intensity or power density depending on the electron number density in the flow domain by causing divergent or convergent ray trajectories. The Fresnel coefficients for reflection and refraction can increase or decrease the amplitude of the electric field vector and cause a change in polarization angle. The refractive index, which is in a collision-less case always real, causes a phase shift in the signal bundle (ray). If heavy particle collisions are relevant, an additional energy absorption is present in the plasma. Interference is negligible according to the analyzed cases but can become important as well. The additional change in the polarization angle caused by the Faraday rotation due to the presence of Earth's magnetic field in experiments is small. From the results we can conclude that the plasma causes an additional attenuation of the signal. The effect of the free space loss is greater than the reduced plasma influence on the spread factor for higher frequencies.

Fourth, we analyzed **the effect of a magnetized plasma on the signal properties**. Besides the mentioned effects of a non-magnetized plasma on a radio wave additional effects occur. An applied magnetic field causes significant Faraday rotations close to the magnet with reduced influence further away. The refractive index can be complex and therefore absorptive even heavy particle collisions are neglected. An applied magnetic reduces the attenuation calculated between two antennas leading to improved communication. The results show that the magnetic field properties should be adjusted to the flow properties.

Fifth, **the suitability of the magnetic windowing method** for radio blackout mitigation is of interest. The functionality of the magnetic windowing method was shown. A pre-analysis of the required magnetic field strengths is required to operate in ideal conditions. For entry capsules or hypersonic cruising vehicles, a decent magnet size can create a corridor with a sufficiently low refractive index for the radio signal depending on the frequency. Uncertainties in the experiments are sometimes putting the positive effects of an applied magnetic field in perspective.

Lastly, it is of interest if **the numerical tool can be validated** against on-ground experiments. The extended version of BORAT with signal characterization was successfully validated with on-ground experiments at VKI for non-magnetized cases. However, uncertainties on the numerical and experimental sides are not negligible. The numerical results are well within the error margins but cannot represent the trend of the scattering parameter with increasing frequencies. There

might be additional effects in the experiment not captured in the 2D ray tracer with signal characterization. Additional 3D effects, besides the challenging experimental environment, might also be the reason for the discrepancies in the validation of MHD cases. However, the validation of the MHD cases gave additional insights to the behavior of electromagnetic waves in anisotropic plasma.

7.3 Future work

In the next step, the effect of heavy particle collisions at high magnetic field strengths will be analyzed. Heavy particle collisions will increase the plasma attenuation and change the refractive index leading to an altered ray path. The analysis of larger magnetic fields will show if there arises a threshold of improvements in signal characterization. A hybrid ray-tracer for magnetized (anisotropic) plasma might improve computational cost and accuracy, especially for validation purposes, by applying the Huygens principle after leaving the plasma area and using a full wave analysis, which requires fewer rays. Implementing a machine learning algorithm into BORAT might be useful to analyze decent antenna positions, antenna types, beamforming possibilities, and improved magnetic field properties.

In a further step, a 3D version of BORAT will show if there are effects in experiments not captured in the 2D version. Atmospheric entries with an angle of attack other than zero would also need a 3D analysis. On-ground experiments in infrared frequencies would make it possible to visualize the signal propagation for further physical understanding and improvement in the numerical tool. Additionally, the effect of a pulsed magnetic field instead of a steady magnetic field can be analyzed, promising a reduced magnet size and cooling requirements. Extending the refractive index equation to account for dusty plasma will improve the accuracy in atmospheric entry analysis or the analysis of communication interruption during launches on other celestial bodies. Furthermore, the radar cross-section of hypersonic cruising vehicles and satellites with electric propulsion systems can be analyzed with BORAT for tracking and identification.

List of Articles

Journal articles included in this dissertation:

- J. S. Laur, V. F. Giangaspero, V. Sharma, A. Lani, N. Donaldson, M. K. Kim, J. Giacomelli, G. Herdrich, A. Hein, and J. Thoemel, “Radio communication blackout mitigation: Analyzing magnetic field effects via ray-tracing analysis,” AIAA Journal, pp. 1–12, Apr. 2024.
- J. S. Laur, V. F. Giangaspero, V. Sharma, A. Lani, D. Luis, A. Viladegut, J. L. Gonzales Rios, J. Querol, J. A. Vasquez Peralvo, J. C. Merlano Duncan, A. M. Hein, and J. Thoemel, “Radio Blackout Mitigation: 2D Ray Tracing and Signal Analysis in Unmagnetized Plasma,” AIAA Journal. (not published yet)
- J. S. Laur, V. F. Giangaspero, V. Sharma, A. Lani, D. Luis, A. Viladegut, J. L. Gonzales Rios, J. Querol, J. A. Vasquez Peralvo, J. C. Merlano Duncan, A. M. Hein, and J. Thoemel, “Radio Blackout Mitigation: 2D Ray Tracing in Magnetized Plasma with Signal Analysis,” AIAA Journal. (not published yet)

Conference articles:

- J. Laur, V. Giangaspero, V. Sharma, A. Lani, N. Donaldson, M. Kim, J. Giacomelli, G. Herdrich, A. Hein, and J. Thoemel. "The Effect of an Applied Magnetic Field onto the Re-entry Radio Communication Blackout." In Proceedings of the 2nd International Conference on Flight Vehicles, Aerothermodynamics and Re-entry Missions Engineering. 2022.
- J. Laur, D. Luis, A. Viladegut, V. F. Giangaspero, A. Lani, J. L. Gonzalez Rios, J. Querol et al. "Radio Communication Blackout Mitigation: Ray Tracing Analysis and Signal Characterization Including Experimental Validation for Non-magnetized Plasmas." Paper presented at AEC 2023 - 10th EUCASS - 9th CEAS, Lausanne, Switzerland, 02 October 2023. doi:10.13009/EUCASS2023-487.
- J. Laur, D. Luis, A. Viladegut, V. F. Giangaspero, A. Lani, J. L. Gonzalez Rios, J. Querol et al. "Radio Communication Blackout Mitigation: 2D Ray Tracing Analysis of Magnetized Plasma with Signal Characterization." Paper presented at AIAA SciTech 2024, Orlando, Florida, 2024.

Co-authored articles:

- O. Borgue, K. Kanavouras, J. Laur, J. Thoemel, L. Rana, and A. Hein. "Developing a distributed and fractionated system of 10 grams satellites for planetary observation." In Proceedings of the International Astronautical Congress, IAC2. Paris, France: IAF, 2022.
- A. Lani, V. Sharma, V. F. Giangaspero, S. Poedts, A. Viladegut, O. Chazot, J. Giacomelli et al. "A Magnetohydrodynamic enhanced entry system for space transportation: MEESST." Journal of Space Safety Engineering (2022). doi:10.1016/j.jsse.2022.11.004.
- Vincent F. Giangaspero, Vatsalya Sharma, Johannes Laur, Jan Thoemel, Alessandro Munafò, Andrea Lani, Stefaan Poedts, "3D ray tracing solver for communication blackout analysis in atmospheric entry missions." Computer Physics Communications (2023). doi: 10.1016/j.cpc.2023.108663

Bibliography

[1] S. Varrette, P. Bouvry, H. Cartiaux, and F. Georgatos, "Management of an academic hpc cluster: The ul experience," in *Proc. of the 2014 Intl. Conf. on High Performance Computing & Simulation (HPCS 2014)*, (Bologna, Italy), pp. 959–967, IEEE, July 2014.

[2] C. A. Balanis, *Antenna theory : : analysis and design /.* Hoboken, New Jersey: Wiley, fourth edition. ed., 2016 - 2016.

[3] A. Knapp, H. Fulge, G. Herdrich, N. Ono, R. Wernitz, M. Auweter-Kurtz, H.-P. Roser, and S. Fasoulas, "Investigation of mhd impact on argon plasma flows by variation of magnetic flux density," *The open plasma physics journal*, vol. 5, no. 1, 2012.

[4] A. V. A. L. A. C. O. C. D. Luis, V. F. Giangaspero, "Effect of electron number densities on the radio signal propagation in an inductively coupled plasma facility," 2023 (not published yet).

[5] E. Papadopoulou, P. Leyland, N. Banerji, and E. Fay, "Numerical Simulations of the Apollo 4 Reentry Trajectory," tech. rep., 2013.

[6] E. Josyula, *Hypersonic nonequilibrium flows : : fundamentals and recent advances /.* Progress in Astronautics and Aeronautics ; Volume 247, Reston, Virginia: American Institute of Aeronautics and Astronautics, Inc., 2015 - 2015.

[7] P. H. Oosthuizen, *Introduction to compressible fluid flow /.* Heat transfer, Boca Raton, Florida: CRC Press/Taylor Francis Group, second edition. ed., 2014.

[8] P. M. Sforza, *Manned spacecraft design principles /.* Elsevier aerospace engineering series, Amsterdam: Elsevier, 2016.

[9] E. S. De Góes Maciel and A. P. Pimenta, "Thermochemical non-equilibrium entry flows in Mars in two-dimensions - Part II," *WSEAS Transactions on Mathematics*, vol. 13, no. September, pp. 201–223, 2014.

[10] H. Zhou, X. Li, K. Xie, Y. Liu, and Y. Yu, "Mitigating reentry radio blackout by using a traveling magnetic field," *AIP Advances*, vol. 7, oct 2017.

[11] G. He, Y. Zhan, N. Ge, Y. Pei, and Y. Zhao, "Channel Characterization and Finite-State Markov Channel Modeling for Time-Varying Plasma Sheath Surrounding Hypersonic Vehicles," tech. rep., 2014.

[12] E. D. Gillman, J. E. Foster, and I. Blankson, "Review of leading approaches for mitigating hypersonic vehicle communications blackout and a method of ceramic particulate injection via cathode spot arcs for blackout mitigation," 2010.

[13] M. Keidar, M. Kim, and I. D. Boyd, "Electromagnetic reduction of plasma density during atmospheric reentry and hypersonic flights," *Journal of Spacecraft and Rockets*, vol. 45, pp. 445–453, may 2008.

[14] G. He, Y. Zhan, and N. Ge, "ADAPTIVE TRANSMISSION METHOD FOR ALLEVIATING THE RADIO BLACKOUT PROBLEM," *Progress In Electromagnetics Research*, vol. 152, pp. 127–136, 2015.

[15] S. Li and X. Jiang, "Review and prospect of guidance and control for Mars atmospheric entry," 2014.

[16] Y. Takahashi, R. Nakasato, and N. Oshima, "Analysis of radio frequency blackout for a blunt-body capsule in atmospheric reentry missions," *Aerospace*, vol. 3, p. 2, jan 2016.

[17] G. Herdrich, "Raumfahrtrelevante plasmen und deren anwendungsbezogene klassifizierung," 2012.

[18] K. Minkwan, M. Keidar, and I. D. Boyd, "Analysis of an electromagnetic mitigation scheme for reentry telemetry through plasma," *Journal of Spacecraft and Rockets*, vol. 45, no. 6, pp. 1223–1229, 2008.

[19] M. Kim and A. Gülhan, "Plasma manipulation using a mhd-based device for a communication blackout in hypersonic flights," in *Proceedings of 5th International Conference on Recent Advances in Space Technologies - RAST2011*, pp. 412–417, 2011.

[20] B. A. Webb and R. W. Ziolkowski, "A metamaterial-inspired approach to mitigating radio frequency blackout when a plasma forms around a reentry vehicle," *Photonics*, vol. 7, pp. 1–22, dec 2020.

[21] D. D. Morabito, "The Spacecraft Communications Blackout Problem Encountered during Passage or Entry of Planetary Atmospheres," tech. rep., 2002.

[22] Y. Takahashi, K. Yamada, and T. Abe, "Prediction Performance of Blackout and Plasma Attenuation in Atmospheric Reentry Demonstrator Mission," tech. rep.

[23] R. A. Hartunian, G. E. Stewart, T. J. Curtiss, S. D. Fergason, R. W. Seibold, and P. Shome, "Implications and mitigation of radio frequency blackout during reentry of reusable launch vehicles," *AIAA Atmospheric Flight Mechanics Conference*, vol. 2, no. August, pp. 1070–1079, 2007.

[24] L. Shi, B. Bai, Y. Liu, and X. Li, "Navigation antenna performance degradation caused by plasma sheath," *Journal of Electromagnetic Waves and Applications*, vol. 27, pp. 518–528, Jan. 2013.

[25] S. A. Bendoukha, K.-i. Okuyama, and B. Szasz, "a Study of Radio Frequency Blackout for Space Probe During Atmospheric Reentry Phase," *International Journal of Research -GRANTHAALAYAH*, vol. 5, no. 3, pp. 1–15, 2017.

[26] D. D. Morabito, B. Schratz, K. Bruvold, P. Ilott, K. Edquist, and A. Dwyer Cianciolo, "The Mars Science Laboratory EDL Communications Brownout and Blackout at UHF," tech. rep., 2014.

[27] P. Tran and J. Paulat, "Re-entry Flight Experiments Lessons Learned – The Atmospheric Re-entry Demonstrator ARD," *Nato Rto*, pp. 1–46, 2007.

[28] H. Böhrk, C. Dittert, H. Weihs, T. Thiele, and A. Gülhan, "Sharp leading edge at hypersonic flight: Modeling and flight measurement," *Journal of Spacecraft and Rockets*, vol. 51, pp. 1753–1760, sep 2014.

[29] G. Rosen, "Method for the Removal of Free Electrons in a Plasma," *The Physics of Fluids*, vol. 5, pp. 737–738, 06 1962.

[30] Y. Takahashi, K. Yamada, and T. Abe, "Examination of radio frequency blackout for an inflatable vehicle during atmospheric reentry," *Journal of Spacecraft and Rockets*, vol. 51, pp. 430–441, mar 2014.

[31] N. Sternberg and A. I. Smolyakov, "Resonant transmission of electromagnetic waves in multilayer dense-plasma structures," *IEEE Transactions on Plasma Science*, vol. 37, no. 7 PART 2, pp. 1251–1260, 2009.

[32] J. X. Liu, Y. Zhao, J. J. Lv, S. Qu, T. Y. Liu, T. P. Yu, and J. Zhao, "THz wave propagation in the stagnation region of reentry plasma sheath," *AIP Advances*, vol. 11, no. 6, 2021.

[33] H. Kaushal and G. Kaddoum, "Optical Communication in Space: Challenges and Mitigation Techniques," *IEEE Communications Surveys and Tutorials*, vol. 19, no. 1, pp. 57–96, 2017.

[34] S. Poddar and D. Sharma, "Blackout mitigation during space vehicle re-entry," *Optik*, vol. 126, no. 24, pp. 5899–5902, 2015.

[35] R. Starkey, *Electromagnetic Wave / Magnetoactive Plasma Sheath Interaction for Hypersonic Vehicle Telemetry Blackout Analysis.*

[36] H. Usui, F. Yamashita, and H. Matsumoto, "Computer experiments on the measurement of reentry plasma with radio waves," *Advances in Space Research*, vol. 24, no. 8, pp. 1069–1072, 1999. Active Experiments in Space Plasmas.

[37] M. K. Kim, "ELECTROMAGNETIC MANIPULATION OF PLASMA LAYER FOR RE-ENTRY BLACKOUT MITIGATION," tech. rep.

[38] A. Lani, V. Sharma, V. F. Giangaspero, S. Poedts, A. Viladegut, O. Chazot, J. Giacomelli, J. Oswald, A. Behnke, A. S. Pagan, G. Herdrich, M. Kim, N. D. Sandham, N. L. Donaldson, J. Thoemel, J. C. Duncan, J. S. Laur, S. I. Schlachter, R. Gehring, M. Dalban-Canassy, J. Tanchon, V. Große, P. Leyland, A. Casagrande, M. L. R. Betancourt, M. Collier-Wright, and E. Bögel, "A magnetohydrodynamic enhanced entry system for space transportation: Meesst," *Journal of Space Safety Engineering*, vol. 10, no. 1, pp. 27–34, 2023.

[39] R. Starkey, "Electromagnetic wave / magnetoactive plasma sheath interaction for hypersonic vehicle telemetry blackout analysis," in *34th AIAA Plasmadynamics and Lasers Conference*, American Institute of Aeronautics and Astronautics, jun 2003.

[40] H.-s. Xie, B. Debabrata, Y.-k. Bai, H.-y. Zhao, and J.-c. Li, "Boray: An axisymmetric ray tracing code supports both closed and open field lines plasmas," 05 2021.

[41] J.-P. Rossi and A. J. Levy, "A ray model for decimetric radiowave propagation in an urban area," *Radio Science*, vol. 27, no. 06, pp. 971–979, 1992.

[42] A. O. Kaya, L. J. Greenstein, and W. Trappe, "Characterizing indoor wireless channels via ray tracing combined with stochastic modeling," *IEEE Transactions on Wireless Communications*, vol. 8, no. 8, pp. 4165–4175, 2009.

[43] L. Guo, L. Guo, and L. Gan, "Investigation of effects of plasma sheath on antenna radiation based on ray tracing method," *AIP Advances*, vol. 11, 08 2021. 085116.

[44] J. Zhou and Y. Han, "Analysis of plasma sheath propagation attenuation based on ray tracing," *Contributions to Plasma Physics*, vol. 62, no. 1, p. e202100071, 2022.

[45] D. Morabito, B. Schratz, K. Bruvold, P. Ilott, K. Edquist, and A. D. Cianciolo, "The mars science laboratory edl communications brownout and blackout at uhf," *Interplanetary Network Progress Report*, vol. 197, no. 27, pp. 1–22, 2014.

[46] S. Ramjatan, A. Lani, S. Boccelli, B. Van Hove, Ö. Karatekin, T. Magin, and J. Thoemel, "Blackout analysis of mars entry missions," *Journal of Fluid Mechanics*, vol. 904, 2020.

[47] V. F. Giangaspero, A. Lani, S. Poedts, J. Thoemel, and A. Munafò, "Radio communication blackout analysis of exomars re-entry mission using raytracing method," in *AIAA Scitech 2021 Forum*, p. 0154, 2021.

[48] C. Vecchi, M. Sabbadini, R. Maggiora, and A. Siciliano, "Modelling of antenna radiation pattern of a re-entry vehicle in presence of plasma," in *IEEE Antennas and Propagation Society Symposium, 2004.*, vol. 1, pp. 181–184, IEEE, 2004.

[49] A. Scarabosio, J. L. A. Quijano, J. Tobon, M. Righero, G. Giordanengo, D. D'Ambrosio, L. Walpot, and G. Vecchi, "Radiation and scattering of EM waves in large plasmas around objects in hypersonic flight," *IEEE Transactions on Antennas and Propagation*, vol. 70, pp. 4738–4751, jun 2022.

[50] K. Davies, *Ionospheric radio propagation*, vol. 80. US Department of Commerce, National Bureau of Standards, 1965.

[51] F. Wyrowski and C. Hellmann, "Physical optics modeling with smart rays," *Optical Design*, pp. 43–47, 2015.

[52] V. F. Giangaspero, V. Sharma, J. Laur, J. Thoemel, A. Munafò, A. Lani, and S. Poedts, "3d ray tracing solver for communication blackout analysis in atmospheric entry missions," *Computer Physics Communications*, vol. 286, p. 108663, 2023.

[53] Y. A. Kravtsov and Y. I. Orlov, *Geometrical optics of inhomogeneous media*, vol. 38. Springer, 1990.

[54] I. H. Hutchinson, *Principles of Plasma Diagnostics*. Cambridge University Press, 2 ed., 2002.

[55] H. Singh, S. Antony, and R. M. Jha, *Plasma-based Radar Cross Section Reduction*. Springer Singapore, 2016.

[56] Y. Tian, W. Yan, X. Gu, X. Jin, J. Li, and B. Li, "Effects of magnetized plasma on the propagation properties of obliquely incident THz waves," *AIP Advances*, vol. 7, p. 125325, dec 2017.

[57] S. Ellingson, *Magnetostatics Redux*, vol. 2. 2018.

[58] *Antennen und Strahlungsfelder : Elektromagnetische Wellen auf Leitungen, im Freiraum und ihre Abstrahlung*. Wiesbaden: Vieweg+Teubner Verlag, 4., aktualisierte und erweiterte auflage ed., 2012.

[59] W. Demtroder, *Experimentalphysik 2: Elektrizitat und Optik*, vol. 6. 2013.

[60] C. Liang, X. Chen, and P. H. of Electronics Industry, *Electromagnetic Frontier Theory Exploration /*. Berlin ;: De Gruyter„ 2019 - 2020.

[61] S. Ellingson, *Electromagnetics*. VT Publishing, Aug. 2018.

[62] M. Hiebel, *Fundamentals of Vector Network Analysis*. Rohde & Schwarz, 2007.

[63] F. Caspers, "Rf engineering basic concepts: S-parameters," 2012.

[64] V. Giangaspero, "Modeling strategy for blackout analysis of re-entry phases in space exploration missions," Dec 2023.

[65] H. Ling, R.-C. Chou, and S.-W. Lee, "Shooting and bouncing rays: calculating the rcs of an arbitrarily shaped cavity," *IEEE transactions on antennas and propagation*, vol. 37, no. 2, pp. 194–205, 1989.

[66] M. Kundrapu, J. Loverich, K. Beckwith, P. Stoltz, M. Keidar, A. Shashurin, and T. Zhuang, "Modeling and simulation of weakly ionized plasmas using nautilus," 01 2013.

[67] J. Giacomelli, G. Herdrich, V. Sharma, V. F. Giangaspero, N. L. Donaldson, M. K. Kim, A. Munafo, and A. Lani, "Numerical rebuilding of magnetic heat flux control experiments for re-entry vehicles by enhanced mhd simulation tools," *2nd International Conference on Flight Vehicles, Aerothermodynamics and Re-entry Missions Engineering (FAR)*, 2022.

[68] A. J. Knapp, *Experimentelle Untersuchung von Magnetohydrodynamischen Einflüssen auf Plasmaströmungen*. Verlag Dr. Hut, 2012.

[69] J. B. Scoggins, V. Leroy, G. Bellas-Chatzigeorgis, B. Dias, and T. E. Magin, "Mutation++: Multicomponent thermodynamic and transport properties for ionized gases in c++," *SoftwareX*, vol. 12, p. 100575, 2020.

[70] J. G. M. L. A. N. Donaldson, V. Sharma and G. Herdrich, "Deliverable d1.2 (d2): Heat fluxplasma model extension verification," tech. rep., University of Southampton, 2022.

[71] R. Perez, "Chapter 7 - satellite antennas," in *Space Interference* (R. Perez, ed.), vol. 1 of *Wireless Communications Design Handbook*, pp. 222–250, Academic Press, 1998.

[72] "Cst studio suite (2022)." Accessed: 2023-07-01.

[73] "Anechoic chamber upc." Accessed: 2023-07-02.

[74] A. V. Diana Luís, "Radio blackout experiments with magnet," tech. rep., von Karman Institute for Fluid Dynamics, Rhode Saint-Genese, BE, 2024.

[75] B. Bottin, O. Chazot, M. Carbonaro, V. Van Der Haegen, and S. Paris, "The VKI Plasmatron Characteristics and Performance," *Measurement Techniques for High Enthalpy and Plasma Flows*, April 2000.

[76] B. Bottin, *Aerothermodynamic Model of an Inductively-Coupled Plasma Wind Tunnel: Numerical and Experimental Determination of the Facility Performance.* PhD thesis, von Karman Institue for Fluid Dynamics, 1999.

[77] A. Smara, S. Schlachter, and M. Dalban-Canassy, "Design report of the HTS magnet," meesst project technical report d5.2, THEVA DUENNSCHICHT-TECHNIK GMBH, Karlsruhe Institute of Technology, Absolut System, 2022.

[78] S. Schlachter, R. Gehring, and A. Drechsler, "Magnet manufactured," meesst project technical report d5.3, Karlsruhe Institute of Technology, 2023.